INFECTIOUS DISEASE ECOLOGY: IMMUNE-PATHOGEN DYNAMICS, AND HOW TROPHIC INTERACTIONS DRIVE PREY-PREDATOR-DISEASE DYNAMICS

A Dissertation

Presented to the Faculty of the Graduate School

of Cornell University

in Partial Fulfillment of the Requirements for the Degree of

Doctor of Philosophy

by

Paul Joseph Hurtado

January 2012

INFECTIOUS DISEASE ECOLOGY: IMMUNE-PATHOGEN DYNAMICS, AND HOW TROPHIC INTERACTIONS DRIVE PREY-PREDATOR-DISEASE DYNAMICS

Paul Joseph Hurtado, Ph.D.

Cornell University 2012

This thesis comprises theoretical investigations of two biological systems: the first focuses on the consumer-resource and host-parasite dynamics of *Daphnia*, and the second on the immune-pathogen dynamics of *Mycoplasma gallispeticum* (MG) infections in the house finch (*Carpodacus mexicanus*) and other passerine birds. The approach used is to model these biological systems as dynamical systems and to use those models to address specific biological questions.

The first chapter is motivated by recently described relationships between *Daphnia*, their parasites and their algal food source which suggest that these host-parasite and consumer-resource processes directly moderate one another. We currently lack theory to predict how these direct interactions might influence population level dynamics. This work attempts to fill this gap and to address questions specific to the *Daphnia*-parasite system.

In the second chapter I present and analyze a model of the vertebrate immune response to mycoplasma infections. That model is used to identify pathogen and host-immune characteristics responsible for shaping patterns of MG infection in passerine birds, and to identify those that most affect host infectiousness and survival. This work provides a foundation for further theoretical and empirical study of the intimate interactions between mycoplasmas and their hosts.

BIOGRAPHICAL SKETCH

Paul Joseph Hurtado was born on Tuesday June 26, 1979 in Denver, Colorado to Mary F. Hurtado and Michael A. Hurtado. After living in Denver for three years while his father finished dental school, his family packed up their belongings and a stray dog named Liz and moved into his mother's childhood home in his parents' home town of Pueblo, CO. His lifelong friend and only sister Katie was born shortly after the move back to Pueblo.

Paul's formal education began at a Montessori pre-school where he and his sister were able to spend time with their aunt Martha, stuff their little faces full of mulberries, and develop immunity to a variety of mostly harmless infectious diseases acquired from their friends. Later, they each attended local public schools (Pueblo District 60) then the local university (Colorado State University - Pueblo, then known as the University of Southern Colorado).

During his time at Jefferson Elementary School, Paul had to repeat 3rd grade due to his poor performance in math. Fortunately, once his parents and teachers learned that he was easily distracted at school and would tire of doing math problems once he figured out *how* to do them, a few adjustments were made to his daily routine and his studies moved forward without additional setbacks. Paul managed to survive his three years at Pitts Middle School with his math and science interests intact, despite being temporarily afflicted with the social skills that only a teenage boy can possess and occasional conflicts with Mr. Lile, the science teacher. Thankfully, his two wonderful parents and a few parent-teacher conferences helped resolve these disputes.

Paul attended Pueblo's Central High School where many of his high school teachers left their mark on his formative young mind. Peggy Pechek and Judy Wodishek had the daunting task of improving his English and introducing him

to great literature. Sally Keller introduced him to the wonderful world of philosophy, which is still one of his favorite subjects. Jim Benedetto expanded his grasp of general biology and (re)introduced him to the concept of taking organized notes during class. Wayne Doerr taught him both the joys of chemistry, and the joys of having a chemistry lab. Joe Olivieri's passion for music was highly contagious, and his charismatic demeanor made choir one of Paul's more memorable high school activities. Paul graduated from Central High School in June 1998.

Paul attended the University of Southern Colorado after high school, majoring in Biology, Chemistry and Mathematics. He was fortunate to be able to devote the majority of his time to his studies during college, thanks to his parents' continued support (Paul lived in their basement throughout college), scholarships from various organizations, and late night study sessions with his classmates. During college he had the opportunity to spend his summers working on campus as a student researcher with Dr. Sandra Bonetti and Dr. Helen Caprioglio. He spent two summers at Cornell in Carlos Castillo-Chavez's Mathematical and Theoretical Biology Institute (MTBI), which he heard about through his ecology professor and Cornell alum, Dr. Lee Ann Martinez. Paul was an active member of the biology and chemistry clubs, worked in the Math Learning Center, and was very active with the university's Experiential Learning Center, which is an organization that used outdoor recreation to teach science, leadership and professional development. Paul's experiences with these individuals and organizations taught him many invaluable lessons and contributed heavily to his decision to pursue his graduate studies at Cornell's Center for Applied Mathematics with advisor Stephen P. Ellner.

Beyond his formal education, it was outside the classroom where Paul really developed his interests in science and nature. Growing up, his family spent a lot of time outdoors and he began to explore the natural areas near his home as soon as he was allowed to cross the street on his bike. Fishing and hunting trips with his father and other friends and family members made up the bulk of his early excursions to the many riparian areas, prairies and mountains near Pueblo. Later involvement with organizations like the Arkansas Valley Audubon Society and the Colorado Division of Wildlife helped broaden his perspective on science, nature and society, as did his father's career in the public health field and his aunt's and mother's work helping people with developmental disabilities. It was the support, criticism and guidance of individuals and organizations like these that led Paul to pursue a career in science and mathematics.

To my parents Mike and Fran,
my sister Katie, my grandmother Lillie,
my aunts and uncles (Martha, Larry, "Butch",
Mary, Edward, Dorothy, and Ritan),
and my wife Deena.

ACKNOWLEDGEMENTS

I'd like to thank my family, especially my wife and fellow CAM grad Deena Schmidt, for their support and encouragement during my graduate studies at Cornell.

My advisor Steve Ellner has been an exemplary researcher, teacher, critic, and mentor during my time at Cornell, and it was a great pleasure to spend time with him discussing science, mathematics and scholarship. I'm incredibly grateful for his guidance, sage advice, unique insights and commitment to his students.

These chapters would not have been possible without the guidance of my advisor, and my collaborations with Spencer Hall (Indiana University, Bloomington) and the "finch conjunctivitis group" (supported by NSF DEB 0622705). I would especially like to thank Andrè Dhondt, Wes Hochachka, Dana Hawley, Andy Dobson, Erik Osnas, David Ley, Jessica Grodio, and Sarah States. I also thank Michael Cortez, Laura Jones, Joe Simonis, Andrea Graham, Ann Thomas, Jonathan Rubin, Judy Day, Marisa Eisenberg, Suzanne Robertson and Frank Hilker for their questions and comments; the Center for Applied Mathematics (CAM), the SLOAN foundation and the Cornell Graduate School for graduate student support; and the Mathematical Biosciences Institute at The Ohio State University (NSF DMS 0635561, 0931642) for hosting me during the writing of this manuscript.

Many other outstanding faculty and staff contributed to my graduate training at Cornell. Among them are Richard Rand, Steve Strogatz, John Guckenheimer, Evan Cooch, Nelson Hairston Jr., Irby Lovette, Monica Geber, David Winkler, Karl Schat, Caren Cooper, Maria Tarrell, Rick Durrett, Al Schatz, Meena Haribal, Zellman Warhaft, Mark Holton, Dolores Pendell and Selene Cammer. I

owe special thanks to Carlos Castillo-Chavez, as without his Mathematical and Theoretical Biology Summer Institute (MTBI) I most likely would have never even applied to graduate school at Cornell.

My graduate training at Cornell was deeply enriched by time spent with other students and members of the Ithaca community. CAM is a stimulating and rewarding environment to work in because of its bright and diverse group of graduate students. I also benefited greatly from interactions with students and staff in other departments (e.g. EEB, Math and TAM), the Cornell Laboratory of Ornithology, and through Cornell Outdoor Education. This long list includes Matt Holden, Chris Schepper, Lauren Childs, Christian Kuehn, Ben Dalziel, Jon DeCoste, Sarah States, Nancy Chen, Jessica Zuniga, Ryan Hernandez, Sam Arbesman, Jason Martin, Carla Martin, Erik Sherwood, Joe Tien, Rebecca Tien, Emilia Huerta-Sanchez, Fergal Casey, Johnny Guzman, Tara Small, Jesus Rodriguez, Sharad Goel, Suzanne Shontz, Sarah Iams, Joel Nishimura, Diarmuid Cahalane, Tim Novikov, Ben Shaby, David Slater, Aaron Solo, Edoardo Carta-Gerardino, Danielle Lyles, Anael Verdugo, Viviana Ruiz-Gutierrez, Elise Zipkin, Chris Jenelle, Joe Simonis, Chris Wiley, Nicholas Sly, Shawn Billerman, Marcus Collins, and Lauren Peritz, just to name a few.

TABLE OF CONTENTS

LIST OF FIGURES

CHAPTER 1

INFECTIOUS DISEASE IN PREDATOR POPULATIONS: DYNAMIC CONSEQUENCES OF PREY-MEDIATED TRANSMISSION AND INFECTIOUSNESS

1.1 Abstract

Host-parasite and consumer-resource interactions have traditionally been assumed to influence one another *indirectly*, via the abundances or density of different organisms. Recently, studies of *Daphnia* and their parasites have found strong *direct* interactions between host-parasite and consumer-resource processes mediated by individual-level changes in behavior and physiology. Despite the long history of modeling consumer-resource and host-parasite systems, we currently lack theory to predict how these direct dependencies might influence population level dynamics. This work attempts to bridge that gap by describing the dynamics of a general consumer-resource model with infectious disease among the consumer population, and comparing those dynamics with and without these direct dependencies between consumer-resource and host-parasite processes. General mathematical results for direct and indirect transmission models are provided along with results specific to the motivating biological system (*Daphnia*, their parasites and their algal food source). These comparisons suggest that these direct dependencies can significantly affect population level dynamics and should be included in models used for certain applications, and that an informative way of quantifying these dependencies is to use relative sensitivities (elasticities).

1.2 Introduction

Despite the known potential for interspecific interactions to affect disease spread and persistence, such factors are rarely considered in simple models of disease transmission. This is partly because of the fundamental role of interactions within the host population, the utility of simple single-population models, the difficulties of analyzing higher dimensional models, and the practical challenges of collecting the data needed to study the roles of various ecological factors in natural systems [Wood et al., 2007, Lively, 2006, Hall et al., 2009b], especially wildlife and other non-human populations.

Strong interspecific interactions have the potential to alter disease dynamics through a variety of mechanisms [Ostfeld et al., 2008, others]. These include elevated rates of predation on infected hosts [Duffy et al., 2005, Hall et al., 2005, Duffy, 2007, Roy and Holt, 2008], changes in transmission rates in the presence of competitors [Hall et al., 2007, 2009a], and changes in disease progression due to external resource dynamics driving host metabolic demands and internal allocation of resources [Hall et al., 2009b, Hall, Spencer R. and Simonis, JosephL. and Nisbet, RogerM. and Tessier, AlanJ. and Cáceres, CarlaE., 2009]. Consequently, ecological interactions influence important quantities such as host infectiousness (pathogen load), the duration of infectiousness and demographic consequences of infection for individual hosts such as increased mortality (pathogen virulence).

This paper was motivated by recent studies of parasitism in *Daphnia*, particularly the fungal pathogen *Metschnikowia bicuspidata* in *Daphnia dentifera* [Hall et al., 2005, 2006, Duffy, 2007, Hall et al., 2007, Duffy et al., 2008, Duffy and

Hall, 2008, Hall et al., 2009b, Hall, Spencer R. and Simonis, JosephL. and Nisbet, RogerM. and Tessier, AlanJ. and Cáceres, CarlaE., 2009, Ebert, 2005]. *Daphnia* are major algal consumers in freshwater ponds and lakes, and their population dynamics are tightly linked to algal population dynamics [McCauley et al., 1999, Ebert, 2005, Ch. 2]. *Daphnia* populations can also be under "top down" control due to predation by larval insects and fish, which selectively feed on infected *Daphnia* [Duffy et al., 2005, Duffy, 2007]. Importantly, these studies have revealed that the quantity and quality of the host population's algal food source greatly influence two important determinants of disease.

(1) The number of infectious spores produced per infected individual and the time to death (duration of infection) vary markedly with the quantity and quality of the host's food source (see Figure 1.1) [Hall et al., 2009b, Hall, Spencer R. and Simonis, JosephL. and Nisbet, RogerM. and Tessier, AlanJ. and Cáceres, CarlaE., 2009].

(2) Field and laboratory data strongly suggests that foraging effort depends on resource abundance [Hall et al., 2007, Porter et al., 1982]. In our example system and other producer-consumer systems where disease is transmitted via contagion that persist in the environment, a consumer's infection risk is proportional to its foraging effort. As a result, per capita infection risk increases as food becomes less abundant.

In order to study the population level consequences of these ecological and metabolic effects in producer-consumer-disease systems, we consider models motivated by the *Daphnia-Metschnikowia* system. We begin with a standard producer-consumer model that is extended to include spore-based disease transmission among consumers. We then compare the dynamics of this model

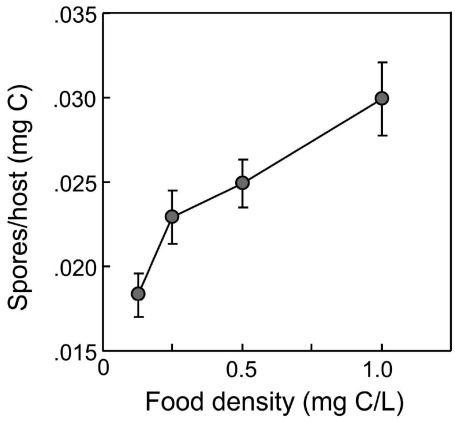

Figure 1.1: Observed dependence of the per capita spore production rate across a range of food densities. Data are from a life-table experiment using *Daphnia dentifera* infected with the fungal pathogen *Metschnikowia bicuspidata*. Figure from Hall, Spencer R. and Simonis, JosephL. and Nisbet, RogerM. and Tessier, AlanJ. and Cáceres, CarlaE. [2009], Fig. 1(F).

with or without (1) a transmission rate that depends on resource abundance, and (2) a spore production rate that depends on resource abundance. We also consider a more general model of producer-consumer-disease dynamics with direct transmission as a limiting case of the spore-based model of disease transmission.

Our results show these resource-dependent epidemiological processes can significantly affect consumer-resource and disease dynamics, particularly non-equilibrium dynamics like consumer-resource cycling and whether disease . Under certain conditions these population-level effects can be predicted using relative sensitivities to quantify how these two rates respond to changes in resource abundance. Computational results show that models that do or do not include these resource-dependencies exhibit similar qualitative dynamics. This may imply that the more tractable "classical" models may be better for qualitative understanding, while including these resource dependencies may be more appropriate for quantitative applications like fitting consumer-resource-disease

models to time series data.

1.3 Model Framework

To investigate how these strong ecological dependencies affect producer-consumer-disease dynamics, we compare those dynamics among particular instances of a general model which either incorporate or ignore these dependencies, respectively. We also consider a direct transmission model as a limiting case of the general model when spore turnover is relatively fast. These models offer limited insights using mathematical analysis alone, therefore both analytical and computational methods are used.

The models are based on a generalized Rosenzweig-MacArthur model of the producer-consumer interaction, modified to include spore-based disease transmission among consumers. The scaled model variables are n the density of producers (amount per unit volume of medium), x the density of susceptible consumers, y the density of infected consumers and z the density of infectious spores. The model variables have been scaled (see Appendix A.1) so that all population units are in producer equivalents (except a factor $\sigma(n)$ for spore density z). Time has been scaled so that one unit of time is equal to the average consumer lifetime in the absence of predation and disease.

1.3.1 General Model

Our model is similar to previous producer-consumer-disease models that have been developed for this and other systems [e.g. Duffy et al., 2005, Hall et al.,

2007, 2006, Duffy and Hall, 2008, Hilker and Schmitz, 2008].

$$\frac{dn}{dt} = rn(1-n) - \alpha(n)(x+y)n \tag{1.1a}$$
$$\frac{dx}{dt} = \alpha(n)(x+fy)n - (1+m)x - \beta(n)xz \tag{1.1b}$$
$$\frac{dy}{dt} = \beta(n)xz - (1+m\theta+\nu)y \tag{1.1c}$$
$$\frac{dz}{dt} = \sigma(n)(1+\nu)y - \mu z. \tag{1.1d}$$

In the absence of consumers ($x + y = 0$), the producer population follows a logistic growth model (see (1.1a)). To model consumption, we use a general per-consumer per-producer feeding rate $\alpha(n)$. This is effectively a measure of feeding effort, which depends on producer density n as detailed below. To incorporate the consequences of disease, the consumer population is partitioned into susceptible (x) and infected (y) individuals which may have different birth rates determined by parameter f. A base mortality rate of 1 results from scaling the units of time into consumer lifetimes. Additional mortality at rate m is due to generalist predation by fish as in Duffy et al. [2005] and Duffy [2007].

Disease transmission to susceptible consumers (1.1b) occurs via contact with infectious material z in the environment (e.g. fungal spores). The rate of contact with infectious spores depends on foraging effort, thus transmission rate $\beta(n)$ depends on producer density n as detailed below. Once infected consumers experience higher death rates due to both direct consequences of disease (rate ν), reduced fecundity ($f < 1$), and a proportional increase in susceptibility to predation ($\theta > 1$).

When an infected individual dies (excluding consumed individuals), it re-

leases $\sigma(n)$ units of infectious spores into the environment (1.1d). In the *Daphnia-Metschnikowia* system, well-fed hosts harbor well-fed parasites which in turn produce more fungal spores (see Figure 1.1). To model this resource-dependence we assume a spore production rate $\sigma(n)$ which depends on producer abundance. Once released, spores then degrade or are lost from the environment (at rate μ).

For numerical studies of the model we use specific forms of $\alpha(n)$, $\beta(n)$ and $\sigma(n)$ based on experimentally observed relationships in the *Daphnia-Metschnikowia* system,

$$\alpha(n) = \frac{a}{k+n} \tag{1.2a}$$

$$\beta(n) = \frac{\beta_c}{k+n} \tag{1.2b}$$

$$\sigma(n) = \sigma_0 \cdot (1 + \phi n) \tag{1.2c}$$

The form of $\sigma(n)$ is based on the data in Figure 1.1. The form of $\beta(n)$ follows Hall et al. [2009b]. In *Daphnia* and other organisms, the per-capita foraging effort $\mathcal{F}(n)$ varies with food availability [Porter et al., 1982, Hall et al., 2007]. This quantity is defined following the definition of *clearance rate* in Grover [1997] as "the amount of habitat (area or volume) per unit time from which an individual predator removes prey". Foraging effort therefore determines an organism's contact rate with its environment, and any prey items or infectious material in that environment. In the case of *Daphnia*, the volume of media filtered per unit time $\mathcal{F}(n)$ is proportional to $\alpha(n)$, therefore we assume the per-spore per-capita infection rate $\beta(n)$ is proportional to $\alpha(n)$. Under a linear functional response, feeding effort is constant. Under a type-II functional response, $\mathcal{F}(n) \propto \frac{1}{k+n}$ thus

Variable	Value	Description
n	–	Producer density (relative to consumer-free steady state)
x	–	Susceptible consumer density (scaled to producer equivalents)
y	–	Infected consumer density (scaled to producer equivalents)
z	–	Infectious spore density (scaled producer equivalents)
t	–	Time (units are disease-free consumer lifetime)
Parameter	Value	Description
r	40	Producer growth rate (day^{-1}) [Sorokin and Krauss, 1958]
α	–	Type-I consumption rate (consumer^{-1} day^{-1})[Hall et al., 2007]
a	–	Maximum of type-II consumption rate $\alpha(n)$
k	–	Half saturation constant for type-II $\alpha(n)$ [Hall et al., 2007]
ρ	1	Relative feeding rate of infected individuals
f	0.75	Relative fecundity of infected individuals
m	0.6	Fish predation rate on susceptible Daphnia [Duffy et al., 2005]
β	–	Infection rate (susceptible^{-1} spore^{-1}) [Duffy et al., 2005]
ν	1	Additional mortality for infecteds unrelated to fish depredation
θ	3	Fish selectivity for infecteds [Duffy et al., 2005, Hall et al., 2006]
σ	–	Spore production rate (infected^{-1})
ϕ	0.5	Slope parameter for n-dependent spore production rate $\sigma(n)$
μ	0.66	Loss rate of infectious spores (L^{-1}) [Hall et al., 2006]
C	0	Spore consumption rate (day^{-1} consumer^{-1})

Table 1.1: Variables and parameters of the scaled model (1.1). See Appendix A.2 for details.

foraging effort and our transmission rate are monotone decreasing functions of n.

1.3.2 Model Parameters

All parameters of model (1.1) have biological interpretations, which were used to determine the parameter ranges and values shown in Tables 1.1 and A.1 (see Appendix A.2 for unscaled model and parameter details). These quantities mostly come from previous empirical studies [Hall et al., 2006, 2007, Duffy et al., 2005, Duffy and Hall, 2008], though very broad parameter ranges were chosen in some cases to more fully explore the range of dynamics and because of the range of variability found in natural systems – particularly regarding algal growth rates and maximum densities.

In the next section we consider the consequences of the producer dependent rates of transmission $\beta(n)$ and spore production $\sigma(n)$ by comparing model dynamics to the case where both rates are constant. This comparison between *variable rates* and *constant rates* models is accomplished by *equilibrium matching*, where for a given constant rates model equilibrium with producer density n_*, the variable rates model is parameterized so that at equilibrium $\beta(n_*) = \beta$ and $\sigma(n_*) = \sigma$. The same can be done for constant versus non-constant consumption rates $\alpha(n)$. This gives

$$\alpha(n) = \alpha \, \frac{k + n_2}{k + n} \tag{1.3a}$$

$$\beta(n) = \beta \, \frac{k + n_2}{k + n} \tag{1.3b}$$

$$\sigma(n) = \sigma \, \frac{1 + \phi n}{1 + \phi n_2} \tag{1.3c}$$

where α, β, and σ are parameters of the constant rates model with a linear consumption rate (constant $\alpha(n)$) and n_2 is the producer density at the endemic disease equilibrium under that model, derived in Appendix A.3.

1.4 Analytical Results

To understand how producer dependent rates of transmission and spore production affect producer-consumer dynamics and disease persistence, we focus first on the transition from steady state coexistence to cycling dynamics. This transition typically occurs via a Hopf bifurcation.

To simplify notation, we refer to different dynamical states as follows. These include the origin (no organisms), the producer-only steady state $EQ_n = (1, 0, 0, 0)$, producer-consumer equilibrium with no disease $EQ_1 = (n_1, x_1, 0, 0)$, disease-free producer-consumer limit cycle LC_1, producer-consumer-disease equilibrium $EQ_2 = (n_2, x_2, y_2, z_2)$, and producer-consumer-disease limit cycle LC_2. If a stable and unstable pair of limit cycles (or equilibria) exists in the positive orthant (all $n, x, y, z > 0$) we indicate the unstable object with subscript u (e.g. LC_u). Computational and limited mathematical results suggest EQ_2 is unique in the specific cases considered here (except for a small region of parameter space; see Appendix A.5), however other forms of the consumption rate $\alpha(n)$, transmission rate $\beta(n)$ and spore production rate $\sigma(n)$ may result in multiple positive equilibria (see Appendix A.3 for further details).

Before presenting our general results, we first summarize the dynamics of the producer-consumer model without disease, giving particular consideration to the cases where the per-consumer feeding rate $\alpha(n)n$ is either a linear or saturating (type-II) function of producer density n. We then present results for a simplified three dimensional model derived from (1.1) by assuming spore dynamics are fast relative to producer-consumer and infection dynamics. In this case of fast spore dynamics, the full model (1.1) can be well approximated by this sim-

pler three dimensional system with direct transmission among consumers. This model is referred to as the *reduced* or *direct transmission* model. We then present similar results for the more general model (1.1).

1.4.1 Disease-free models

The general producer-consumer model without disease is well understood [Murdoch et al., 2003]. Here we summarize the dynamics of this model assuming the linear ($\alpha(n) = \alpha$) and type-II (1.2a) feeding rates considered below. More general results are included in Appendix A.3.

$$\frac{dn}{dt} = rn(1-n) - \alpha(n)nx \tag{1.4a}$$

$$\frac{dx}{dt} = \alpha(n)nx - (1+m)x \tag{1.4b}$$

The disease-free model can exhibit either a stable coexistence steady state $EQ_1 = (n_1, x_1)$ or a stable producer-only steady state $EQ_n = (1, 0)$, with stability depending on the basic reproductive number of the consumers R_{0c} relative to 1, where

$$R_{0c} = \frac{\alpha(1)}{1+m}. \tag{1.5}$$

R_{0c} is the expected lifetime number of new consumers produced per individual under ideal conditions.

Assuming a linear feeding rate ($\alpha(n) = \alpha$), the origin is an unstable saddle and population trajectories starting with $n, x > 0$ will always converge to either the consumer-free steady state (when $R_{0c} < 1$) or the coexistence steady state EQ_1 (when $R_{0c} > 1$). This model does not exhibit any cycling.

Under the type-II consumption rate $\alpha(n) = a/(k+n)$, model (1.4) is the classic Rosenzweig-MacArthur model which exhibits the same qualitative dynamics as the constant-α case, with the added possibility of producer-consumer cycling. These cycles are born via a supercritical Hopf bifurcation, whereby the stable steady state EQ_1 loses stability and gives rise to stable producer-consumer cycles LC_1. This is the well known "paradox of enrichment" [Rosenzweig, 1971] or the "suppression-stability tradeoff" [Murdoch et al., 2003] where an increase in the food quality of producers and/or an increase in consumer effectiveness results in population cycling. Mathematically, cycling occurs when consumer's basic reproductive ratio R_{0c} increases through $R_H = 1/(1-k)$ from $1 < R_{0c} < R_H$ to $1 < R_H < R_{0c}$ as detailed in Appendix A.3.

1.4.2 Reduced Model: Rapid Spore Dynamics

When spore turnover is fast relative to other population rates of change, spore density $z(t)$ rapidly reaches a quasi-steady state (where $\frac{dz}{dt} \approx 0$), thus $z(t)$ tracks $y(t)$ as approximately $z(t) \approx \left(\frac{\sigma(n(t))(1+\nu)}{\mu}\right) y(t)$. Inserting this approximation in (1.1) then defining the direct transmission rate $B(n) = \frac{\beta(n)\sigma(n)(1+\nu)}{\mu}$ we can approximate model (1.1) with

$$\frac{dn}{dt} = rn(1-n) - \alpha(n)(x+y)n \tag{1.6a}$$

$$\frac{dx}{dt} = \alpha(n)(x+fy)n - (1+m)x - B(n)xy \tag{1.6b}$$

$$\frac{dy}{dt} = B(n)xy - (1+m\theta+\nu)y \tag{1.6c}$$

For a similar model with frequency-dependent direct disease transmission see Hilker and Schmitz [2008]. Model (1.6) can exhibit each of the equilibrium

states mentioned above: the producer only steady state EQ_n, the disease-free producer-consumer equilibrium EQ_1 and the endemic disease equilibrium EQ_2. To describe the stability conditions for these equilibria (and the transition to producer-consumer-disease cycles LC_2) we first introduce the following quantities.

The basic reproductive ratio of the disease R_{0d} for both the reduced model (1.6) and the general model (1.1) is given by

$$R_{0d} = \left(\frac{\beta(n_1)x_1}{\mu}\right)\left(\frac{\sigma(n_1)(1+\nu)}{1+\nu+m\theta}\right) \tag{1.7}$$

We interpret R_{0d} as the expected number of new infections per infected individual in a disease-free population at steady state (EQ_1). It is here written as the product of the expected number of new infections per spore and the expected number of new spores per infected individual. Note this criterion (and R_{0c}) depend only on the values of $\alpha(1)$, $\alpha(n_1)$, $\beta(n_1)$, and $\sigma(n_1)$ and not any other values or derivatives of these functions.

As we will show, the stability differences between variable and constant rates models depend on the *relative* strength of n-dependence in $\beta(n)$ and $\sigma(n)$. For this reason, we sometimes write derivatives $\sigma'(n)$ and $\beta'(n)$ in terms of their elasticities. For a given function $F(n)$, the *elasticity of F with respect to n* is defined as $E_F = \frac{dF(n)}{dn}\frac{n}{F(n)}$. This dimensionless quantity is the proportional change in $F(n)$ per proportional change in n. Elasticities evaluated at the endemic disease equilibrium value of $n = n_2$ are indicated with an asterisk (e.g. E_{F*}). Two properties of elasticities used below are 1) if $F(n)$ and n are positive then E_F and $F'(n)$ have the same sign, and 2) if F is proportional to the product of two functions, e.g. $F(n) \propto g(n)h(n)$, then $E_F = E_g + E_h$.

Dynamics and Stability

Our goal here is to compare the stability criteria for the endemic disease steady state EQ_2 under the constant rate model (1.6) with those of the EQ_2-matched variable rates model (1.6). For both models, if $R_{0d} < 1$, the disease dies out. If both $R_{0c}, R_{0d} > 1$, then disease can persist in the consumer population in at least two ways: at equilibrium when EQ_2 is stable, or under stable endemic-disease cycles, LC_2. The transition between these two states (a Hopf bifurcation) can be found via a standard stability analysis using the Routh-Hurwitz stability criteria [Guckenheimer et al., 1997, Guckenheimer and Myers, 1996]. See Appendix A.4 for details.

As shown in Appendix A.4, whether non-constant $B(n)$ has a stabilizing or destabilizing affect on the population dynamics in the presence of disease (i.e. whether it shifts the Hopf bifurcation in a way that impedes or promotes cycling) depends only on whether $B(n)$ is an increasing ($E_{B*} > 0$) or decreasing ($E_{B*} < 0$) function of n, respectively, at the endemic equilibrium ($n = n_2$). In terms of $\beta(n)$ and $\sigma(n)$,

$$E_{B*} = E_{\beta*} + E_{\sigma*} \tag{1.8}$$

implies that for model (1.6) the difference in stability between constant and variable rates models is determined by the sign of the net relative sensitivity of $\sigma(n)$ and $\beta(n)$ at the endemic disease equilibrium EQ_2. In the *Daphnia-Metschnikowia* example assuming fast spore dynamics, the decreasing transmission rate $\beta(n)$ therefore has a destabilizing effect on the system, while the increasing rate of spore production $\sigma(n)$ has a stabilizing effect.

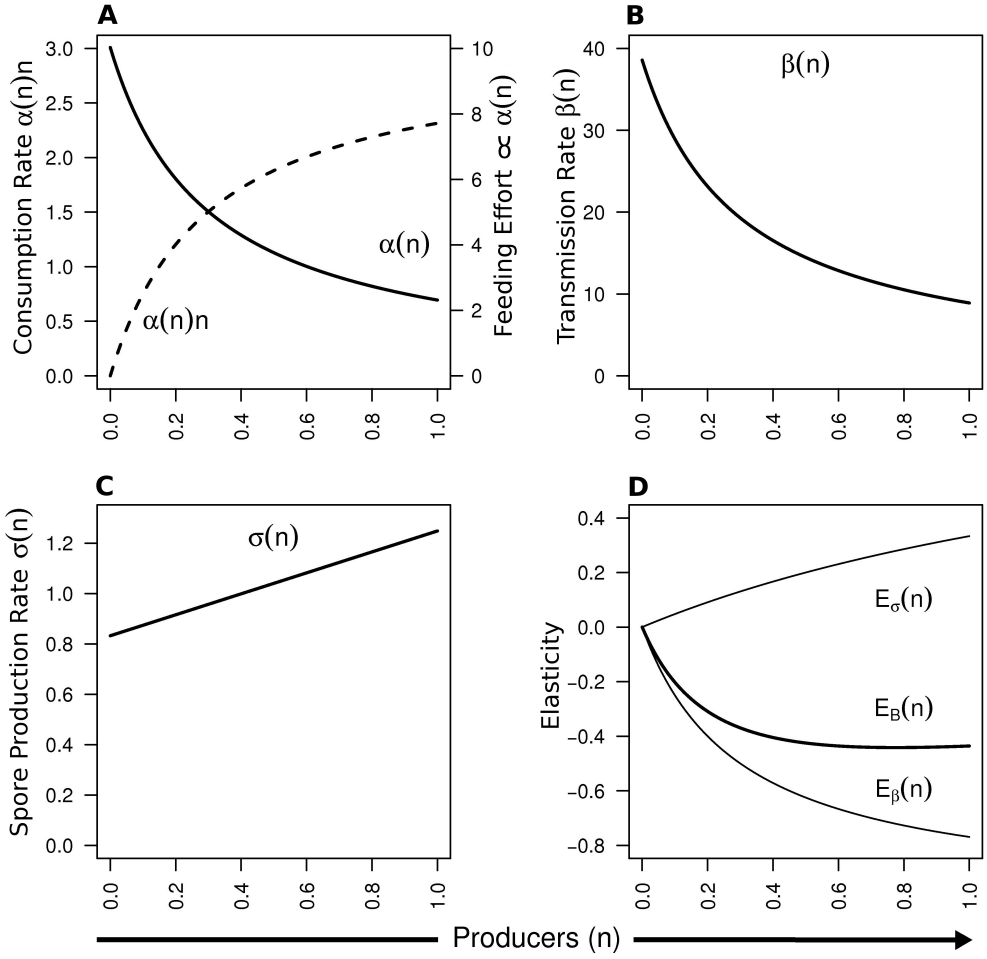

Figure 1.2: Examples of n-dependent rates of consumption $\alpha(n)$ (**A**), transmission $\beta(n)$ (**B**) and infectiousness $\sigma(n)$ (**C**), and their elasticities (**D**). Panel **A**: A type-II predation rate $\alpha(n)n$ implies the rate of environmental exposure (e.g. volume of water filtered per unit time) is proportional to $\alpha(n)$. Panel **B**: This rate of exposure implies transmission rate $\beta(n)$ is proportional to $\alpha(n)$. Panel **C**: The spore production rate $\sigma(n)$ is linear based on Figure 1.1. Panel **D**: In the case of the direct transmission model (1.6) and some cases of model (1.1) with moderate to fast spore dynamics, the stability consequences of these mechanisms can be determined by the sign of $E_B = E_\sigma + E_\beta$ at the endemic disease equilibrium value of the producer density, $n = n_2$. Positive E_B means stabilizing, negative E_B destabilizing. As in model (1.1), producer density (n) is scaled relative to the consumer-free carrying capacity (thus $n_{max} = 1$).

Invasibility of the disease-free state EQ_1

We may also consider how producer dependent rates $\beta(n)$ and $\sigma(n)$ affect disease invasion – i.e. the stability transition between EQ_1 and EQ_2 as determined by R_{0d} (1.7) – using two basic facts. First, matching the constant and variable rates models at EQ_2 requires that $B(n_2) = B$, thus the basic reproductive numbers for disease under the constant (R^c_{0d}) and variable rates models (R^v_{0d}) are proportional to $B = B(n_2)$ and $B(n_1)$, respectively. Second, since disease decreases consumer density by increasing mortality and decreasing fecundity ($x_2 < x_1$) it indirectly increases producer density ($n_2 > n_1$).

Therefore if $B(n)$ is a strictly decreasing function of n, by $n_2 > n_1$ it follows that variable rates increase the basic reproductive ratio ($R^v_{0d} > R^c_{0d}$). Likewise, if $B(n)$ is increasing then $R^v_{0d} < R^c_{0d}$. Thus, under the variable rates model the disease-free steady state EQ_1 is easier to invade when $B(n)$ is decreasing at n_2 (i.e. the endemic disease state EQ_2 is relatively more stable if $B'(n_2) < 0$), and EQ_1 is harder to invade when $B(n)$ is increasing at n_2.

1.4.3 Full Model

Next, we relax the assumption that spore dynamics are relatively fast and consider the full model (1.1). As above, we can describe how the stability conditions for the endemic disease equilibrium EQ_2 under the variable rates model differ from the stability conditions under the constant rates model (see Appendix A.4 for details). It can be shown that an increasing $\sigma(n)$ always has a stabilizing effect (as was the case under the direct transmission model (1.6)) while a decreasing $\beta(n)$ may have either a destabilizing or stabilizing effect.

Comparing the constant and variable rates models (1.1) with general $\alpha(n)$, the difference in stability of the endemic disease steady state EQ_2 near the Hopf bifurcation depends only on the sign of

$$(E_{\beta*} + E_{\sigma*})d_3^2\mu - E_{\beta*}(\gamma E_{\beta*} + (d_2d_3 - 2d_1)) \tag{1.9}$$

where each $d_i > 0$ $(i = 1, 2, 3)$ and $\gamma > 0$ as detailed in Appendix A.4. For very fast spore dynamics (e.g. μ and σ relatively large), this result agrees with the results of the previous section. The first term in (1.9) dominates so that an increasing $\sigma(n)$ has a stabilizing effect on the Hopf bifurcation, and a decreasing $\beta(n)$ has a destabilizing effect. More generally, (1.9) indicates that an increasing $\sigma(n)$ will always stabilize the transition to cycling dynamics (i.e. expand the region of parameter space where EQ_2 is stable by shifting the Hopf bifurcation), while a decreasing $\beta(n)$ can be either destabilizing or stabilizing depending on the sign of the second term in (1.9), which is quadratic in $E_{\beta*}$.

1.5 Bifurcation Analysis

Producer-consumer and other predator-prey systems commonly exhibit non-equilibrium dynamics. These typically include cycling (e.g. classical producer-consumer cycles), oscillations induced by periodic environmental drivers (e.g. seasonal temperature change) and transient oscillations. In the next two sections we describe how producer-dependent rates of transmission and infectiousness affect disease persistence and these non-equilibrium population dynamics under models (1.1) and (1.6). We do this using computational methods (e.g. the bifurcation continuation software Matcont in MATLAB [Dhooge et al., 2003]) to analyze and compare the non-equilibrium dynamics that occur in the constant and

variable rates models (1.1) with a type-II consumer feeding rate ($\alpha(n) = a/(k+n)$). Importantly, models (1.1) and (1.6) can exhibit other non-equilibrium dynamics and instances of bistability as described in Appendices A.5 and A.6.

Numerical investigations of these models with parameter ranges based on the *Daphnia-Metschnikowia* system suggest this system typically exhibits either steady state dynamics or cycling dynamics, either with or without disease (and consumer) persistence. Some parameter regimes also yield bistability between the steady state with disease (EQ_2) and cycling dynamics with or without disease.

To facilitate model comparison and computation, both constant and variable rates models with type II $\alpha(n)$ are matched at EQ_2 to the constant rates model (1.1) with predation rate $\alpha(n) = \alpha$ (see Appendix A.4 for details). This is accomplished using equations 1.3. Comparisons are restricted here to parameter regimes where the population sizes comprising the endemic disease equilibrium EQ_2 are biologically meaningful (i.e. non-negative) as shown in Appendix A.3, Figure A.1.

1.5.1 Constant Rates Model

We begin by describing the dynamics exhibited by model (1.1) with constant rates $\beta(n) = \beta$ and $\sigma(n) = \sigma$. Figure 1.3 summarizes the dynamics associated with different regions of parameter space and the bifurcations that form the boundaries of those regions. Additional dynamics can occur in these regions, but are less biologically relevant and have been omitted here for clarity (see Appendix A.5 for details).

To clarify Figure 1.3, we describe how the dynamics change as parameters are moved through regions ①-⑤. In region ①, the endemic disease equilibrium EQ_2 is stable: disease persists without population oscillations. One can exit that region along two qualitatively different paths. The first option is to cross into region ② then ⑤. The second is to exit through region ③ towards ⑤.

Traveling along the first path into region ②, EQ_2 loses stability via a Hopf bifurcation $\mathbf{H}_-$ and gives rise to *stable* disease limit cycles LC_2 in region ② (see panel ② in Figure 1.4). This is analogous to the disease-free transition from steady state producer-consumer dynamics to producer-consumer cycling, but in the presence of disease. Continuing through ② towards region ⑤, disease prevalence decreases as the amplitude of the disease cycle LC_2 increases. Disease is eventually lost from LC_2 at the boundary between ② and ⑤ leaving the disease-free cycle LC_1 stable in ⑤ (see panel ⑤ in Figure 1.4).

Mathematically, these two transitions are called a supercritical Hopf bifurcation $\mathbf{H}_-$ (part of the Hopf bifurcation discussed in Section 1.4) and a transcritical bifurcation of limit cycles (labeled **BPC** for the *branch point cycle* that occurs at the bifurcation). The qualifier *supercritical* indicates EQ_2 gives rise to stable cycles at $\mathbf{H}_-$. A *subcritical* Hopf would yield an unstable cycle. As parameters approach **BPC** from ②, the disease components y and z approach 0 and disease cycle LC_2 approaches the disease-free cycle LC_1. At **BPC**, $y = z = 0$ and LC_2 collapses onto LC_1 (the orbit $LC_1 = LC_2$ is the *branch point cycle*). Beyond **BPC** in region ⑤, LC_2 continues towards negative y and z values leaving the disease-free limit cycle LC_1 stable.

A second option to exit region ① is through region ③ - a region of bistability between disease cycles LC_2 and the endemic disease equilibrium EQ_2 (see ③ in

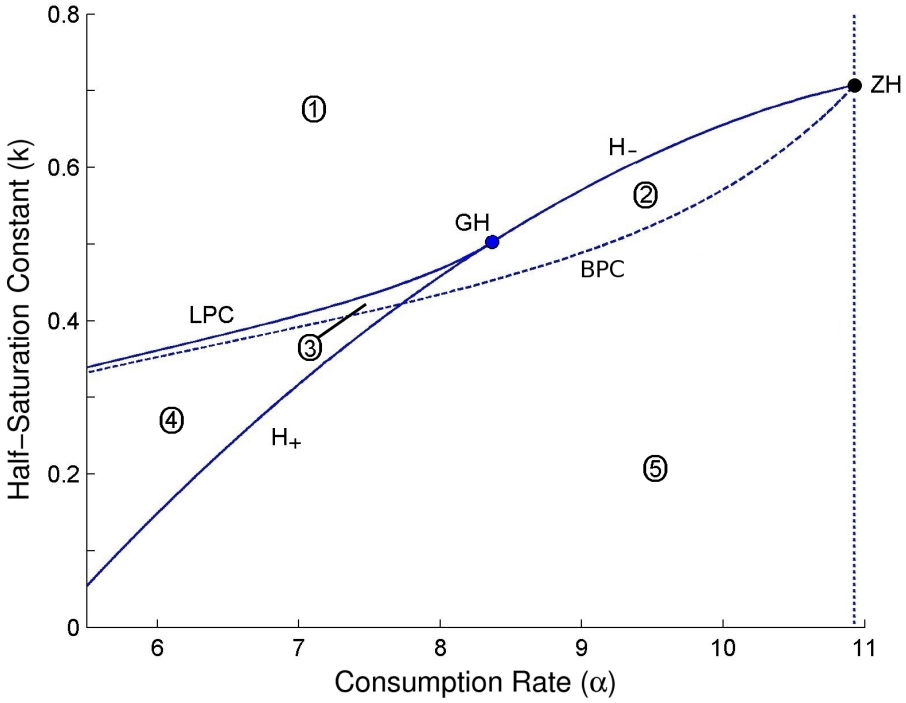

Figure 1.3: Bifurcation diagram summarizing the main population and disease dynamics under the reference case of model (1.1) assuming a type-II feeding rate $\alpha(n) = a/(k+n)$ and constant rates of transmission β and spore production σ. Regions ①-⑤ are separated by bifurcation curves as described in the text. In region ① the endemic disease steady state (EQ_2) is stable. In region ② the equilibrium EQ_2 loses stability and gives way to disease cycles (LC_2). Disease is lost from these cycles in region ⑤ where disease free cycles (LC_1) dominate the dynamics (but see Appendix A.5). There are two regions of bistability between the bifurcation curves labeled **LPC** and $\mathbf{H}_+$, in which EQ_2 is bistable with one of either LC_1 (region ④) or LC_2 (region ③). Appendix A.5 describes additional dynamics not included here, and Appendix A.6 details how host-density dependent disease transmission leads to bistability in these models. To facilitate computation and model comparison, this model is matched to the type-I constant rates model at EQ_2 and parameterized with respect to the per capita feeding rate $\alpha = \alpha(n_2)$ (see the text, Appendix A.3 and Figure A.1 for further details). (Parameters used: $r = 40$, $f = 0.75$, $m = 0.6$, $\theta = 9$, $\nu = 1$, $\mu = 19$, $C = 0$, $\beta = 25$, $\sigma = 0.9$).

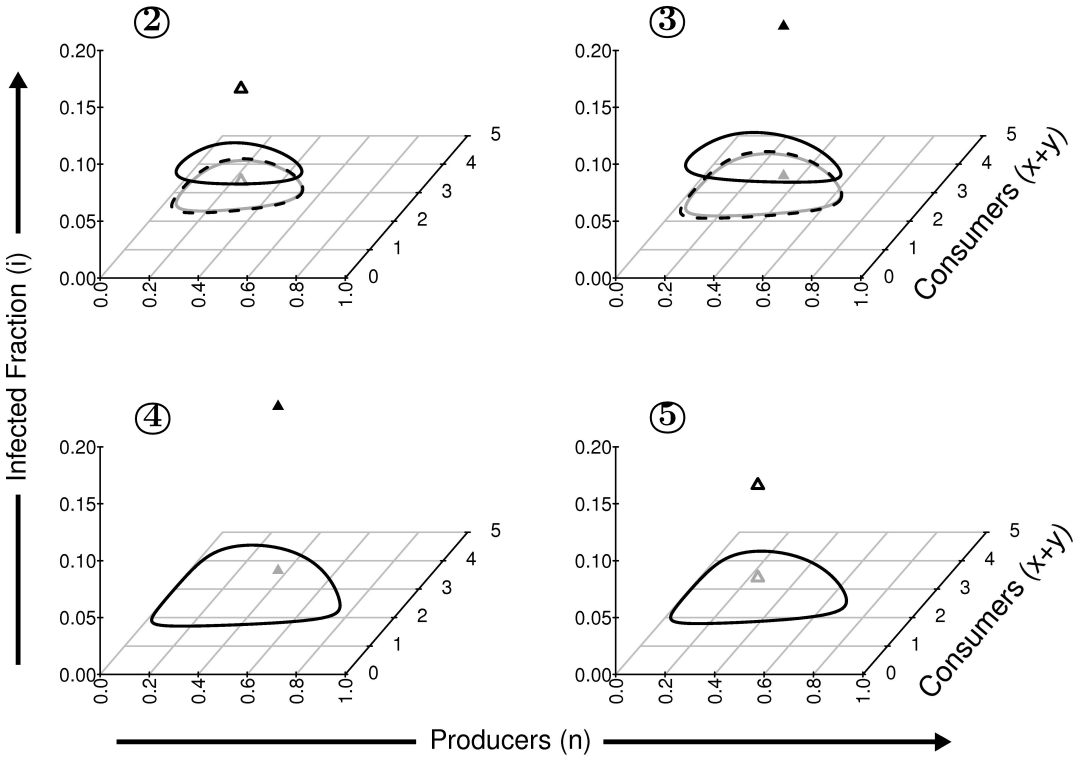

Figure 1.4: Examples of the asymptotic dynamics of model (1.1) corresponding to regions ②-⑤ in Figure 1.3, for producers (n), total consumers ($x + y$), and the proportion of infected consumers ($i = y/(x + y)$) with z not shown. Crossing the Hopf bifurcation curve into region ② (see **H** in Figure 1.3) the endemic equilibrium EQ_2 (black triangle; solid = stable, empty = unstable) has become unstable and the endemic disease limit cycle (solid = stable, dashed = unstable) is attracting. Also shown are the unstable disease-free cycle (dashed) and projections of the two disease states (gray) onto the producer-consumer ($i = 0$) plane. In ③ bistability exists between disease cycle LC_2 and steady state EQ_2. Not shown is the unstable cycle LC_u that forms part of the separatrix between these two attractors. Crossing **BPC** from ③ into ④ (see Section 1.5.1) disease is lost from the attracting limit cycle resulting in bistability between disease-free cycle LC_1 and the endemic disease equilibrium EQ_2. In region ⑤ only disease-free cycles are attracting. (Parameters used: $r = 40$, $f = 0.75$, $m = 0.6$, $\theta = 9$, $\nu = 1$, $\mu = 19$, $C = 0$, $\beta = 25$, $\sigma = 0.9$. In ② $\alpha = 9$, $k = 0.51$; ③ $\alpha = 7.5$, $k = 0.425$; ④ $\alpha = 7$, $k = 0.35$; ⑤ $\alpha = 9$, $k = 0.4$).

Figure 1.4). In region ③ near the bifurcation curve labeled **LPC** (for the *limit point cycle* that occurs at the bifurcation) the basin of attraction for EQ_2 is large while that of LC_2 is small, therefore most trajectories lead to steady state dynamics with disease (EQ_2) while very few result in producer-consumer-disease cycles (LC_2). Moving away from **LPC** the basin of attraction for EQ_2 shrinks while that of LC_2 grows until one of two other bifurcations occurs.

Moving from region ③ to ⑤ can occur two ways: through ② or ④. Crossing $\mathbf{H}_+$ into region ②, the basin of attraction for EQ_2 shrinks to nothing at the subcritical Hopf curve $\mathbf{H}_+$, while that of LC_2 grows until only LC_2 is stable in ② (also see Figure 1.6). Moving from region ③ into ④, disease is lost from LC_2 as was the case crossing **BPC** from region ② into ⑤. Thus, in ④ bistability exists between disease-free cycles LC_1 and disease equilibrium EQ_2 (see ④ in Figure 1.4). Continuing from region ④ into ⑤ is analogous to crossing $\mathbf{H}_+$ from ③ into ②, but where disease is absent from the producer-consumer cycles LC_1. The basin of attraction for LC_1 grows while that of EQ_2 shrinks to nothing at $\mathbf{H}_+$, leaving EQ_2 unstable and LC_1 stable in ⑤.

All of these dynamics can be most clearly understood in the context of generic dynamical behavior near a generalized Hopf bifurcation, with the presence or absence of disease during population cycling determined by the transcritical bifurcation of limit cycles **BPC**. The relevant details of these bifurcations can be summarized as follows.

A generalized Hopf bifurcation consists of three branches (see Figure 1.3): a supercritical Hopf $\mathbf{H}_-$ (to the right of **GH**), a subcritical Hopf $\mathbf{H}_+$ (to the left of **GH**), and a saddle-node bifurcation of limit cycles **LPC** (described below). By definition, a region of bistability exists between **LPC** and $\mathbf{H}_+$, and the nature

of that bistability follows from these two bifurcations. The subcritical Hopf $\mathbf{H}_+$ gives rise to an *unstable* periodic orbit LC_u which exist *above* $\mathbf{H}_+$ in regions ③ and ④ where EQ_2 is locally stable. Ignoring **BPC** for the moment, traversing ③ and ④ from $\mathbf{H}_+$ towards **LPC**, the amplitude of the unstable cycle LC_u increases and the stable and unstable orbits (LC_2 and LC_u) approach one another. The **LPC** is where the two collide (the cycle $LC_u = LC_2$ is called a *limit point cycle*), and beyond the **LPC** both disappear leaving the disease equilibrium EQ_2 as the lone attracting state in region ①. Importantly, this unstable cycle LC_u is part of the separatrix that determines the basins of attraction for bistable states EQ_2 and the stable limit cycle (LC_2 in region ③, and LC_1 in region ④). As a result, the basin of attraction for EQ_2 is vanishingly small near $\mathbf{H}_+$ (i.e. most trajectories result in cycling) and it increases as the amplitude of LC_u increases, i.e. as parameters move from $\mathbf{H}_+$ towards **LPC**. Near **LPC** most trajectories lead to EQ_2 as the basin of attraction for LC_2 is small. Computational results suggest that this family of models can exhibit other bifurcations (e.g. a flip or period doubling bifurcation) however as these are of little biological importance we omit those details from these results.

In summary, the cycling regimes in which disease can persist are regions ② and ③. Disease can also persist at steady state in region ①, an in bistable regions ③ and ④.

1.5.2 General Model

To determine how producer-dependent rates of disease transmission and spore production affect disease persistence under non-equilibrium dynamics, we next

consider model (1.1) with non-constant $\beta(n)$ and $\sigma(n)$ based on observed dependencies in the *Daphnia-Metschnikowia* system. The dynamic consequences of including these two mechanisms manifest as changes in the size or location of regions ② (disease cycles LC_2 stable) and ③ (LC_2 bistable with the disease equilibrium EQ_2). Recall these models are matched to the type I constant rates case (constant α, β and σ) using equations (1.3) and as detailed in Appendix A.4.

To isolate the individual contributions of producer-dependent rates of transmission $\beta(n)$ and spore production $\sigma(n)$ relative to the constant rates model, we consider four versions of model (1.1) assuming neither, one or both of $\beta(n)$ and $\sigma(n)$ are constant. Bifurcation diagrams for these models are shown in Figure 1.5. The qualitative dynamics in each region are equivalent to those described in Figures 1.3, 1.4 and 1.6. Figure 1.5A contains the same bifurcation diagram as in Figure 1.3 (constant rates β and σ). Figure 1.5B assumes non-constant $\beta(n)$ and constant $\sigma(n) = \sigma$, and Figure 1.5C assumes non-constant $\sigma(n)$ and constant β. The bifurcation diagram for the full variable rates model is shown in Figure 1.5D.

We begin with region ① where the endemic disease steady state EQ_2 is stable. The results from Section 1.4 imply that an increasing $\sigma(n)$ should stabilize EQ_2 while under sufficiently fast spore dynamics the decreasing function $\beta(n)$ should destabilize EQ_2 by each shifting **H** towards lower or higher k values thereby changing the size of region ①. Comparing the effect of $\sigma(n)$ alone in Figures 1.5A and 1.5C, the Hopf bifurcation curve **H** is shifted towards lower k values as expected. Comparing Figures 1.5A and 1.5B, $\beta(n)$ has the same qualitative stability consequences as expected from the direct transmission model (1.6) in this case. Recalling equations (1.8) and (1.9), Figure 1.5D shows the combined

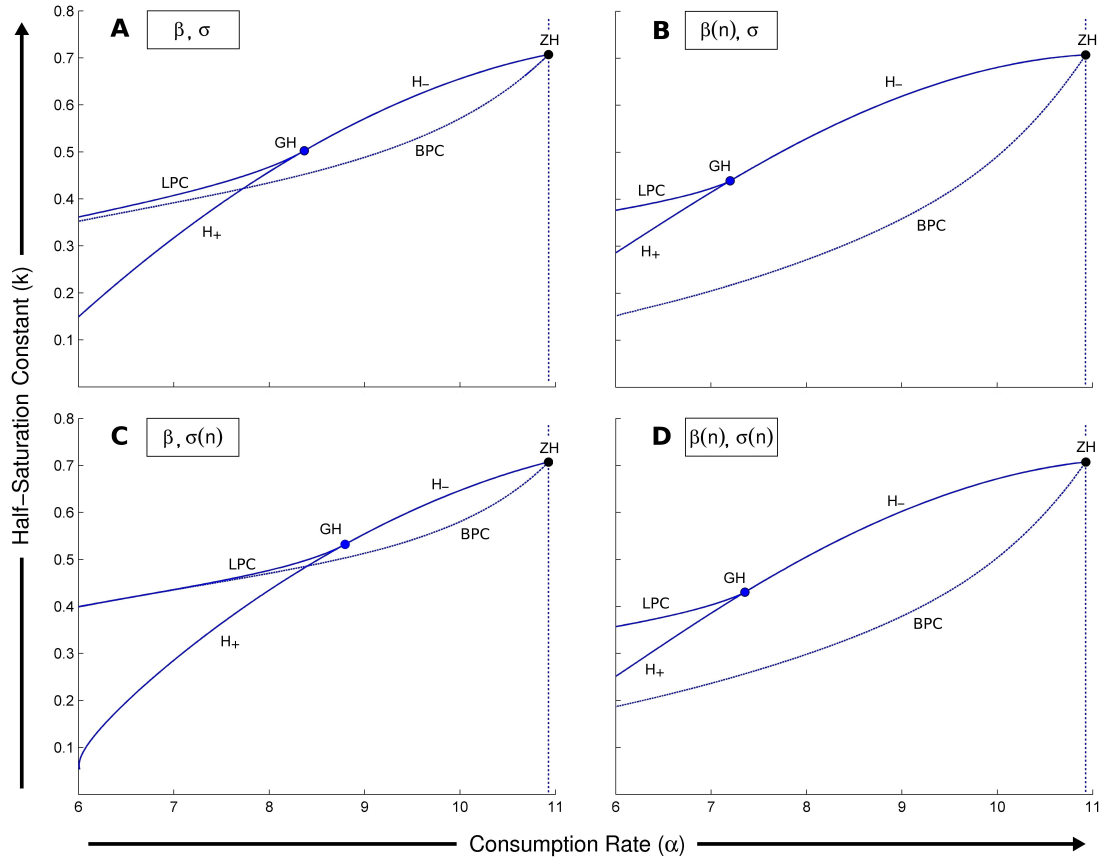

Figure 1.5: Comparison of model (1.1) dynamics with constant and n-dependent rates of transmission ($\beta(n)$) and spore production ($\sigma(n)$). Panel **A** shows the same constant-rates model diagram as in figure 1.3. The diagram for the variable rates model as described in Section 1.5.2 is shown in panel **D**. Panels **B** and **C** show the diagrams for model (1.1) with only one of $\beta(n)$ and $\sigma(n)$ non-constant to illustrate how resource dependent rates of spore production $\sigma(n)$ and transmission $\beta(n)$ each contribute to the dynamical differences between models. See Appendix A.5 for additional dynamics not shown in these diagrams.

effect under the variable rates model in this case is dominated by the effect of $\beta(n)$. The individual and combined elasticities in this case are shown in Figure 1.2, and an illustration of the dynamics in each region ②-⑤ is shown in Figures 1.5 and 1.6.

The change in size of the regions where disease persists during population cycling (② and ③) are determined by the previously mentioned Hopf, the tran-

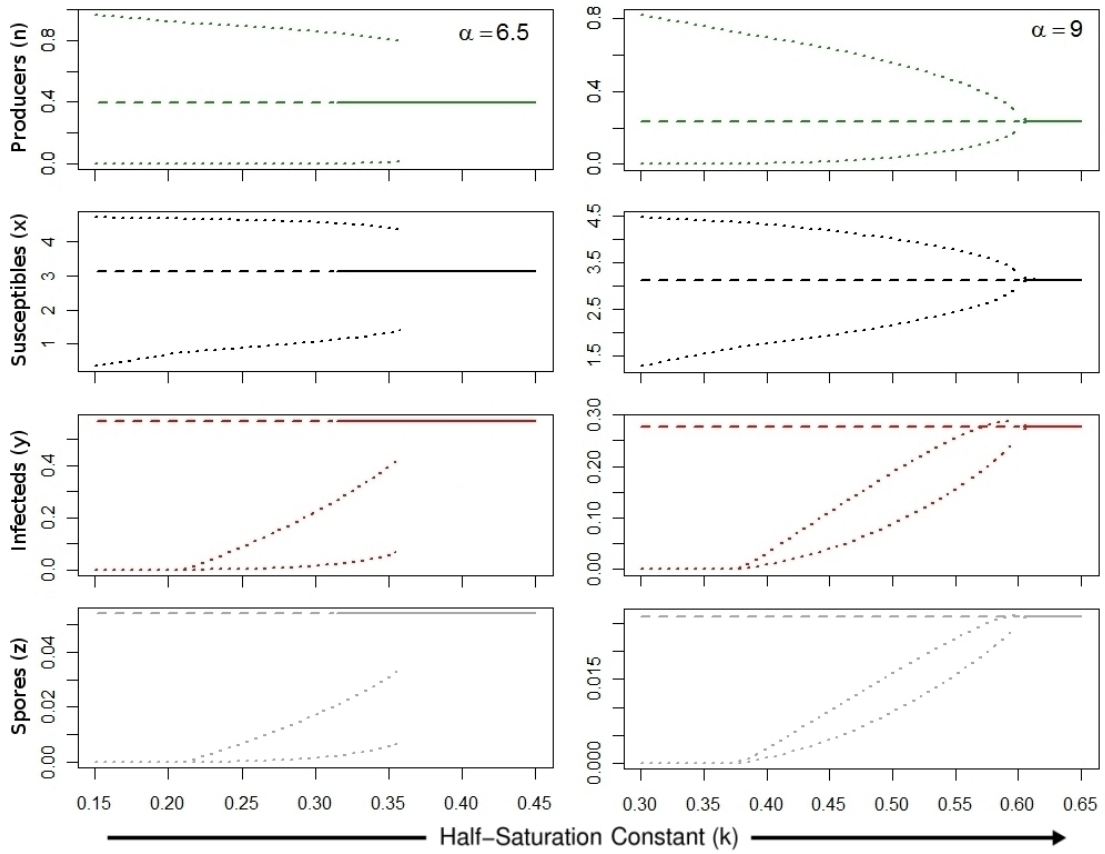

Figure 1.6: Examples of how the model dynamics change as parameters are varied along two different paths through the bifurcation diagram in Figure 1.5D. Solid lines indicate (locally) stable EQ_2 values, dashed lines indicate EQ_2 is unstable, and dotted lines indicate the minimum and maximum values of stable limit cycles with disease (LC_2) or without (LC_1). In the case on the left k increases from 0.15 to 0.45 along $\alpha = 6.5$, crossing through regions ⑤, ②, ③ then ①. Note the bistability between LC_2 and EQ_2 for k between $0.31, 0.36$, which corresponds to region ③. The unstable limit cycle LC_u that exists in regions ③ and ④ as discussed in the text (Section 1.5.1) is not shown. On the right, k increases from 0.3 to 0.65 along $\alpha = 9$ through regions ⑤, ②, then ①. (Note: EQ_2 is constant with respect to k here since this model is matched to the type-I (constant α) constant rates model.)

scritical bifurcation of limit cycles **BPC** and the saddle-node bifurcation of limit cycles **LPC** emanating from the generalized Hopf bifurcation **GH**. Comparing the effect of non-constant $\beta(n)$ and $\sigma(n)$ on **BPC** relative to the constant rates model (Figure 1.5A), we see that the producer-dependent transmission rate $\beta(n)$ greatly increases the regions with disease cycling by shifting **BPC** downwards. The producer-dependent spore production rate $\sigma(n)$ (Fig. 1.5C) has the opposite effect. Under the variable rates model (Fig. 1.5D), changes to **BPC** induced by the producer-dependent transmission rate appear to dominate.

For these parameters, incorporating non-constant $\sigma(n)$ shifts **GH** (and the **LPC**) farther up the Hopf curve, increasing bistability (③ and ④). Incorporating non-constant $\beta(n)$ shifts **GH** downwards, decreasing bistability. Here again the effect of $\beta(n)$ dominates, however with regards to regions ② and ③ these dynamical changes are dwarfed by the larger changes in **BPC** and **H**. The variable rates model therefore shows an overall increase in the size of parameter regimes ② and ③, where disease persists during population cycling.

1.6 Seasonal Forcing

In temperate ponds and lakes, the dynamics of naturally occurring *Daphnia* populations and their algal food source have strong seasonal influences [Scheffer et al., 1997, Ebert, 2005, Ch 2.]. A typical annual cycle begins with large algal blooms in spring as warming temperatures cause vertical mixing of the water column, producing an upwelling of nutrients. *Daphnia* populations increase in response to this abundance of food, eventually driving down algal density. This results in an overabundance of consumers, and their subsequent decline

in numbers. Following this spring algal bloom and clearance by *Daphnia*, the population dynamics that have been observed include continued producer-consumer cycling as well as other dynamics driven by various environmental factors (e.g., succession of the algal community).

Here we briefly illustrate how producer-dependent rates of infection and spore production can affect the dynamics in a seasonally forced version of model (1.1). Seasonal forcing is modeled by dividing the year into two seasons. During the warm season (duration $T = \frac{2}{3}$ years), model (1.1) governs the population and disease dynamics. During the cold season *Daphnia* reproduction and the consumption of algae are halted until the start of the next warm season, which is initiated as follows.

To mimic the spring algal bloom at the start of the warm season, algae (n) are assumed to be at their maximum density ($n = 1$). Typically, initial *Daphnia* levels are relatively low and primarily come from hatching ephippial eggs produced during previous years [Ebert, 2005, Cáceres, 1998]. To model this, we assume all *Daphnia* are initially uninfected and that their initial density x_s is proportional to an exponentially weighted sum of the previous season's reproductive population sizes ($x + fy$). Similarly, the initial spore concentration z_s is assumed to be proportional to the accumulated level of (viable) spores from the previous year. Assuming the previous warm season began at time t_0, the initial quantities for

the following warm season are given by equations (1.10).

$$n_s = 1 \tag{1.10a}$$

$$x_s = \rho_x \int_{t_0}^{t_0+T} [x(t) + fy(t)] e^{-\omega_x (T-t)} dt \tag{1.10b}$$

$$y_s = 0 \tag{1.10c}$$

$$z_s = \rho_z \int_{t_0}^{t_0+T} z(t) e^{-\omega_z (T-t)} dt \tag{1.10d}$$

To compare between constant and variable rates models under seasonal forcing, we first numerically determine the long-term dynamics under the variable rates model for a given parameterization (Figure 1.7A). The constant rates model parameters β and σ are then taken to be the average of their producer-dependent counterparts $\beta(n)$ and $\sigma(n)$ over those asymptotic dynamics during the warm season. Starting from the asymptotic state of the variable rates model, the long-term dynamics of the constant rates model can then be determined.

As shown in Figure 1.7B, there can be significant quantitative differences between constant and variable rates models under seasonal forcing, including temporal inconsistencies in the pattern and intensity of disease. Despite these quantitative differences, the long-term dynamics of the seasonally forced constant rates model do appear to qualitatively match the variable rates model dynamics for the majority of the parameter values considered (not shown). Computational comparisons suggest resource dependent rates of transmission and infectiousness have the biggest impact on the dynamics during the spring algal bloom where producer densities are highest and most variable.

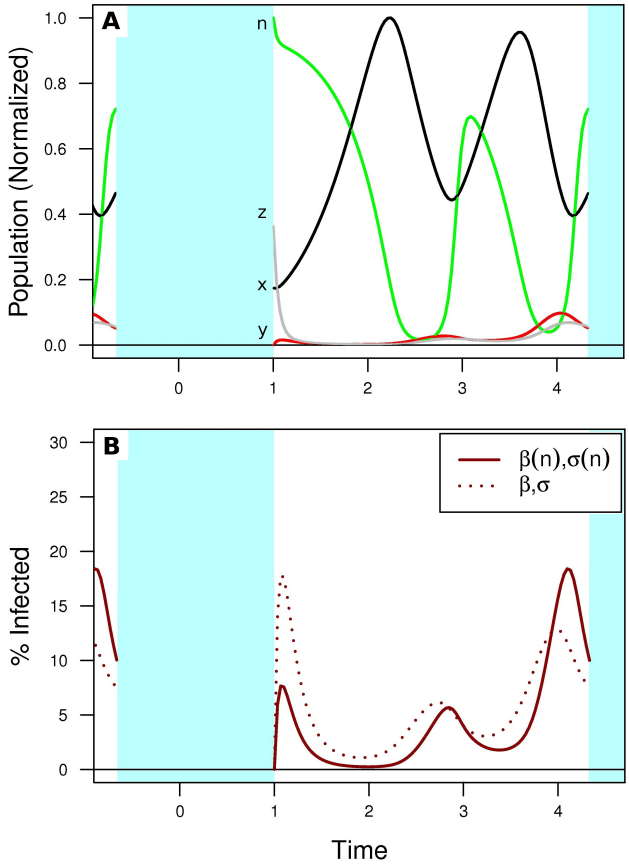

Figure 1.7: A comparison of constant and variable rates models (1.1) with seasonal forcing. Panel **A** shows the asymptotic dynamics of the seasonally forced model with the winter season shaded blue. Recall n = producer density, x = susceptible consumers, y = infected consumers and z = infectious spores. Panel **B** shows the percent of infected consumers under the variable rates (solid line) and constant rates (dotted line) models. The n-dependent rates of transmission and infectiousness have the largest impact on these disease dynamics during the spring algal bloom where resource levels are highest. (Model Parameters: $\alpha = 6$, $k = 0.4$, $r = 40$, $f = 0.75$, $m = 0.6$, $\theta = 9$, $\nu = 1$, $\mu = 19$, $C = 0$, $\beta = 25$, $\sigma = 0.9$ and $\phi = 0.5$. For the constant rates model, $\beta = 26.75$ and $\sigma = 0.92$ which are the average values of $\beta(n)$ and $\sigma(n)$ during the warm season shown in **A**. Time units shown are consumer lifetimes.)

1.7 Discussion

A great deal of progress has been made in recent decades developing theory to explain the population level consequences of trophic interactions. Similar progress has been made developing a theoretical foundation for infectious disease dynamics. A growing body of evidence suggests that trophic interactions and disease processes commonly interact in nature, yet theory that combines the two is relatively scarce. The results presented here are a step towards bridging this gap and help to clarify how these two forces interact to shape the dynamics of natural populations.

Our results suggest that resource dependent rates of disease transmission and infectiousness can significantly alter the transition from the endemic disease steady state to population cycling. If disease is transmitted directly (model (1.6)), the resource dependent rates of transmission and infectiousness will each have a stabilizing effect on the population dynamics if they increase with n near the endemic disease steady state, and will have a destabilizing effect if they are decreasing. The same holds when disease is transmitted via a persistent environmental reservoir (model (1.1)), with one exception: in some cases $\beta(n)$ may have the opposite effect (see equation 1.9). Importantly, when transmission and infectiousness have competing effects (i.e. one increases with n and the other decreases) their combined effect can be quantified using their elasticities at the endemic disease steady state.

In our motivating example of fungal parasitism in *Daphnia*, $\sigma(n)$ is increasing and $\beta(n)$ is decreasing. This yields a net destabilizing effect on the endemic disease steady state, as the destabilizing effect of $\beta(n)$ outweighs the small sta-

bilizing effect of $\sigma(n)$.

Our results also show these mechanisms affect non-equilibrium dynamics, like transient dynamics and whether or not disease can persist under cycling. Under seasonal forcing, the constant and variable rates models can show very different dynamics, suggesting that these mechanisms likely shape the dynamics of natural systems and should be considered for inclusion in models used for making quantitative comparisons with transient or other non-equilibrium data.

Resource dependent rates of transmission and infectiousness can also affect seasonal dynamics. Furthermore, these results affirm that simple models lacking these mechanisms ($\beta(n)$, $\sigma(n)$ constant) can capture important qualitative dynamics of these more detailed models, with some limitations.

Our findings suggest the following directions for future empirical and mathematical research. Particularly revealing tests of our predictions would come from comparing systems where $\beta(n)$ or $\sigma(n)$ differ in whether they are increasing, decreasing or effectively constant. To guide future modeling efforts, a broader body of empirical evidence is needed that quantifies how particular disease processes interact with particular trophic processes in other systems.

Evolutionary dynamics are also ignored in this work. Many theoretical results regarding the evolution of virulence and host-parasite coevolution involve the basic reproductive number of the pathogen $R_{0,dis}$ or related quantities which depend on the value of β and σ evaluated at the disease-free equilibrium (e.g. see Day [2001]). As we learn more about the ecological consequences of resource-dependent disease transmission and progression, we may then ask how they shape the evolution of resource-consumer-parasite systems.

Previous work by Hilker and Schmitz [2008] investigates a similiar model to the direct transmission model (1.6) but with a frequency dependent (instead of density dependent) rate of disease transmission that results in a loss of the bistability exhibited by models (1.1) and (1.6). As detailed in appendix A.6, density-dependent transmission yields bistability in this system because increased disease-induced mortality during consumer-resource cycling causes a counter intuitive *increase* in the average consumer density. This "hydra effect" [Abrams, 2009] in the underlying consumer-resource model, combined with density dependent rates of disease transmission, leads to positive feedback during invasion of disease-free consumer-resource cycles which permits bistability between disease-free cycles and states of disease persistence.

Finally, the family of models we have considered can exhibit other kinds of dynamics than those detailed above. Further bifurcation analyses of these models may reveal other biologically relevant dynamics and conditions under which we expect to observe them, or may yield additional dynamical differences that arise between models that do or do not include direct resource dependencies among important epidemiological rates.

CHAPTER 2

WITHIN-HOST DYNAMICS OF MYCOPLASMA INFECTIONS: CONJUNCTIVITIS IN WILD PASSERINE BIRDS

2.1 Abstract

The host-pathogen interaction drives infectious disease dynamics at the individual, population and community levels. Here I present and analyze a model of the (vertebrate) immune response to mycoplasma infections, and use it to identify which pathogen and host-immune characteristics drive patterns of *Mycoplasma gallisepticum* (MG) infections in the house finch (*Carpodacus mexicanus*) and other passerine birds. We also consider which host and pathogen characteristics most affect host infectiousness and survival. These results imply that much of the observed variation in the house finch likely arises from variation among birds in the effectiveness of their non-specific immune response to MG, and that the host and pathogen characteristics most likely to influence host infectiousness and survival are the intrinsic pathogen growth rate, the strength and efficiency of the non-specific immune response and (to a lesser degree) the rate of activating the specific response. These findings suggest that molecular-level study of how mycoplasmas interact with the host's non-specific and inflammatory responses should reveal much about the relationships between host infectiousness, pathogen load, and symptoms in this and other mycoplasma diseases.

2.2 Introduction

The host-pathogen interaction is at the core of every infectious disease system, and provides an important foundation from which to study infectious disease at the individual, population and community levels. Central to this interaction is the interplay between the pathogen and the host's immune defenses, which can largely determine 1) both short and long term consequences of infection for the host and 2) host infectiousness and pathogen transmission. The immune-pathogen interaction also mediates how various external factors act to shape the progression and consequences of an infectious disease.

The motivation for this paper is a bacterial disease caused by the pathogen *Mycoplasma gallisepticum* (MG), which has been the focus of much study since its appearance in wild passerine birds in eastern North America around 1993 [Dhondt et al., 2005]. Originally known as a respiratory pathogen of domestic poultry, MG has been well studied prior to its jump to passerine hosts in the early 1990s. Its primary host is the house finch (*Carpodacus mexicanus*), a widespread species introduced into eastern North America from southern California in the early 1940s [Elliott and Aribib Jr., 1953, Aldrich and Weske, 1978]. MG can also infect the american goldfinch (*Carduelis tristis*) and other Carduline finches, and has been detected in various other bird species [Fischer et al., 1997, Mikaelian et al., 2001, Hartup et al., 2001, DeCoste et al, pers. comm.]. Disease symptoms include severe inflammation of the conjunctiva (the mucosal surface of the eye), lethargy, and in some cases death [Luttrell et al., 1998, Dhondt et al., 2005].

There are multiple reasons to study *M. gallisepticum* in wild birds. First, this

disease shares many of the hallmarks of mycoplasmal infections in other organisms including some model organisms (rodents), domestic poultry and humans [Blanchard and Browning, 2005]. Second, this wildlife disease is relatively easy to study *in situ* since disease symptoms can be visually observed in wild birds and also since these organisms can be studied in captivity. Third, this system provides an opportunity to study host-pathogen coevolution during the emergence of a novel infectious disease. Following its appearance during the early 1990s MG led to significant declines in the eastern population of the house finch and today continues to spread into western North America. The genomes of some MG strains have been sequenced and the functional genomics of MG and other mycoplasmas are fairly well understood [Papazisi et al., 2003, Blanchard and Browning, 2005]. Furthermore, recent evidence shows that strains of MG circulating among house finches differ in virulence and virulence has changed over time (Hawley, Osnas & Dhondt; pers. comm.).

Figure 2.1 illustrates the range of disease progression among house finches using data from experimentally infected captive birds [Grodio et al., 2008, 2011, Hawley et al., 2010]. The typical course of infection in the house finch ranges from a very mild acute illness to a more persistent chronic disease with prolonged severe inflammation. Symptomatic infections begin with a brief asymptomatic period followed by mild to severe inflammation of the mucosal tissues surrounding the eye and inside the eyelids (the conjunctiva). This diseased state may clear within a week or two, however in some individuals it can persist for months or may be so severe as to result in death. Observations thus far suggest that the resolution of symptoms typically (though not exclusively) follows a reduction in pathogen load by the host's immune response.

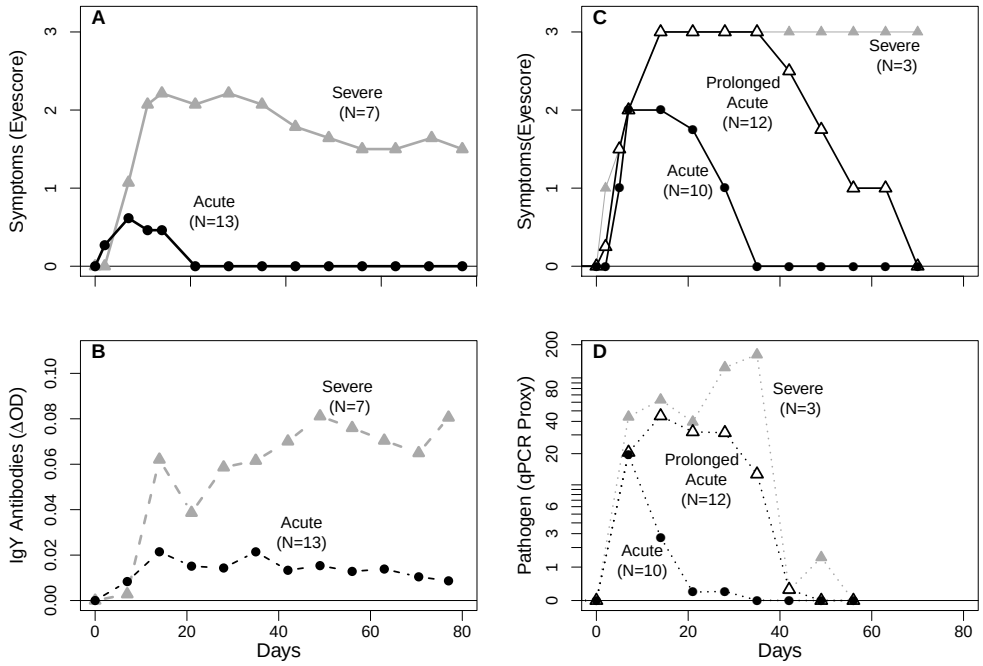

Figure 2.1: *Mycoplasma gallisepticum* infections in the house finch (*Carpodacus mexicanus*) range from very mild to very severe. Panels on the left show symptoms (**A**) and antibody levels (**B**) for 20 individuals from the common garden experiment described in Hawley et al. [2010] and Grodio et al. [2011] (in prep.). The means for groups are shown: the 7 most severe infections from that experiment (N=40) and 13 that resolved symptoms of infection from the group (N=20) infected with a 2006 isolate of *M. gallisepticum*. Panels on the right show average symptoms (**C**) and approximate pathogen load (**D**) from a second experiment [Grodio et al., 2008, 2011]. Here the median values for three qualitatively similar groups are shown: mild acute infections, prolonged acute infections, and severe infections characterized by persistent, severe symptoms over the duration of the experiment. "Eye Score" is a standard measure of the severity of conjunctivitis [Kollias et al., 2004, Sydenstricker et al., 2006] and IgY is the avian equivalent of mammalian IgG.

The goal of this paper is to develop and analyze a dynamic model of the vertebrate immune response to a localized mycoplasma infection and use it to answer the following questions about *M. gallisepticum* in wild passerine birds. First, empirical study of this system has shown significant variation in the progression of *M. gallisepticum* infections within and between host species. Such variation is common in wildlife disease systems with multiple host species. We

ask, to what extent can this variation be explained by a relatively simple model of the pathogen and host immune interaction? What aspects of this variation may result from factors not included this model? Second, preliminary data suggest there has been some evolutionary change in virulence (i.e. the severity of host symptoms) among circulating strains of *M. gallisepticum* (Hawley, Osnas and Dhondt, pers. comm.). Virulence evolution in this system is likely shaped by pathogen load, which drives host infectiousness (pathogen fitness), and by host disease symptoms, which drive host mortality risk and survival (host fitness). We ask, which pathogen and host-immune characteristics most affect host infectiousness and host mortality risk? Can we identify likely targets for empirically detecting virulence-driven selection in the host or pathogen using this model?

Mycoplasma infections are typically quite persistent and induce severe inflammation by eliciting a frustrated and ineffective host immune response. To quote Simecka [2005], "it is likely that almost every component of the host immune system is involved in the response to mycoplasma disease." That is, both specific and non-specific immune responses are involved in controlling infections and mycoplasmas may manipulate the host immune response by interfering with regulatory pathways [Citti et al., 2005]. Because of this complexity – some of which is not well understood – modeling the immune response to mycoplasmas poses a considerable challenge. The approach used here attempts to reduce that complexity by making functional categorizations of the various immune components and their main effects. The key benefit of this approach is that it yields a relatively simple, mathematically tractable model which captures the main biological processes that shape these immune-pathogen dynamics.

The remainder of the paper is organized as follows. Section 2.3 summarizes the key aspects of the host immune response to mycoplasmas, and a brief history of mycoplasmal conjunctivitis in wild birds. Section 2.4 introduces the mathematical model of the host immune response as well as the suite of simplified models which are analyzed in the Results section 2.5. The remainder of section 2.5 addresses how parameter value changes affect different measures of pathogen and host fitness. We end with a summary and discussion of our results in section 2.6.

2.3 Biological Background

It is know from observations of captive and wild individuals infected with *M. gallisepticum* that considerable variation in disease progression exists between and within host species, and between different pathogen strains. In other species known to have only rarely contracted *M. gallisepticum*, for example house sparrows (*Passer domesticus*), individuals can show little to no signs of infection when inoculated with *M. gallisepticum* in captivity [Dhondt et al., 2008]. Many factors likely contribute to this variation by affecting the immune-pathogen interaction. These include pathogen strain, host genetics, nutrition, ambient temperature, time of year, host social status, and the route of initial infection – e.g. orally vs. directly into the conjunctiva [Dhondt et al., 2007, Hawley et al., 2007, 2010, Dhondt et al pers. comm.].

2.3.1 Mycoplasmas and the Host Immune Response

Mycoplasmas belong to the class of bacteria known as the Mollicutes [Edward and Kanarek, 1960, Edward and Freundt, 1967, Brown et al., 2007]. Mollicutes have no cell wall, are among the smallest known bacteria (as small as 0.3μm), tend to be highly host species specific, and unlike many other bacteria cannot produce lipopolysaccharide (LPS) - a cell wall component that elicits a strong immune response in vertebrates. As a group, mycoplasmas interact closely with host mucosal membranes and infections tend to be both persistent and accompanied by severe inflammation.

Based on what is known about the vertebrate immune response to mycoplasmas [Blanchard and Browning, 2005], the typical *M. gallisepticum* (MG) infection in house finches likely proceeds as follows. Once a small population of MG cells is introduced into the conjunctiva, individual cells must survive the first line of host immune defenses (e.g. resting macrophages (MACs), antimicrobial peptides, etc.) and attach to the mucosal membrane. During colonization of the host, close interaction with the host epithelial cells activates the non-specific immune components (e.g. MACs) and induces the host's inflammatory response. The number and activity level of phagocytic cells at the infection site increases, however these may be ineffective at killing MG without the presence of specific antibodies [Hickman-Davis et al., 1997, Simecka, 2005, pp.485-493]. This ineffective non-specific immune response slows, but does not stop, the growing pathogen population. Antigen presenting cells associated with the non-specific immune response then activate specific immune components by transporting MG antigens into the lymphatic system. There they initiate B- and T-cell selection and maturation which later results in the production of MG-specific anti-

bodies. Once at the infection site, these antibodies bind to MG allowing phagocytic cells like MACs to more effectively neutralize MG. This results in clearance of the infection unless MG evades the immune response [e.g. via surface antigen turnover, Citti et al., 2005] or the response is otherwise ineffective. As is commonly the case with mycoplasma infections, pathogen persistence is associated with sustained inflammation from the host's frustrated and ineffective immune response. In house finches, this includes visible signs of conjunctival inflammation accompanied by epithelial and lymphoid hyperplasia [Luttrell et al., 1996, Dhondt et al., 2005, others].

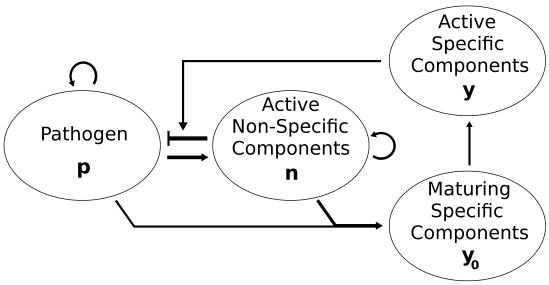

Figure 2.2: Model variables and main interactions included in the immune response model (2.1).

2.4 Model

This model is based on the innate (non-specific) immune response model described in Reynolds et al. [2006], which we extend to include the adaptive (specific) immune response to mycoplasmas as described in Simecka [2005]. The state variables represent the combined activity of various immune system components involved in the response to mycoplasma infections, grouped into functional categories as illustrated in Figure 2.2. Scaled to reduce the number of parameters, the state variables are the pathogen density p, active non-specific (innate) immune components n, and progenitor cells y_0 that mature into active specific immune components y (e.g. maturing and anti-body producing B-cells, respectively). The model equations are

$$\frac{dp}{dt} = k_{pg} p\,(1-p) - \frac{k_m p}{\mu_p + p} - K(y) n p \tag{2.1a}$$

$$\frac{dn}{dt} = \frac{n + k_p p}{x_n + n + k_p p} - \mu_n n \tag{2.1b}$$

$$\frac{dy_0}{dt} = \frac{(np)^\alpha}{x_y^\alpha + (np)^\alpha} - \mu_{y0} y_0 \tag{2.1c}$$

$$\frac{dy}{dt} = \mu_{y0} y_0 - \mu_y y \tag{2.1d}$$

where $K(y)$ is an increasing function of y with $K(0) > 0$. The unscaled model equations and their relationship to the model by Reynolds et al. [2006] are given in Appendix B.1.

The pathogen population is assumed to follow equation (2.1a), which exhibits logistic growth with intrinsic growth rate k_{pg} in the absence of a host immune response (pathogen units have been scaled to maximum density $p = 1$ as detailed in Appendix B.1). The second term in (2.1a) models the ability of local (unactivated) immune defenses to neutralize an initially small population of invading pathogen as detailed in Reynolds et al. [2006].

The activated non-specific immune components n (see eqs. 2.1a,b) include phagocytic and antigen presenting cells like macrophages as well as other cells like heterophils (avian neutrophils). Activation of innate immune components results from both the presence of pathogens and some positive feedback, with deactivation occurring at rate μ_n. Together, they are assumed to activate the specific immune response (see eq. 2.1c) and to neutralize pathogens at per-capita rate $K(y)$. This removal rate is increased by the actions of the specific immune response, e.g. by the binding of antibodies to MG.

To incorporate the specific immune response, variables representing the maturing (y_0) and active (y) specific immune components are modeled with equations (2.1c,d). We assume the primary role of the specific immune response is to produce antibodies that enhance the efficiency of innate immune components (e.g. phagocytic cells) in removing pathogen. The first term in equation (2.1c) models the activation of the specific immune components y_0 by antigen presenting cells during an active infection. Activation is modeled using a saturating response to the level of pathogen p and innate immune activity n. Once

activated, maturation occurs at rate μ_{y0} to produce specific immune components which then decay at rate μ_y. Mathematically, the maturation process simply introduces a delay in the production of active specific immune components (e.g. antibodies).

Though not included in equations (2.1), the symptoms of disease appear to largely result from the host immune response, yet it is unknown whether these symptoms harm or benefit the pathogen, nor whether they help or hinder the immune response. For this work, we assume the immune-pathogen dynamics are largely unaffected by disease symptoms, and we assume those symptoms are generated by a combination of both pathogen and immune activity as detailed in Section 2.5.4.

2.4.1 Simplified Models & Important Subsystems

In formulating model (2.1) we have simplified the complexity of the vertebrate immune system by adopting a "top down" perspective highlighting how the immune system functions during mycoplasma infections. Many biological questions about the immune response to mycoplasmas can therefore be framed as mathematical questions about the dynamics of equations (2.1), but despite this model's relative simplicity it only permits limited mathematical analysis.

In order to understand the dynamics of model (2.1) beyond those limited analytical results, we also describe the dynamics of a suite of simpler models which either approximate equations (2.1) or are key subsystems of that model. We also provide some computational results illustrating the immune-pathogen dynamics of model (2.1) for particular parameter regimes (see Table 2.1 in the

next section).

The simplified models considered below primarily arise from the fact that different immune processes occur across a wide range of time scales (see Segel and Perelson [1991] and Appendix B.2). We may therefore assume that the non-specific immune activity (n) rapidly responds to changes in pathogen density (p), which itself changes quickly relative to the slower dynamics of the specific immune response (y).

The dynamics of these simplified models are presented in the next section as follows. The section begins by describing the pathogen dynamics in the absence of the host immune response. We then describe the dynamics of the innate response by considering the p-n subsystem in the absence of a changing specific immune response, i.e. we treat $K(y) = K_{ny}$ as a constant (see Figure 2.2). This approximates the fast time scale dynamics of model (2.1). Using standard separation of time scales techniques, we can approximate the slow time scale dynamics using a simplified model which combines the p-n dynamics into a single equation governing the pathogen dynamics and a second equation governing the dynamics of the specific immune response. This simplified, slow time scale model is accordingly referred to as the p-y model.

2.4.2 Model Parameterization

Parameter values for model (2.1) are shown in Table B.1, and are based on the unscaled model parameters shown in Appendix B.1. These values are used below to motivate certain simplifying assumptions, and to illustrate the dynamics. Each parameter represents a particular biological quantity and values for those

Variable	Value	Description
p	$0-1$	Rescaled pathogen density
n	$0-1/\mu_n$	Rescaled active innate components
y_0	$0-1/\mu_{y0}$	Rescaled maturing specific immune components
y	$0-1/\mu_y$	Rescaled active specific immune components
t	.	Rescaled damage from the immune response
Parameter	Value	Description
k_{pg}	0.1	Pathogen growth rate
k_m	$1.5\text{x}10^{-8}$	Maximum removal by local innate components
μ_p	$1\text{x}10^{-8}$	Half-saturation constant for local innate components
K_{min}	> 0	Baseline active innate pathogen removal rate
K_{max}	$> K_{min}$	Maximum removal rate, specific components present
θ	6	Determines steepness of $K(\cdot)$ at x_{ny}
x	200	Half-saturation value for activation of specific response
x_y	$8.29\text{x}10^{-6}$	Half-saturation constant for pathogen removal rate $K(y)$
k_p	$2.5\text{x}10^{9}$	Pathogen activation of the innate response
x_n	199	Half-saturation value for activation of innate response
μ_n	0.05	Rate of active innate component loss
α	6	Determines response steepness at half-saturation value x_y
μ_{y0}	0.0037	Maturation rate of specific immune components
μ_y	0.0016	Rate of specific immune component loss

Table 2.1: Variables and parameter values of the scaled model (2.1). These values are based on the unscaled model parameters in Appendix B.1, Table B.1. Time units are hours unless otherwise stated.

quantities have been chosen based on empirically derived quantities, where possible. Because relatively few details are known about the avian immune system, many parameter values were based on those in Reynolds et al. [2006]. The remaining parameter specifications were chosen to yield model dynamics similar to experimentally observed infection dynamics [Dhondt et al., 2005, 2008, Kollias et al., 2004, Sydenstricker et al., 2005, 2006].

2.5 Results

2.5.1 Establishing the Infection

The very early stages of infection are largely free from control by the host's immune response, and follow the single equation

$$\frac{dp}{dt} = k_{pg} p\,(1-p) - \frac{k_m p}{\mu_p + p}. \tag{2.2}$$

Once a naive host is inoculated (density $p(0) \ll 1$), the pathogen population must overcome the host's baseline immune defenses in order to persist and proliferate. This first line of defense is modeled by the second term in (2.2) and affects the host-pathogen dynamics in two ways: First, it may cause a strong Allee effect for the pathogen population where initial densities below a critical size p_{crit} decline towards zero instead of increasing and establishing an infection. Second, it reduces the maximum attainable pathogen density ($p_{max} \leq 1$) by decreasing the *effective intrinsic growth rate* of the pathogen (see Appendix B.3),

$$r_0 \equiv k_{pg} - k_m/\mu_p. \tag{2.3}$$

The relationship between the strength of these baseline immune defenses (i.e. the magnitude of k_m) and the two phenomena just mentioned are illustrated in Figure 2.3 and can be described as follows.

In the absence of these defenses (i.e. if $k_m = 0$), the pathogen population follows simple logistic growth towards $p_{max} = 1$ (here $r_0 \equiv k_{pg}$ is positive). Increasing the strength of the baseline immune defenses $k_m > 0$, the attracting pathogen density p_{max} decreases towards $p = 1 - \mu_p$ while a third equilibrium

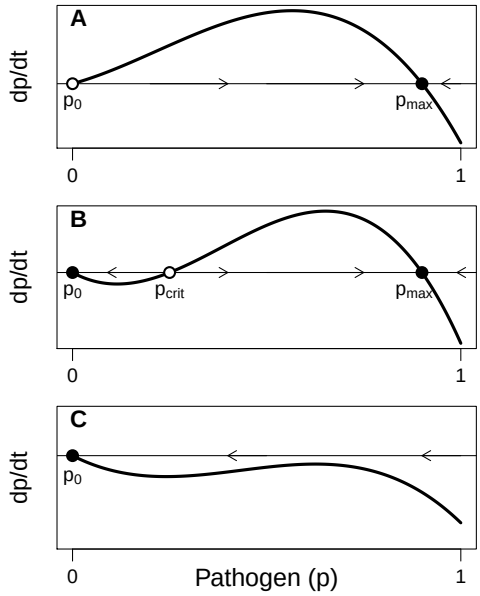

Figure 2.3: Pathogen dynamics in the absence of an active immune response (i.e. following equation 2.2). Three possibilities exist, and depend on the relative strength of the host's baseline immune defenses k_m which here increases from low (panel **A**) to very high (**C**). In panel **A**, $k_m \approx 0$ so the effective intrinsic growth rate r_0 is positive and the dynamics are similar to logistic growth. Panel **B** shows the result of increasing k_m until r_0 becomes negative. This results in a strong Allee effect (and bistability) where initial pathogen densities must be higher than p_{crit} (an unstable equilibrium) to increase towards the steady state density p_{max}. In panel **C**, further increases in k_m result in the loss of the persistence steady state p_{max}, leaving the host completely immune to infection. The transitions between these different states occur via a transcritical bifurcation (**A** to **B**) and a saddle-node bifurcation (**B** to **C**), as detailed in Appendix B.3.

value $p_{crit} < 0$ increases towards 0 and r_0 decreases towards 0. Further increasing k_m results in r_0, p_{max} and p_{crit} simultaneously passing through 0, $1 - \mu_p$ and 0 respectively (see Figure 2.3B). This leaves the threshold value p_{crit} positive, with both the maximum pathogen density p_{max} and the state of health ($p = 0$) locally attracting. A necessary condition here and in model (2.1) for having bistability with the origin is that $r_0 < 0$. Increasing k_m even further causes p_{crit} and p_{max} to move towards one another (see Figure 2.3B,C) until they meet and vanish, leaving the host completely immune to infection. See Appendix B.3 for additional

details.

The inclusion of these baseline immune defenses (i.e. assuming $k_m > 0$) can lead to interesting dynamics under model (2.1), but they also obscure how other immune components help determine different infection outcomes. To clarify the role of other immune components, results presented below first assume negligible baseline immune defenses ($k_m = 0$), and then describe how those dynamics change by including such defenses ($k_m > 0$).

2.5.2 Early Pathogen Control: Non-specific Immunity

The non-specific immune components (n) play two important roles during a newly established infection: they directly eliminate pathogen and help activate the specific immune response. During a mycoplasma infection, a susceptible host's non-specific immune response is often ineffective and requires the specific immune response to clear the infection [Simecka, 2005]. Accordingly, the non-specific immune response is important in shaping the timing, severity and persistence of infections across different hosts and host species.

To describe how the non-specific immune response shapes infection dynamics, we can approximate the fast time scale dynamics of model (2.1) by holding the specific immune response (y) constant. In the full model (2.1), y and $K(y)$ both change relatively slowly during an active infection. Defining the constant $K_{ny} = K(y)$, model (2.1) becomes

$$\frac{dp}{dt} = k_{pg} p\,(1 - p) - \frac{k_m p}{\mu_p + p} - K_{ny} n p \tag{2.4a}$$

$$\frac{dn}{dt} = \frac{n + k_p p}{x_n + n + k_p p} - \mu_n n. \tag{2.4b}$$

If baseline immune defenses are negligible (i.e. if we assume $k_m = 0$) then there is no Allee effect. An infection in this case will always approach either a positive steady-state pathogen density $p_* > 0$ and level of immune activity $n_* > 0$, or the infection will be cleared by a self-sustaining inflammatory response with steady state $n_n > 0$ (see Appendix B.3 and Reynolds et al. [2006] for details). Since self-sustained inflammatory responses are currently unknown in the motivating biological system, we will focus our attention on the persistence steady state (p_*, n_*) and ask: under what conditions is p_* significantly greater than 0?

Figures 2.4A,B (where $k_m = 0$) show how slowly increasing the net effectiveness of the immune response (K_{ny}) reduces the attracting pathogen level p_* in a nearly linear fashion until p_* is very near 0 (see arrow, Fig. 2.4B). Interestingly, any further increases in K_{ny} allow the pathogen to persist at very low levels. This persistence results from the absence of an Allee effect when $k_m = 0$ and from the very low saturation threshold ($x_n/k_p \approx 0$) for the activation of the non-specific response according to equation (2.4b) and Table 2.1. If activation of the non-specific response saturates at higher pathogen densities then this transition is far less abrupt (compare Figure panel 2.4A with C-F).

If baseline immune defenses are sufficiently strong ($k_m > 0$), these dynamics change as expected from section 2.5.1. Baseline immune defenses can induce an Allee effect that hinders or prevents the establishment of infection and allows complete pathogen clearance by the immune response. Increasing K_{ny}, the dynamic changes may be similar to the $k_m = 0$ case, however if baseline immune defenses are very strong such increases can yield a more abrupt clearance of the pathogen via a saddle-node bifurcation as shown in Figure 2.4E. These baseline

immune defenses also reduce the attracting pathogen density p_*, although this reduction is very small for biologically relevant parameter values. For more details regarding the model (2.4) dynamics see Appendix B.3.

Simplifying the *p*-*n* subsystem

In addition to our biological motivations for discussing the dynamics of the *p*-*n* subsystem (2.4), the above results help simplify model (2.1) to clarify how the specific immune response (y) shapes infection outcomes. To further simplify models (2.1) and (2.4) we make two additional assumptions. First, since self-sustained inflammatory responses are unknown in this system, we assume a negligible amount of positive feedback in the activation of the non-specific immune response, so

$$\frac{dn}{dt} = \frac{k_p p}{x_n + k_p p} - \mu_n n \tag{2.5}$$

This rules out the potential for a self-sustaining inflammatory response (see Appendix B.3.3).

Second, the non-specific immune response (n) responds rapidly to changes in other model variables for parameter values like those in Table 2.1. This fast non-specific response together with (2.5) implies that n rapidly tracks changes in pathogen density p according to the quasi-steady state value

$$\mathbf{n}(p) = \frac{1}{\mu_n}\left(\frac{k_p p}{x_n + k_p p}\right) \tag{2.6}$$

obtained by assuming the right-hand side of (2.5) equals 0 (see Appendix B.2). Hence, the dynamics of this simplified *p*-*n* subsystem can be approximated by the single equation

$$\frac{dp}{dt} = k_{pg} p\,(1 - p) - \frac{k_m p}{\mu_p + p} - K_{ny}\mathbf{n}(p)p. \tag{2.7}$$

Since equation (2.7) is a one dimensional ODE, we can analyze its dynamics completely. As detailed in Appendix B.3.3 and B.3.4, it behaves just like the simplified *p*-*n* model (eqs. 2.4a, 2.5) except there are no cycling dynamics. Any equilibrium pathogen value p_* of the simplified *p*-*n* model is necessarily an equilibrium of (2.7), thus there can be up to three equilibria in the unit interval, in addition to the origin (see Figure B.1, Appendix B.3.4). The stability of the origin depends on the sign of r_0, as expected, and no self-sustained inflammatory response is possible in the absence of pathogen (i.e. $\mathbf{n}(0) = 0$). Any equilibrium pathogen density p_* under (2.7) is locally stable if the slope of the simplified *p*-*n* model's *n*-nullcline is greater than that of the *p*-nullcline at p_*, and is unstable otherwise. The largest such equilibrium (always less than 1) is always stable when positive.

2.5.3 Pathogen Persistence and the Specific Immune Response

We next describe how the specific immune response shapes the outcome of infection when the non-specific response fails to clear the infection on its own. In doing so we address two questions: First, when does the steady state pathogen density p_* correspond to high or very low pathogen densities? Second, how do different levels of specific and non-specific immune efficacy affect p_*?

Using (2.7), we can describe the role of the specific immune response (y) in model (2.1) by making the additional simplifying assumption that the delay in activating the specific immune response is negligible. Simulation results suggest this affects the timing of the specific immune response, but has little effect on the asymptotic dynamics. These assumptions yield the simplified slow time

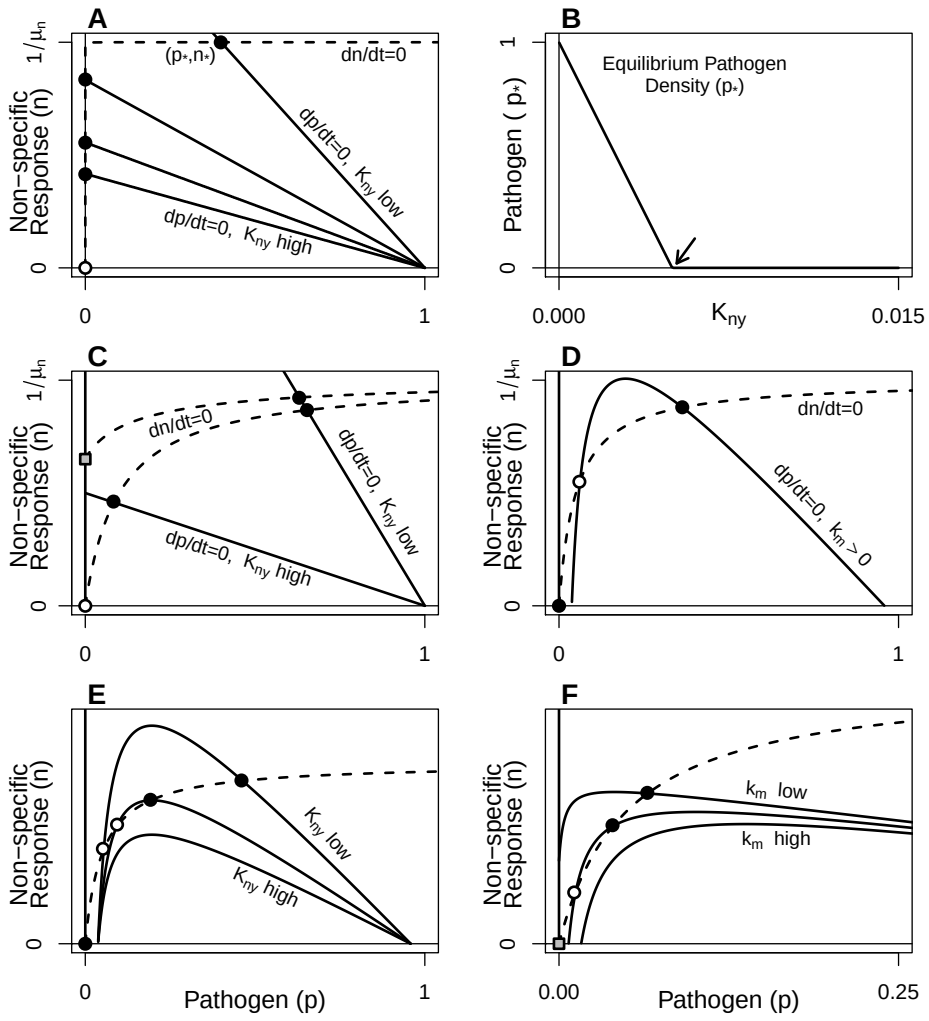

Figure 2.4: Example n- and p-nullclines (solid and dashed curve, respectively) illustrating the dynamics of the p-n subsystem (2.4). Equilibria (filled=stable, empty=unstable) occur where the nullclines intersect. Panel **A** shows the possible dynamics assuming values similar to those in Table 2.1 with $k_m = 0$ (no bistability). Panel **C** shows the nullclines and equilibria more clearly using different values. If the self-sustaining inflammatory response value $n_n \equiv 1/\mu_n - x_n$ is positive (shaded square in **C**) then either that state or the unique persistence equilibrium (p_*) is attracting depending on whether or not $p_* > 0$. If $n_n < 0$ then the only equilibria are the (unstable) origin and the (stable) persistence equilibrium p_* (see text and Appendix B.3 for stability conditions). Panel **B** shows how p_* changes with increasing immune efficiency K_{ny} assuming $k_m = 0$ and $n_n < 0$, using a broader range of K_{ny} values than shown in **A**. Panels **D**-**F** shows how assuming $k_m > 0$ introduces multiple interior equilibria ($p_*, n_* > 0$) and can lead to bistability. Panel **E** and **F** illustrate how the nullclines (and persistence equilibria) change with increasing efficiency of the specific immune response (increasing K_{ny}) and increasing strength of baseline immune defenses (increasing k_m), respectively.

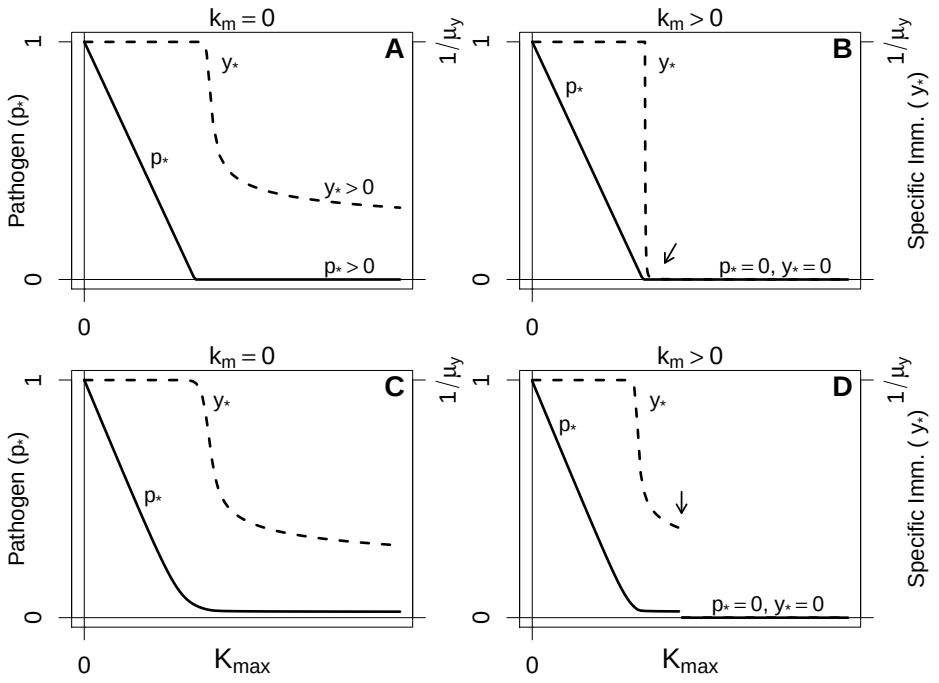

Figure 2.5: Examples of how the specific immune response efficiency (K_{max}) and an Allee effect ($k_m > 0$) shape infection outcome under the p-y model (2.8). Steady state pathogen density p_* and specific immune activity y_* are shown for a range of K_{max} values ($K_{min} = 0$). Panel **A**, **B** show the dynamics without ($k_m = 0$) and with ($k_m > 0$) an Allee effect. Panels **C**, **D** show qualitatively equivalent dynamics to **A**, **B**. Increasing K_{max}, p_* decreases almost linearly until p_* yields diminishing rates of immune activation. With no Allee effect ($k_m \approx 0$), additional increases in K_{max} permit low-level pathogen persistence and a sustained immune response ($p_*, y_* > 0$). With an Allee effect ($k_m > 0$), clearance can occur. The transition between persistence and clearance can be sensitive to parameter changes and initial pathogen densities and involves a homoclinic bifurcation that abruptly expands the basin of attraction for the pathogen-free state near the transition (see Appendix B.4, Figure B.2 for details). Parameters: See Table 2.1. Panels **B**, **D** use $k_m = 1.5\text{x}10^{-8}$ and $k_m = 4.8\text{x}10^{-4}$, respectively. Panels **C**, **D** use $x_n = 0.01k_p$, $x_y = 4.15\text{x}10^{-1}$. Initial conditions are $p(0) = 0.1$, $y(0) = 0$.

scale model

$$\frac{dp}{dt} = \left(k_{pg}(1-p) - \frac{k_m}{\mu_p + p} - K(y)\mathbf{n}(p)\right)p \tag{2.8a}$$

$$\frac{dy}{dt} = \frac{(\mathbf{n}(p)p)^\alpha}{x_y^\alpha + (\mathbf{n}(p)p)^\alpha} - \mu_y y \tag{2.8b}$$

which has a single immune response variable y. Here the efficiency of pathogen

removal $K(y)$ increases with increasing y, and the quasi-equilibrium value of the non-specific immune response $\mathbf{n}(p)$ is given by (2.6). As a working example, we assume $K(y)$ is sigmoidal

$$K(y) = \left(K_{min} + \frac{(K_{max} - K_{min})y^{\theta}}{x^{\theta} + y^{\theta}} \right) \tag{2.9}$$

where the minimum value $K(0) = K_{min}$ corresponds to the pathogen removal rate of the non-specific immune system alone ($y = 0$), and K_{max} is the maximum pathogen removal rate.

The course of infection under model (2.1) can be divided into two stages: an early acute phase largely determined by the p-n subsystem dynamics, followed by either clearance or persistence of the infection according to the dynamics of the p-y model (2.8). Whether or not an acute infection is cleared by the specific response depends largely on the efficiency of the specific response $K(y)$ and whether or not an Allee effect is present.

To describe the immune-pathogen dynamics under model (2.8) we first consider case where baseline immune defenses are negligible ($k_m = 0$, no Allee effect). In this case, there is always exactly one pathogen persistence steady state ($p_* > 0, y_* > 0$) that is always stable. More generally it can be shown that stability is guaranteed in this case whenever the activation rate of the specific immune response (first term in 2.8b), the quasi-steady state of the nonspecific immune response $\mathbf{n}(\cdot)$ and the efficiency of pathogen removal $K(\cdot)$ are all increasing functions at the equilibrium p_* (see Appendix B.4 for details). As shown in Figure 2.5A, this $p_* > 0$ may correspond to a high or very low pathogen density and requires a sustained immune response $y_* > 0$.

To highlight two transitions related to pathogen clearance and persistence, Figure 2.5 shows how the steady state pathogen density p_* changes with increas-

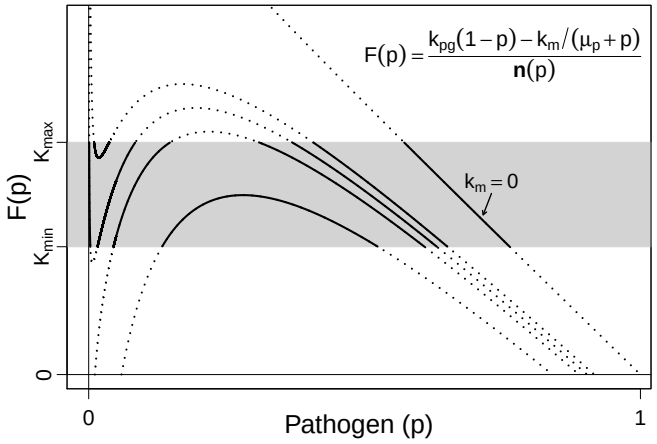

Figure 2.6: The p-nullcline $g_p(p) \equiv K^{-1}(F(p))$ (2.10a) under the p-y model (2.8) is only defined for p values where $F(p)$ (2.11) falls within the range of $K(\cdot)$ (i.e. between K_{min} and K_{max}, shaded gray above). If baseline immune defenses are negligible ($k_m = 0$, top curve), the domain of $g_p(p)$ is a single interval and the shape of $g_p(p)$ reflects the shape of $K(y)$ (cf. Fig. 2.7A). If $k_m > 0$, the domain of $g_p(p)$ may include two or more intervals (see the middle three curves). Over the lower interval(s) $g_p(p)$ is typically increasing (see Fig. 2.7D), or may have a local minimum between vertical asymptotes (see second highest curve here, and solid black curve in Fig. 2.7B). Where $g_p(p)$ is defined, it is increasing (or decreasing) wherever $F(p)$ is increasing (or decreasing, respectively), since $K^{-1}(\cdot)$ is strictly increasing on its domain $[K_{min}, K_{max})$.

ing K_{max} in the presence or absence of an Allee effect. Increasing K_{max} from near K_{min} initially gives a near-linear decrease in pathogen density p_*. Eventually, p_* is small enough to decrease immune activation rates below their saturation thresholds. Beyond this transition, immune activity (y_*) decreases but pathogen density p_* changes little (see Fig 2.5A,C).

The presence of an Allee effect ($k_m > 0$, Fig. 2.5B,D) introduces the potential for a second, more abrupt transition (see Fig. 2.5D) associated with a homoclinic bifurcation described in Appendix B.4.2. Similar to Figure 2.4E, increasing K_{max} increases the Allee threshold and decreases p_*. Here, however, the basin of attraction for the pathogen-free state ($p = 0$, y= 0) can very suddenly grow to

encompass nearly all biologically plausible initial conditions. Beyond this transition, the outcome of infection is complete clearance of the pathogen following the acute phase of infection.

Importantly, whether the outcome of infection is clearance or low-level persistence will have major consequences for the host when disease symptoms are immune mediated, or when the immune response is otherwise costly (compare the two cases in Figure 2.5). Under such circumstances, immune-mediated disease symptoms may increase host mortality risk or otherwise impact host fitness during persistent infections despite very low pathogen levels.

To more precisely describe how these dynamics depend on model parameters we next consider the nullclines of (2.8)

$$g_p(p) = K^{-1}\left(\frac{k_{pg}(1-p) - \frac{k_m}{\mu_p + p}}{\mathbf{n}(p)}\right) \tag{2.10a}$$

$$g_y(p) = \frac{1}{\mu_y}\frac{(\mathbf{n}(p)p)^\alpha}{x_y^\alpha + (\mathbf{n}(p)p)^\alpha} \tag{2.10b}$$

where $K^{-1}(\cdot)$ is the inverse of $K(y)$.

For $k_m \geq 0$, the y-nullcline $g_y(p)$ is a monotone increasing function of p (approximately sigmoidal) with maximum value $1/\mu_y$. The shape of the p-nullcline $g_p(p)$ is more variable due to the bounded nonlinear function $K(y)$.

To see how different parameters shape the p-nullcline 2.10a, define

$$F(p) = \left(k_{pg}(1-p) - \frac{k_m}{\mu_p + p}\right)/\mathbf{n}(p) \tag{2.11}$$

so that the p-nullcline can be written as $g_p(p) = K^{-1}(F(p))$. Since here $K(y)$ is a nonlinear (sigmoidal) function with the finite range $[K_{min}, K_{max})$, it follows that $K^{-1}(\cdot)$ is also nonlinear and that $g_p(p)$ is only defined for values of p where $F(p) \in [K_{min}, K_{max})$. Figure 2.6 illustrates how this restricts the domain of $g_p(p)$ which

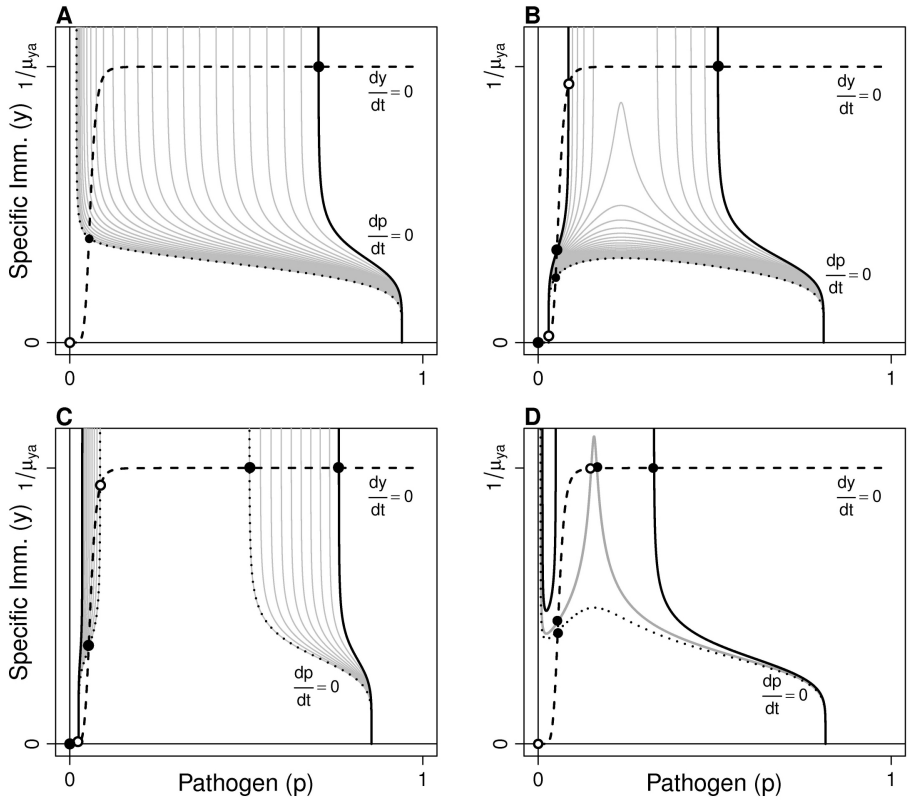

Figure 2.7: Nullclines of the p-y model (2.8) illustrating the kinds of dynamics possible when $k_m = 0$ (panel **A**) and when $k_m > 0$ (panels **B-D**). Multiple instances of the p-nullcline (solid curves) are shown but only one instance of the y-nullcline (dashed curve). Gray curves indicate how the p-nullcline changes as K_{max} is increased with the solid black curve corresponding to the lowest value of K_{max} and the dotted curve the highest. Note vertical asymptotes at some boundaries of the p-nullcline's multi-interval domain (see Figure 2.6).

for $K(\cdot)$ given by (2.9) results in a discontinuous p-nullcline defined on a domain of 1-3 disconnected intervals.

Figure 2.7 shows multiple instances of the p-nullcline (solid curves) for a range of K_{max} values. If baseline immune defenses are negligible ($k_m = 0$) the p-nullcline (2.10a) is a decreasing function with domain $(p_{lo},\ p_{hi}]$. If $k_m = 0$ then $F(p)$ is linear, so for any strictly increasing function $K(\cdot)$ with range $(K_{min},\ K_{max}]$, p_{lo} is determined by K_{max} (i.e. p_{lo} decreases as K_{max} is increased) and p_{hi} is deter-

mined by K_{min} (see the $k_m = 0$ curve, Figure 2.6). As shown in Figure 2.7A, the p-nullcline intercepts the p axis at p_{hi} and approaches ∞ on the lower end of this domain as p decreases towards p_{lo}.

If $k_m > 0$ (see the four lower curves in Fig. 2.6 and see Fig. 2.7B,D) the p-nullcline can be highly nonlinear which allows the p-y model to have multiple equilibria associated with low pathogen levels and instances of bi- and multi-stability including bistability between the persistence steady state and the origin (see Figure 2.7). Some of these equilibria can undergo a Hopf bifurcation resulting in low-level pathogen-immune cycling, although simulations suggest cycling dynamics are rare or of small amplitude for biologically relevant parameter values. In dynamical systems terms, these new dynamics arise from transcritical bifurcations involving the origin, from saddle-node bifurcations in the interior of the positive quadrant, and from other bifurcations associated with a homoclinic bifurcation near a generalized Hopf bifurcation (see Appendix B.4).

These results suggest the following about the immune-pathogen dynamics under the simplified model (2.8) and model (2.1). First, pathogens with higher growth rates k_{pg} will have both higher steady state pathogen density p_* and result in more immune activity y_*. Second, low pathogen removal rates (e.g. reduced $K(y)$) yield both higher pathogen load and elevated immune activity. These results also highlight the synergistic nature of how the vertebrate immune system responds to infection, and the potential for nonintuitive dynamics to arise from even relatively simple models of that response.

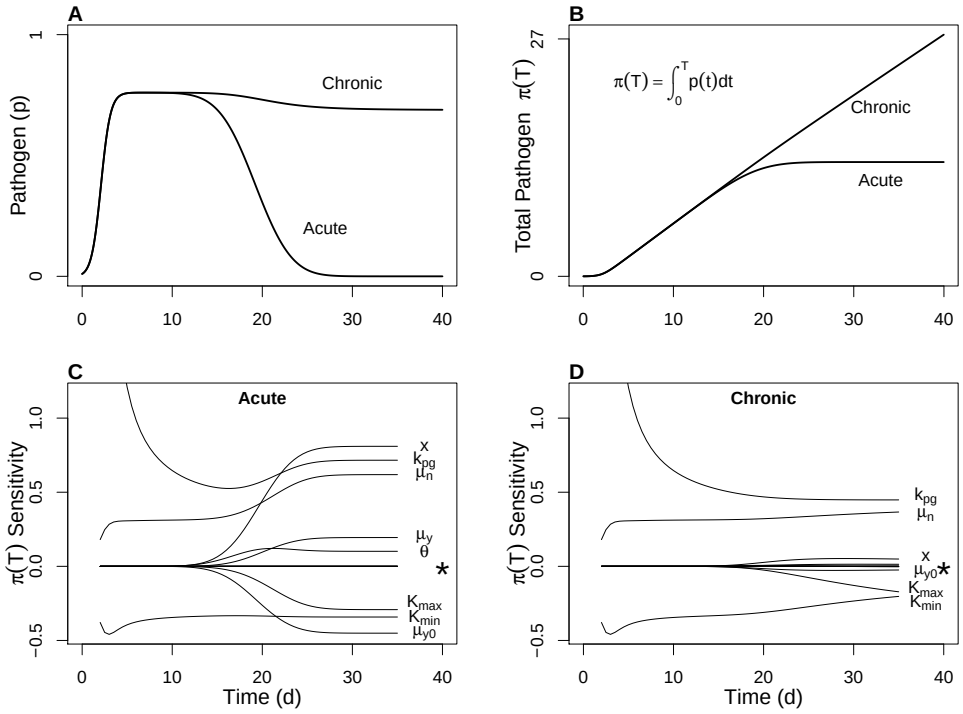

Figure 2.8: Sensitivity profiles for model (2.1) showing how pathogen fitness (total pathogen load $\pi(T)$ (2.12)) responds to small changes in the parameter values in Table 2.1 with $K_{min} = 0.0012$. Sensitivities are shown for a range of times T, as total pathogen load depends on the duration of infection which may be shortened by host death. Panel **A** shows pathogen dynamics for an acute infection ($K_{max} = 0.0075$) and a persistent (chronic) infection ($K_{max} = 0.00156$). Panel **B** shows the total pathogen load for each case. The curves in **C**, **D** are relative sensitivities for each parameter, computed over a range of T values (see text). Here * indicates parameters with sensitivities near 0. The primary determinants of infectiousness in this case are related to the pathogen growth rate and the timing and strength of the specific and non-specific immune responses. Parameters used: k_{pg}, k_m, μ_p, K_{min}, K_{max}, α, x, x_y, k_p, x_n, μ_n, θ, μ_{y_0}, and μ_y.

2.5.4 Determinants of Host Infectiousness and Mortality Risk

We would like to know which pathogen and host characteristics most affect pathogen fitness (host infectiousness) and host fitness (host mortality risk). To quantify fitness, we define two important quantities. First, we assume host infectiousness is given by total pathogen load (pathogen fitness) over the duration

of the infection, given by

$$\pi(T) = \int_0^T p(t)dt \tag{2.12}$$

where time T is when the host dies or recovers. Second, to quantify host survival we model host death as a random process. In house finches, host mortality risk is increased by the tissue damage and inflammation caused by the interaction between host immune components and pathogen [Faustino et al., 2004, Hochachka and Dhondt, 2000]. We therefore define the time an infected host dies as the random variable T_{death}, given by

$$\mathcal{P}(T_{death} \leq T) = \exp\left(-\int_0^T \lambda(t)dt\right) \tag{2.13}$$

where the mortality rate $\lambda(t) = cU(t)$ is assumed to be given by the total pathogen removal rate $U = K(y)np$ (a proxy for disease symptoms) times a constant c. We quantify the effect of disease on host fitness using the probability of surviving to day $T = 40$, given by

$$\mathcal{P}_s \equiv \mathcal{P}(T_{death} \leq 40). \tag{2.14}$$

To identify which pathogen and host characteristics most strongly influence our two fitness quantities $\pi(T)$ and $\mathcal{P}_s$, a sensitivity analysis is used to determine how they change with changing parameter values. Since the duration of infection T (time to host recovery or death) is highly variable and because c is largely unknown, we show these parameter sensitivities as curves over a range of T and c values, or as *sensitivity profiles* with respect to T or c. Here the (relative) sensitivity of quantity R to changes in parameter q is

$$S_q(R) = \frac{\partial R}{\partial q}\frac{1/R}{1/q}. \tag{2.15}$$

Pathogen fitness sensitivities for two instances of model (2.1) are shown in Figure 2.8. The comparison between parameter sensitivities before and after

control by the specific immune response ($T \approx 15$ in Fig. 2.8C) suggests that whether or not individual pathogen characteristics are likely to respond to selection depends on whether transmission typically occurs before or after the specific immune response. If the host dies or otherwise ceases to be infectious prior to the specific response, pathogen fitness is most sensitive to changes in the pathogen's intrinsic growth rate k_{pg}, the loss rate of non-specific immune components μ_n and the effectiveness of the non-specific immune response in removing pathogen K_{min}. Otherwise, if the majority of hosts resolve their infections selection may act on additional pathogen characteristics that affect the activation rate of the specific response or its effectiveness in removing pathogen.

To identify the host and pathogen characteristics that influence host survival, we consider the relative sensitivity of host survival $\mathcal{P}_s$ (2.14) to changes in parameters over a range of virulence scalar values, c. Note from (2.13), (2.15) and our definition of $\lambda(t) = cU(t)$ that these sensitivities scale with c since

$$S_q(\mathcal{P}_s) = -cq\frac{\partial}{\partial q}\left(\int_0^T U(t)dt\right) \tag{2.16}$$

for any parameter q. Figure 2.9A shows the immune-pathogen interaction curves proportional to mortality rate $\lambda(t)$ (see eq. 2.13) for the two cases shown in Figure 2.8. Figure 2.9B shows the associated survival probabilities $\mathcal{P}_s$. Their parameter sensitivities (Figure 2.9C,D) suggest that host characteristics affecting the timing and strength of the immune response (i.e. μ_n, x, K_{max}, K_{min}, μ_y and μ_{y0}) may respond to disease-induced selection as would host characteristics that affect the pathogen growth rate k_{pg}.

From the perspective of the pathogen, the above immune-pathogen dynamics lead to a natural transmission-virulence tradeoff as illustrated in Figure 2.10.

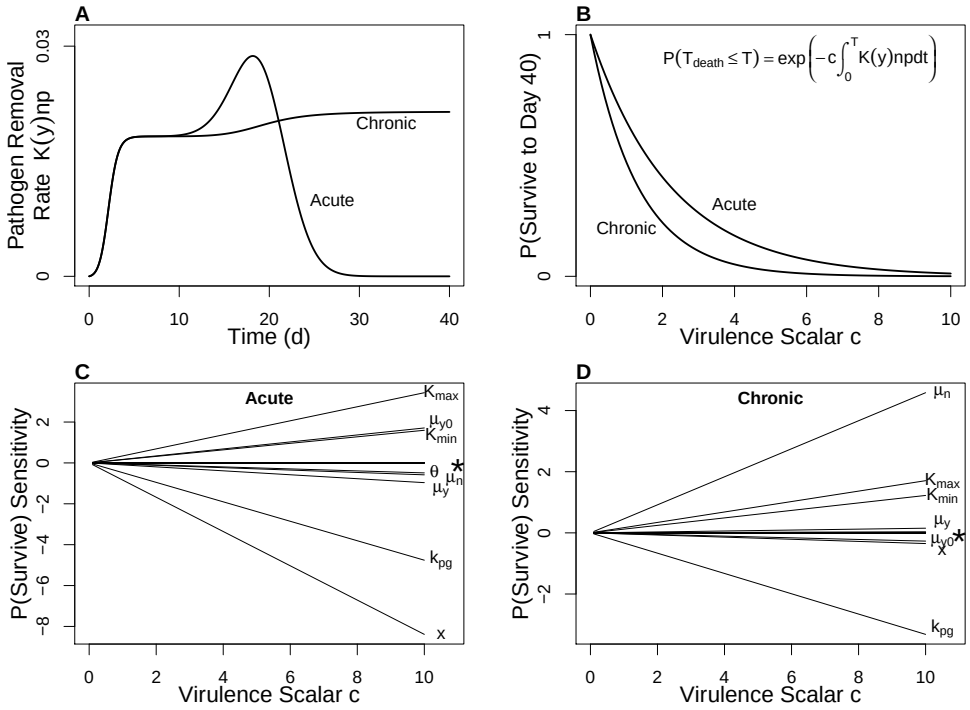

Figure 2.9: Sensitivity profiles for the probability of surviving to day 40, $\mathcal{P}_s$, under model (2.1) showing how host survival responds to small changes in the parameter values in Table 2.1. Panel **A** shows a measure of the immune-pathogen activity ($K(y)np$) corresponding to the two cases in Figure 2.8A. Panel **B** shows how $\mathcal{P}_s$ depends on c where $\lambda(t) = cK(y)np$. Panels **C** and **D** show approximate parameter sensitivities computed over a range of c values (see text for why these scale with c). Here * indicates parameter sensitivities that are approximately 0. Parameters used: k_{pg}, k_m, μ_p, K_{min}, K_{max}, α, x, x_y, k_p, x_n, μ_n, θ, μ_{y_0}, and μ_y.

Assuming variation only in the pathogen growth rate k_{pg} and using the "acute" immune-pathogen dynamics shown in Figures 2.8 and 2.9, we can compute the average relationship between transmission and virulence as shown by the black curve in Figure 2.10.

These results highlight two key aspects of this system. For host and pathogen, the evolutionary consequences of transmission-mediated and/or host-mortality-mediated selection may depend heavily on whether transmission and mortality typically occur before or after the action of the specific im-

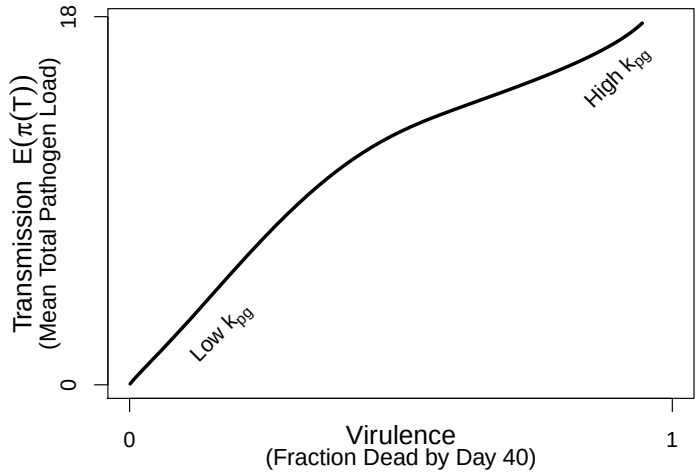

Figure 2.10: Transmission-virulence relationship arising from variation in the pathogen growth rate k_{pg}, using the relationship between host disease state and mortality rate as described in Figure 2.9. This positive relationship indicates the existence of a transmission-virulence tradeoff for the pathogen. Here k_{pg} increases from 10% to 500% of the value given in Table 2.1. For each value of k_{pg}, the distribution (2.13) was used to compute $E(\pi(T))$ and $\mathcal{P}_s$ (see Fig. 2.9 and the text). Parameter c was chosen to yield $\mathcal{P}_s$ = 60% for the value of k_{pg} given in Table 2.1.

mune response [cf. Osnas and Dobson, 2010]. This fact may be important for chronic diseases like those caused by mycoplasmas. Second, any symptoms-driven selective forces acting on the host likely affect both the effectiveness and the timing of the specific immune response as well as the effectiveness of the non-specific response. Since host symptoms are at least partially driven by host immune activity, the direction of selection on host immune characteristics will likely be determined by their net impact on survival.

2.6 Discussion

One goal of this investigation is to identify which host and pathogen characteristics contributed most to within and between host species variation in disease progression, and what aspects of that variation are not well explained by a simple model of the pathogen-immune interaction. This model exhibits four qualitatively different outcomes of infection with respect to pathogen dynamics: 1) no pathogen proliferation due to effective baseline immune defenses or a relatively low pathogen growth rate, 2) a brief increase in pathogen density allowed by ineffective baseline defenses then clearance by the non-specific immune response, 3) a more prolonged period of elevated pathogen density (resulting from an ineffective non-specific response) that is eventually cleared by the specific immune response, and 4) long-term pathogen persistence despite a sustained specific immune response. Our results suggest that key determinants of these different infection outcomes include the pathogen growth rate (k_{pg}) relative to the host's baseline immune defenses, the ability of non-specific and specific immune components to remove pathogen, and other host characteristics affecting the activation and maintenance of various immune components.

Figure 2.11 compares data from Figure 2.1 with model output showing variation in three parameters that most affect pathogen load early during infection (see Appendix B.5 for additional figures). This suggests that much of the variation between infections in house finches likely results from non-specific immune components (e.g. MACs) that are variously unable to control *M. gallisepticum* infections, and perhaps from a delayed or mildly inefficient specific immune response. Importantly, variation in the timing of the specific immune response could also be caused by non-specific immune components involved in activat-

ing and regulating the specific immune response. Another important source of variation between species is the pathogen growth rate, which may be species-specific, may differ between strains of *M. gallisepticum*, and may be influenced by environmental mediators such as temperature. The role of the non-specific immune response in our model is consistent with what is known about other mycoplasma diseases, suggesting that the results presented here may also apply to other host species, not just the house finch. For example, the house sparrow (*Passer domesticus*) is know to have a strong non-specific immune response compared to related species [Lee et al., 2005, Lee, 2006, Martin II et al., 2004] and clears MG infections rapidly [Dhondt et al., 2008].

In the model presented above, we tacitly assume that different infection outcomes arise from differing host and/or pathogen characteristics. Another interpretation of these results is suggested by how MG and other mycoplasma species interact with their hosts. The outcome of MG infection can be influenced by the nature of the initial contact with pathogen [e.g. Dhondt et al., 2007]. Some mycoplasmas are known to actively manipulate the the host immune response, making it more ineffective and harmful to the host [Citti et al., 2005, Simecka, 2005]. Accordingly, an alternative to interpreting different model parameterizations as fixed individual- or species-level characteristics is to view them as characteristics of a single infection that arise from a multitude of factors including the host's attempt to mount an effective specific immune response and the pathogen's attempt to manipulate that response. Future work comparing the results presented here with models that include more detailed immune regulatory mechanisms may suggest experimental means of determining whether or not immune manipulation plays an important role in these systems.

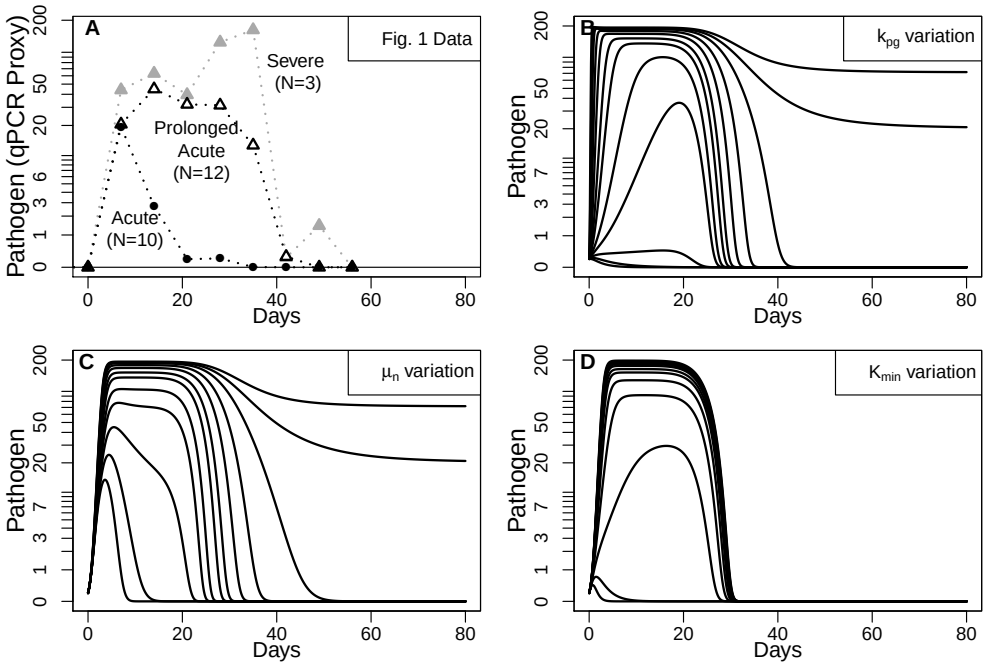

Figure 2.11: Comparison between empirically observed pathogen load variation (panel **A**, from Figure 2.1D), and pathogen load variation under model (2.1) arising from either variation in pathogen (**B**) or host (**C,D**) characteristics. The pattern of variation in the data (**A**) appears more similar to some patterns of host variation (e.g. **C**) than it does to the pattern arising from pathogen growth rate variation (**B**). This is consistent with host heterogeneity being an important source of variation in this system. Moreover, these comparisons suggests that the bulk of the observed variation involves the hosts' non-specific immune response. Each parameter shown varies from 5% to 700% of the value given in Table 2.1, with K_{min} = 1.2x10^{-3}, K_{max} = 2.25x10^{-2}, μ_{y0} = 1.5x10^{-3} (to better match the timing of the specific response) and pathogen density p scaled by 200 for plotting model output on the same log-scale as the data. See Figure B.3 in Appendix B.5 for similar figures where other parameters are varied.

A second goal of this investigation is to identify pathogen and host-immune characteristics likely to affect host infectiousness (pathogen fitness) and mortality risk (host fitness) to help inform the empirical study of selection in this system. According to the sensitivity profiles shown in Figure 2.8, the nature of the selective forces acting on the pathogen depends strongly on whether transmission occurs before or after the specific immune response. Assuming trans-

mission typically occurs early during infections, the characteristics that likely drive pathogen fitness are the pathogen growth rate k_{pg} and any ability of the pathogen to manipulate the non-specific immune response (i.e. to reduce K_{min} and K_{max}). A more complete picture of how host fitness is affected by immune status and pathogen load is needed to give reliable predictions regarding selection on host characteristics. However, if host fitness depends on total immune activity as detailed in the Results section, we would expect selection to act on characteristics associated with an early and efficient immune response (i.e. non-specific immune components) and immune-driven disease symptoms (e.g. inflammatory mediators).

This work suggests that certain molecular and cellular level data should help clarify the relationships between mycoplasma, host epithelial tissues, host immune cells and the symptoms associated with MG infection in house finches. More specifically, data are needed that shed light on the regulation of various immune components and inflammation, and how MG affects these regulatory processes, in avian hosts. Similar data are also needed to establish whether disease symptoms (i.e. tissue inflammation) affect pathogen growth and host immune function, as such feedbacks might affect the results obtained under model (2.1). Using mechanistic models such as these to incorporate molecular-, cellular- and organism-level data should clarify our understanding of the complex interactions between mycoplasmas and their hosts.

APPENDIX A

APPENDIX OF CHAPTER 1

A.1 Model Derivation

The general model (1.1) is a rescaled version of the following model, which is based on spore-based fungal parasitism of *Daphnia sp.*

As described in the text, we begin with a Rosenzweig-MacArthur model with a general predation rate $\tilde{\alpha}(N)N$. Among consumers, we incorporate constant rates of fish predation and a spore-based infectious disease using an "SIZ" model used previously for this system. Spore-based disease transmission largely follows the law of mass action in this systems and others [Ebert, 2005, Ch. 8]. Importantly, we allow for N-dependent contact rates between consumers and spores, and N-dependent production of spores by infected individuals by assuming general N-dependent rates $\tilde{\beta}(N)$, $\tilde{\sigma}(N)$ and $\tilde{C}(N)$. These yield the general (unscaled) model which has units of individuals L^{-1} and time in days.

$$\frac{dN}{d\tau} = \tilde{r}N(1 - N/K) - \tilde{\alpha}(N)N(X + \rho Y) \tag{A.1a}$$

$$\frac{dX}{d\tau} = \chi\tilde{\alpha}(N)N(X + \tilde{f}\rho Y) - (d_x + \tilde{m})X - \tilde{\beta}(N)XZ \tag{A.1b}$$

$$\frac{dY}{d\tau} = \tilde{\beta}(N)XZ - (d_x + \tilde{\nu} + \tilde{m})Y \tag{A.1c}$$

$$\frac{dZ}{d\tau} = \tilde{\sigma}(N)(d_x + \tilde{\nu})Y - \tilde{\mu}Z - \eta\tilde{C}(N)Z(X + \rho Y) \tag{A.1d}$$

Table A.1 contains parameter descriptions, ranges and values. Note that to parameterize the N-dependent rates $\tilde{\beta}(N)$, $\tilde{\sigma}(N)$ and $\tilde{C}(N)$ we rescale the model assuming they are constant, then parameterize their N-dependent functional

forms relative to their constant-rate counterparts. Finally, where parameter values were practically unknown, we attempted to choose values that are biologically plausible, and that yield dynamics consistent with field and laboratory observations.

The rescaled model (1.1) is given by: $t = \frac{\tau}{\frac{1}{d_x}}$, $r = \frac{\tilde{r}}{d_x}$, $\alpha = \frac{\chi\tilde{\alpha}}{d_x}$, $k = \tilde{k}/K$, $f = \tilde{f}\rho$, $m = \frac{\tilde{m}}{d_x}$, $C = \eta\tilde{C}\chi K\frac{1}{d_x}$, $C_c = \eta\tilde{C}_c\frac{\chi}{d_x}$, $\beta = \tilde{\beta}\chi K\frac{1}{d_x}$, $\nu = \frac{\tilde{\nu}}{d_x}$, $\sigma = \tilde{\sigma}$, $\mu = \frac{\tilde{\mu}}{d_x}$. This leaves the rescaled variables as $n = N/K$, $x = \frac{X}{\chi K}$, $y = \frac{Y}{\chi K}$, $z = \frac{Z}{\chi K}$. See Table 1.1 in the text for parameter descriptions.

A.2 Parameter Values

Parameter values and ranges below were determined based upon their biological interpretations, using published values of those quantities when available. Other values come from previously published models of *Daphnia* parasitism or algae consumption. Within biologically plausible parameter ranges, certain parameter values were further specified in order to replicate observed phenomena or produce specific dynamic behaviors.

Algal growth and consumptions rates are based on the wide range of natural variability in green algae and their interactions with *Daphnia*. Intrinsic growth rate $\tilde{r}$ is based on doubling times ($1-4$ doublings day^{-1}) for green algae [Sorokin and Krauss, 1958, others] and maximum algal densities are based on naturally occurring levels during typical algal blooms.

Daphnia feeding (or filtering) rates were based on previously published population growth rates and observed feeding rates [Hall et al., 2007, Duffy et al., 2005, Porter et al., 1982, for example], though such rates in reality likely depend on other factors including temperature and food quality and thus are only loosely defined here. Under the units of mg dry weight L^{-1} (as in Hall et al. [2007]) we have maximum consumption rates $a \approx$ 1-2 orders of magnitude smaller than $N < K$, with k roughly the same order of magnitude as K, though slightly smaller. Based on [Duffy et al., 2005] where the maximum birth rate was 0.4 d^{-1} (with generation times of $1-3$ weeks) we can assume the maximum birth rate (χa) is equal to $b_{max} = 0.4d^{-1}$ from [Duffy et al., 2005], which implies (by $a \approx 10^2$ above) that $\chi = 0.4\text{x}10^{-2}$.

Disease parameters were taken from previously published modeling work

by Hall, Duffy and others. According to [Hall et al., 2006], the mass action infection rate is $\beta = 3\text{x}10^{-6}$ L^{-1} day^{-1} with spores produced at $\sigma = 6.4\text{x}10^{4}$ spores per dead infected host per day. With the other parameters given in Table A.1, this yields an $R_{0,dis}$ only slightly larger than 1 (though simulation suggests that this doesn't guarantee disease persistence in the presence of producer-consumer cycles). Thus, the spore-based infection rate was allowed to be somewhat flexible in order to attain prevalence levels consistent with those observed in naturally occurring *Metschnikowia bicuspidata* epizootics.

The maximum per consumer filtering rate (in L day^{-1}) for *D. magna* is taken from Figure 1 in [Porter et al., 1982] which suggest nearly 4 mL per hour. Converting to the proper units and rounding yields approximately 0.1 L day^{-1} = $\frac{\tilde{C}_c}{k}$. With the above, we compute $\tilde{C}_c$ as $0.1k$.

Variable	Value	Range	Description (Units)
N	–	–	Producer density (No. L^{-1})
X	–	–	Susceptible consumer density (No. L^{-1})
Y	–	–	Infected consumer density (No. L^{-1})
Z	–	–	Infectious spore density (Spores L^{-1})
τ	–	–	Time (days).
Parameter	Value	Range	Description
K	10^4	10^2 - 10^9	Algal carrying capacity (No. L^{-1}) [Porter et al., 1982, others]
$\tilde{r}$	2	0.69 – 2.8	Algal growth rate (No. d^{-1}) [Sorokin and Krauss, 1958]
$\tilde{a}$	3.16x10^2	$\approx \frac{K}{100} - \frac{K}{10}$	Max. consumption rate [Hall et al., 2007]
$\tilde{k}$	0.6x10^4	–	Half saturation constant for type-II $\alpha(n)$ [Hall et al., 2007]
ρ	1	–	Relative feeding rate of infecteds
f	0.75	0 – 1	Relative fecundity of infecteds
χ	0.4x10^{-2}	–	Births per consumed producers [Duffy et al., 2005]
d_x	0.05	0.02 – 0.1	*Daphnia* mortality $\approx$ lifetime^{-1} (No. day^{-1})[Duffy et al., 2005]
$\tilde{m}$	0.03	0 – 0.5	Fish predation rate (Indiv day^{-1}) [Duffy et al., 2005]
$\tilde{C}$	0.1	≤ 0.1	Consumption rate (type-I $\alpha(n)$) (L day^{-1} consumer^{-1})
$\tilde{C}_c$	500	0 – 1000	Max. $C(n)$ (type-II $\alpha(n)$) [Porter et al., 1982]
η	0.7	0 – 1	Spore consumption efficiency
$\tilde{\beta}$	–	≥ 0	Infection rate (fit to yield ≤20% prevalence) [Hall et al., 2006]
$\tilde{\beta}_c$	–	≥ 0	Per capita per spore infection rate
$\tilde{\nu}$	d_x	$\approx d_x$	Additional non-fish-related mortality for infecteds
θ	3	1 – 10+	Fish selectivity Duffy et al. [2005], Hall et al. [2006]
$\tilde{\mu}$	0.033	≥ 0	Loss rate of infectious spores (No. L^{-1}) [Hall et al., 2006]
σ	6.4x10^4	0 – 10^5	Spores produced per dead infected individual [Hall et al., 2006]

Table A.1: Parameter values and descriptions for the unscaled model. Units are individuals L^{-1}, time is in days. The broad range for d is based on the broad range of algal densities observed in nature. Growth rate r based on daily doubling range of 1 – 4 doublings per day from [Sorokin and Krauss, 1958]. For other parameters, see the references indicated in the table.

A.3 Computing Equilibria & Disease-Free Dynamics

In its most general form, model (1.1) offers little analytical insights. As what little analysis it does allow can be useful for computational explorations, we include them here.

A.3.1 Disease-free States & Their Stability

The disease-free dynamics can be understood using the disease-free model

$$\frac{dn}{dt} = rn(1-n) - A(n)x, \qquad \frac{dx}{dt} = (A(n) - (1+m))x$$

where for any non-negative-valued differentiable $\alpha(n)$, we denote the per-consumer rate of consumption by $A(n) = \alpha(n)n$. Let $A^{-1}(s)$ be the (possibly empty) set of n values such that $A(n) = s$, then we can describe the disease-free attractors as follows.

$$EQ_0 = [n = 0, x = 0, y = 0, z = 0], \; EQ_n = [n = 1, x = 0, y = 0, z = 0]$$
$$EQ_1 = \left[n_1 = A^{-1}(1+m), x_1 = \left(\frac{r}{1+m}\right) n_1 (1-n_1), y = 0, z = 0\right].$$

The origin is always unstable since $r > 0$ by assumption. Since $A(0) = 0$, EQ_n is (locally) stable only if $R_{0c} < 1$, where $R_{0c} = \frac{A(1)}{(1+m)}$. The existence and stability of EQ_1 are given as follows. If $A(n)$ is differentiable and non-decreasing over the unit interval, and $A(0) = 0$ then there exists a biologically relevant (and unique) EQ_1 if and only if $A(n_1) = 1 + m$ has a (unique) solution $n_1 \in (0, 1)$. Local stability conditions for biologically relevant EQ_1 can be written in terms of the elasticity $E_A = \frac{dA(n)}{dn}\frac{n}{A(n)}$ evaluated at n_1, or equivalently $E_\alpha = E_A - 1$ (since $A(n) = \alpha(n)n$). The first requirement for stability of EQ_1 is that $A(n)$ be increasing at n_1 ($E_A > 0$).

The second is that either (1) $E_A \geq 1$, or (2) if $0 < E_A < 1$ ($-1 < E_\alpha < 0$) then EQ_1 is stable when $n_1/(1-n_1) > -E_\alpha$. Stability is lost via a Hopf bifurcation when this criterion fails.

Assuming a type-II functional response $A(n) = an/(k+n)$, then $E_A = k/(k+n_1)$, $n_1 = k/(a/(1+m)-1)$, and $R_{0c} = \frac{a}{(k+1)(1+m)}$. In order for $0 < n_1 < 1$, it is necessary that $R_{0c} > 1$. Since the Hopf bifurcation occurs when the stability condition $n_1/(1-n_1) > 1-E_A$ fails, we can substitute $a/(1+m) = R_{0c}(1+k)$ into the expression for n_1 and simplify this inequality (assuming $R_{0c} > 1$) to the equivalent stability condition $R_{0c}(1-k) < 1$. Therefore, (1) a Hopf bifurcation can only occur if $k \in (0,1)$ and (2) defining $R_H = 1/(1-k)$ then the loss of stability of EQ_1 via a Hopf bifurcation coincides with the transition from $1 < R_{0c} < R_H$ to $1 < R_H < R_{0c}$.

A.3.2 Endemic Disease Equilibrium EQ_2

In the type-I constant rates case, the equilibrium point EQ_2 can be solved for by solving the system of equations $\dot{x} = 0$, $\dot{y} = 0$, $\dot{z} = 0$ for $x \neq 0$, $y \neq 0$, and $z \neq 0$, each in terms of n. Substituting these expressions back into n yields a quadratic equation in which only one root could potentially be in $(0,1)$ given the biological constraints on the parameters. Thus, for the constant rates model *with constant* $\alpha(n) = \alpha$,

$$EQ_2 = \left(n_2 = \frac{1}{2}\left(A_1 - \sqrt{A_1^2 + A_0}\right),\ x_2 = \frac{V}{B},\ y_2 = x_2 \frac{\alpha n_2 - (1+m)}{V - \alpha n_2 f},\ z_2 = y_2 \frac{(1+\nu)\sigma}{\mu} \right)$$

where $V = (1 + m\theta + \nu)$, $A_1 = \left(1 + \frac{V}{f}\left(\frac{\alpha\mu(1-f)}{\beta\sigma r(1+\nu)} + \frac{1}{\alpha}\right)\right)$, $A_0 = \frac{4V}{f}\left(\frac{(V-(1+m))\mu}{\beta\sigma r(1+\nu)} - \frac{1}{\alpha}\right)$, and $B = \frac{(1+\nu)\sigma\beta}{\mu}$. As mentioned in the text, this EQ_2 may not be the only such equilibrium in the variable rates case depending on the chosen form of $\alpha(n)$, $\beta(n)$ and $\sigma(n)$. Using forms that allow multiple interior equilibria, parameterizing

the variable rates model by equilibrium matching requires some care to ensure valid comparisons between models.

The endemic disease equilibrium EQ_2 for the more general full model (with $C(n) = 0, \rho = 1$) has no intelligible closed form, however the expressions for x_2, y_2 and z_2 in terms of n_2 given above still hold. Therefore EQ_2 can be solved for numerically by substituting these expressions into $\frac{dn}{dt}\frac{1}{n} = 0$, which can then be solved (computationally) to check for roots in the interval $(n_1, 1)$.

Note that when matched at EQ_2 the values n_2, x_2, and y_2 here are exactly as in the reduced model (1.6) with $z_2 = y_2\frac{\sigma(n_2)(1+\nu)}{\mu}$ since that model was derived using the condition $\frac{dz}{dt} = 0$.

Necessary conditions to check whether the consumer and disease both persist at equilibrium are as follows. Under model (1.1), $x_2, y_2 > 0$ if and only if (1) $V - \alpha(n_2)n_2 f > 0$ and (2) $\alpha(n_2)n_2 - (1+m) > 0$ (together, equivalent to $n_1 < n_2 < \frac{V}{\alpha(n_2)f}$) since the proportion infected at equilibrium is given by

$$\frac{y_2}{x_2 + y_2} = \frac{\alpha(n)n - M}{\alpha(n)n - M + V - \alpha(n)nf}.$$

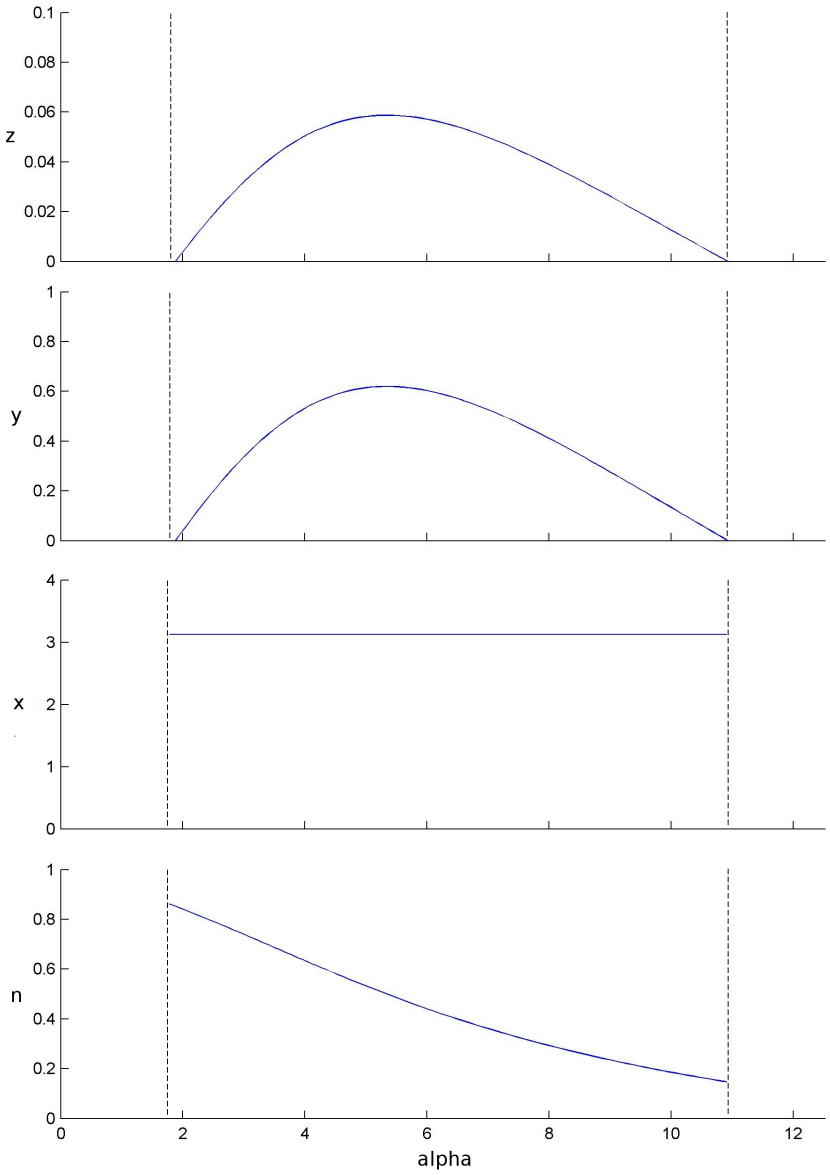

Figure A.1: The values of $EQ_2 = (n_2, x_2, y_2, z_2)$ as a function of α under the type-I constant rates model (1.1). In the bifurcation diagrams shown in figures 1.3, and 1.5, our comparison is restricted to regions where x_2, y_2 and $z_2 > 0$ and $n_2 \in (n_1, 1)$. In those figures, EQ_2 values are constant with respect to k, and x_2 is constant for all α, k values by $x_2 = \frac{(1+m\theta+\nu)}{B}$. Parameter values used are: $r = 40$, $f = 0.75$, $m = 0.6$, $\theta = 9$, $\nu = 1$, $\mu = 19$, $C = 0$, $\beta = 25$, $\sigma = 0.9$.

A.4 Stability Criteria

A.4.1 Parameterizing for Model Comparison

The endemic disease equilibrium EQ_2 can only be determined analytically for the constant rates, type-I model (where $\alpha(n)$, $\beta(n)$, $\sigma(n)$ all constant) as detailed in Appendix A.3.

Generally, equilibrium matching is accomplished as follows. Consider a specific model (model 1) given by assuming functional forms $\beta_1(n)$, $\sigma_1(n)$ and $\alpha_1(n)$ with equilibrium point $EQ_* = (n_*, x_*, y_*, z_*)$. To parameterize model 2 defined by $\beta(n) = \beta_2(n)$, $\sigma(n) = \sigma_2(n)$ and $\alpha(n) = \alpha_2(n)$, these functions are parameterized so that $\beta_2(n_*) = \beta_1(n_*)$, $\sigma_2(n_*) = \sigma_1(n_*)$ and $\alpha_2(n_*) = \alpha_1(n_*)$ and so all other shared parameters are equal between models. This ensures EQ_* is now an equilibrium point of both models.

For our motivating example, the variable rates model assumes $\alpha(n) = \frac{a}{k+n}$, $\beta(n) = \frac{\beta_c}{k+n}$ and $\sigma(n) = \sigma_0(1 + \phi n)$. The constant rates model assumes $\alpha(n) = \frac{a}{k+n}$ with constant $\beta(n) = \beta$ and $\sigma(n) = \sigma$. Each model is matched at EQ_2 to the type I constant rates model (α, β and σ all constant). This requires setting $a = (k + n_2)\alpha$, $\beta_c = (k + n_2)\beta$ and $\sigma_0 = \frac{\sigma}{(1+\phi n_2)}$. To estimate plausible values of ϕ, we rely on the data in Figure 1.1. The best fit line to those data gives $\sigma(1)/\sigma(0) = (1 + \phi n) \approx 0.03/0.02$, a quantity independent of σ_0. To use this to estimate ϕ, we must first know what weight corresponds to the algal carrying capacity (i.e. what n corresponds to 1 mg C/L?). Assuming that 1 mg C/L corresponds to the carrying capacity $n = 1$ – a conservative (low) estimate – these data imply $\phi \approx 0.5$. If 1 mg C/L corresponds to some density below carrying capacity then

$\phi = 0.5/n > 0.5$. Thus, if carrying capacity corresponds to W mg C/L, then $\phi = W \cdot 0.5$. To avoid extrapolating beyond the available data, larger values of W may require a saturating or other functional form of $\sigma(n)$. In the text, we assume the conservative estimate of $\phi = 0.5$.

A.4.2 Stability Comparison of EQ_2: Reduced Model

For the reduced model (1.6) the constant and variable rates models are parameterized so they share the equilibrium point $EQ_2 = \left(n, x = \frac{V}{B}, y = x\frac{\alpha n-(1+m)}{V-\alpha nf}\right)$ (see Appendix A.3). At EQ_2 the Jacobian of the constant rates model with $\alpha(n) = \alpha$ is

$$Jac_0 = \begin{pmatrix} -nr & -\alpha n & -\alpha n \\ \alpha(x+fy) & \alpha n - (1+m) - By & \alpha nf - Bx \\ 0 & By & 0 \end{pmatrix} \tag{A.2}$$

The characteristic polynomial coefficients for this model at EQ_2 are

$$\begin{aligned} C_0 =& V(\alpha n - (1+m))\left(rn + \frac{\alpha^2 n(x+fy)}{(V-\alpha nf)}\right) \\ C_1 =& \alpha n\left((\alpha n - (1+m))\left(\frac{rnf}{V-\alpha nf} + \frac{V}{\alpha n}\right) + \alpha(x+fy)\right) \\ C_2 =& rn + \alpha nf\left(\frac{y}{x}\right) \end{aligned}$$

for $x = x_2$, $y = y_2 > 0$. If there exists additional consumer mortality resulting from disease (i.e. $n_2 > n_1 = \frac{1+m}{\alpha}$), it follows that whenever EQ_2 is biologically relevant (i.e. when $1 > n_2 > n_1$ and $x_2, y_2 > 0$) then $V - \alpha nf$, $V - (1+m)$, and $\alpha n - (1+m)$ are all positive, and so then are all coefficients $C_i > 0$.

Under the constant rates model with general $\alpha(n)$, the Jacobian at EQ_2 (Jac_c)

can be written in terms of Jac_0 above as

$$Jac_c = Jac_0 + \begin{pmatrix} -\alpha'(n)n(x+y) & 0 & 0 \\ \alpha'(n)n(x+fy) & 0 & 0 \\ 0 & 0 & 0 \end{pmatrix} \tag{A.4}$$

evaluated at EQ_2. Writing Jac_c this way, the coefficients of the corresponding characteristic polynomial ($c_0 + c_1\lambda + c_2\lambda^2 + \lambda^3$) can be written in terms of the coefficients C_i above and the elasticity of $\alpha(n)$ at EQ_2 ($E_{\alpha*}$) as $c_i = C_i + \gamma_i E_{\alpha*}$ where $\gamma_0 = \alpha By((V - \alpha nf)(x+y) + \alpha n(x+fy))$, $\gamma_1 = ((By - (\alpha n - M))(x+y)\alpha + \alpha n(x+fy))\alpha$, and $\gamma_2 = (x+y)\alpha$. Each γ_i is positive for biologically relevant EQ_2.

The Routh-Hurwitz stability criteria for EQ_2 under the constant rates model ($B(n) = B$) with general $\alpha(n)$ are given by

$$0 < c_0 \tag{A.5a}$$

$$0 < c_2 \tag{A.5b}$$

$$0 < c_1c_2 - c_0 \tag{A.5c}$$

where c_i are the characteristic polynomial coefficients of the Jacobian matrix at EQ_2, $p_c(\lambda) = c_0 + c_1\lambda + c_2\lambda^2 + \lambda^3$.

The Hopf bifurcation by which a stable EQ_2 gives rise to disease cycles LC_2 occurs when (A.5a,b) each hold, but condition (A.5c) fails, i.e. $c_1c_2 - c_0 = 0$ [Guckenheimer et al., 1997, Guckenheimer and Myers, 1996]. Assuming the case where EQ_2 is stable under the constant rates model (1.6) with general $\alpha(n)$, we may now describe how the variable rates $\beta(n)$ and $\sigma(n)$ affect the stability conditions of the endemic disease equilibrium EQ_2.

Under the variable rates model ($\beta(n)$ and $\sigma(n)$ non-constant), the Jacobian at

EQ_2 (Jac_v) can be written as

$$Jac_v = Jac_c + \begin{pmatrix} 0 & 0 & 0 \\ -\epsilon & 0 & 0 \\ \epsilon & 0 & 0 \end{pmatrix} \tag{A.6}$$

where $\epsilon = B'(n)xy$ evaluated at EQ_2.

Writing Jac_v in these terms yields the characteristic polynomial (A.7), where the coefficient $\gamma_B > 0$ for biologically relevant EQ_2 and E_B is the elasticity of $B(n)$ evaluated at EQ_2 (see Appendix A.4 for details).

$$p_v(\lambda) = (c_0 - \gamma_B E_B) + c_1\lambda + c_2\lambda^2 + \lambda^3 \tag{A.7}$$

Consequently, the inclusion of non-constant rates $\beta(n)$ and $\sigma(n)$ yields the EQ_2 stability criteria (A.8) with the Hopf bifurcation occurring at $c_1c_2 - c_0 + \gamma_B \cdot E_B = 0$.

$$0 < c_0 - \gamma_B \cdot E_B \tag{A.8a}$$

$$0 < c_2 \tag{A.8b}$$

$$0 < c_1c_2 - c_0 + \gamma_B \cdot E_B \tag{A.8c}$$

In the variable rates reduced model, $\gamma_B = \alpha Bxy(Bx - \alpha nf + \alpha n - M)$ (at EQ_2) is positive whenever EQ_2 is biologically relevant.

The stability difference between the variable rates and constant rates models with general $\alpha(n)$ can be considered in two contexts. Generally, (A.8a,c) can be written as $0 < c_0 - \gamma_B E_B < c_1c_2$, so a large enough positive or negative E_{B*} could result in a loss of stability. In the context of losing stability via a Hopf

bifurcation, (A.8c) shows that the direction which the Hopf bifurcation curve is shifted under the variable rates models can be determined by the sign of E_B.

A.4.3 Stability Comparison of EQ_2: General Model

For the constant rates model (1.1) with $\alpha(n) = \alpha$, $\rho = 1$ and $C(n) = 0$ the endemic equilibrium EQ_2 is as given in Appendix A.3. The characteristic polynomial coefficients for this model (written here in terms of the coefficients for the reduced model (1.6) with constant β, σ and α) are given by

$$\begin{aligned} D_0 &= \mu C_0 \\ D_1 &= \mu C_1 + \alpha(\beta z + V)\alpha n(x + fy) \\ D_2 &= \mu C_2 + rn\left(V + \alpha n f\left(\frac{y}{x}\right)\right) + \alpha^2 n(x + fy) \\ D_3 &= \mu + C_2 + V \end{aligned}$$

These are each positive whenever EQ_2 is biologically relevant.

In the constant rates model (1.1) with general $\alpha(n)$, the coefficients of the characteristic polynomial at EQ_2 ($p_c(\lambda) = d_0 + d_1\lambda + d_2\lambda^2 + d_3\lambda^3 + \lambda^4$) are given by $d_i = D_i + \kappa_i \cdot E_{\alpha*}$ where

$$\kappa_0 = \mu\alpha\beta z\,(V(x + y) + \alpha n x(1 - f)) \tag{A.10a}$$

$$\kappa_1 = \alpha^2 n\left(\mu\left((x + y)\frac{fy}{x} + (x + fy)\right) + (V + \beta z)(x + fy)\right) \tag{A.10b}$$

$$\kappa_2 = \alpha\left(\left(\mu + V + \alpha n\frac{fy}{x}\right)(x + y) + \alpha n\,(x + fy)\right) \tag{A.10c}$$

$$\kappa_3 = \alpha(x + y) \tag{A.10d}$$

These $\kappa_i > 0$ whenever $x_2, y_2 > 0$ and $n_2 \in (n_1, 1)$.

The Routh-Hurwitz stability conditions for EQ_2 under the constant rates model (1.1) with general $\alpha(n)$ are given by

$$0 < d_i, \text{ for } i = 0, 1, 3 \tag{A.11a}$$

$$0 < d_1 d_2 d_3 - (d_1^2 + d_3^2 d_0) \tag{A.11b}$$

Similar to the three dimensional case, the Hopf bifurcation giving rise to endemic disease cycles LC_2 is given by the failure of the last condition (A.11b) so long as (A.11a) each hold.

Under the variable rates model (1.1) with general $\alpha(n)$, the characteristic polynomial of the Jacobian at EQ_2 is given by

$$p_v(\lambda) = (d_0 - \mu\gamma\left(E_{\beta*} + E_{\sigma*}\right)) + (d_1 - \gamma E_{\beta*})\lambda + d_2\lambda^2 + d_3\lambda^3 + \lambda^4. \tag{A.12}$$

where $\gamma = (x_2 + y_2)(\alpha n_2 - (1 + m))V\alpha$. Whenever EQ_2 is biologically relevant ($n_1 < n_2 < 1$ and $x_2, y_2 > 0$) then $\gamma > 0$. The stability conditions are given by (A.13a-d).

$$0 < d_0 - \mu\gamma\left(E_{\beta*} + E_{\sigma*}\right) \tag{A.13a}$$

$$0 < d_1 - \gamma E_{\beta*} \tag{A.13b}$$

$$0 < d_3 \tag{A.13c}$$

$$\begin{aligned} 0 < {} & d_1 d_2 d_3 - (d_1^2 + d_3^2 d_0) + \\ & \mu(E_{\beta*} + E_{\sigma*})d_3^2\gamma - E_{\beta*}(\gamma E_{\beta*} + (d_2 d_3 - 2d_1))\gamma \end{aligned} \tag{A.13d}$$

Comparing the Hopf bifurcation criteria for the constant (A.13d) and variable rates model (A.11b), it follows that the effect of non-constant $\beta(n)$ and $\sigma(n)$ on the transition to cycling dynamics (i.e. the location of the Hopf bifurcation in parameter space) depends only on the sign of (1.9) as described in the text.

For very fast spore dynamics (e.g. μ relatively large), this result agrees with the results of the reduced model (1.6). The first term in (1.9) dominates so that an increasing $\sigma(n)$ has a stabilizing effect on the Hopf bifurcation, and a decreasing $\beta(n)$ has a destabilizing effect. More generally, (1.9) indicates that an increasing $\sigma(n)$ will always stabilize the transition to cycling dynamics (i.e. expand the region of parameter space where EQ_2 is stable by shifting the Hopf bifurcation), while a decreasing $\beta(n)$ can be either destabilizing or stabilizing depending on the sign of the second term in (1.9), which is quadratic in $E_{\beta*}$.

A.5 Other Possible Dynamics

The bifurcation diagrams in the text only present the biologically relevant dynamics that dominate those regions of parameter space. In some regions, additional bifurcations can occur. A complete bifurcation analysis of these models remains to be done, but computational results suggest the following.

In models (1.6) and (1.1) a type-II $\alpha(n)$ allows a second interior equilibrium point (EQ_3) to exist in the positive orthant (see Appendix A.3.2). EQ_3 is typically unstable, but can undergo a subcritical Hopf bifurcation (solid black curve, Fig. A.2) leaving it locally stable with a small basin of attraction. Under variable rates $\beta(n)$ and $\sigma(n)$, these bifurcations may occur at larger k values.

Models that include non-constant $\beta(n)$ and $\sigma(n)$ can also produce a period doubling bifurcation of LC_2 which has not yet been observed in the constant rates case. These nonlinearities may produce other dynamics impossible to observe under the constant rates model, however a more complete bifurcation analysis of these models is needed to verify such claims.

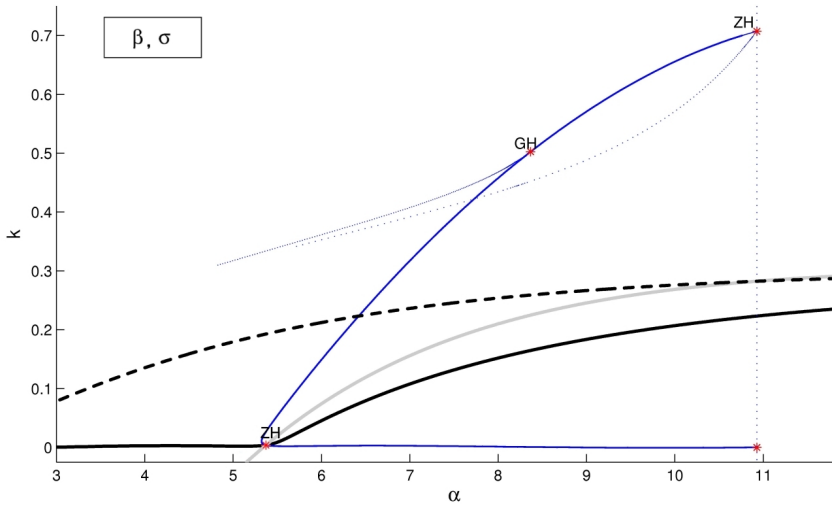

Figure A.2: A more complete bifurcation diagram for model (1.6) with $\alpha(n) = a/(k + n)$ and constant rates β and σ (cf. Figure 1.5A). The type-II $\alpha(n)$ allows models (1.6) and (1.1) to have a second equilibrium (EQ_3) in the positive orthant. As parameters move down across the dashed black curve, EQ_3 becomes positive valued as y_3 increases through 0. Computational results suggest it is locally *unstable* when it enters the positive orthant. As parameters cross down through the solid gray curve where $EQ_2 = EQ_3$, they cross through the solid black curve where EQ_3 undergoes a Hopf bifurcation. This appears to be a subcritical Hopf, giving rise to an unstable limit cycle leaving EQ_3 *locally stable* within a small basin of attraction. Most biologically plausible initial conditions reside outside of this small basin of attraction.

A.6 Consumer-Producer Models with Slow Disease Dynamics

We can clarify how disease affects consumer-producer dynamics by recognizing that disease will either reduce consumer fecundity, increase consumer mortality, or both. How does this affect the consumer-producer dynamics? How do those changes in turn affect the disease dynamics? How is bistability maintained between cycling and steady state dynamics in the presence of disease? To attempt answering these questions we next consider a limiting case of model (1.6) with constant $B(n) = B$.

Assuming $x + y > 0$, we can transform the direct transmission model (1.6) to be in terms of producers n, total consumers $p = x + y$ and the fraction of infected consumers $i = y/(x + y)$. This is done by substituting $f = 1 - g \in (0, 1)$, $x = ip$ and $y = (1 - i)p$ into $dp/dt = dx/dt + dy/dt$ and $di/dt = (dy/dt)/p - i(dp/dt)/p$. Defining $R = B/(1 + \nu)$, this yields

$$\frac{dn}{dt} = \left(\frac{r}{\alpha(n)}(1 - n) - p\right)\alpha(n)n \tag{A.14a}$$

$$\frac{dp}{dt} = \left(\alpha(n)n - \frac{1 + \nu i}{1 - gi}\right)(1 - gi)p \tag{A.14b}$$

$$\frac{di}{dt} = \left(Rp(1 - i) - 1 - \frac{d\ln(p)}{dt}\frac{1}{1 + \nu}\right)(1 + \nu)i. \tag{A.14c}$$

Here the equations are factored to clarify their nullclines and without loss of generality we have assumed no predation on consumers ($m = 0$). (Compare (A.14) to Hilker and Schmitz [2008] for a similar model with frequency dependent disease transmission and no bistability.)

Consider the case where the long-term disease dynamics (under A.14) occur slowly relative to the producer-consumer dynamics. In this case, the n-p dynamics will reach a quasi-asymptotic state (e.g. either steady state or cy-

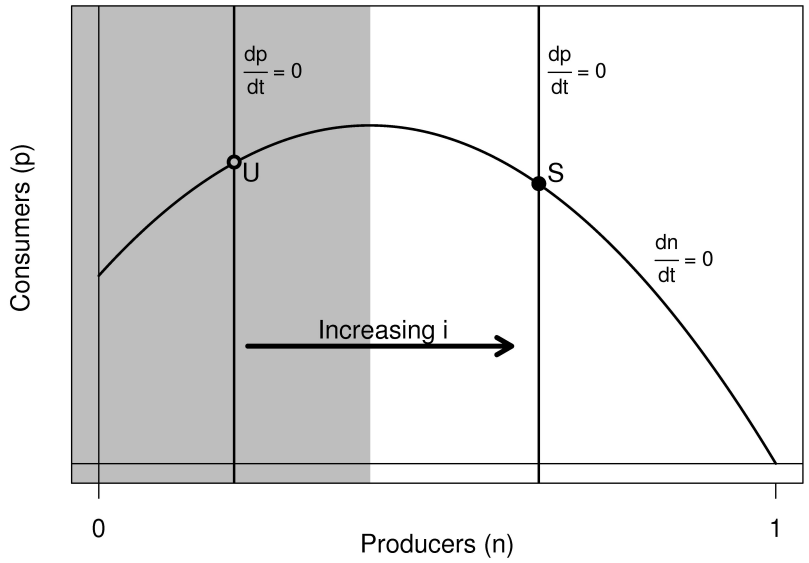

Figure A.3: Nullclines for the Rosenzweig-MacArthur model (type-II $\alpha(n)$) illustrating the consequence of reduced fecundity and/or increased mortality among consumers. Assuming a fixed fraction (i) of the population are diseased, increasing i shifts the p-nullcline to the right – the direction of increasing stability – while i has no effect on the n-nullcline. The coexistence equilibrium is unstable where the n-nullcline is increasing (shaded gray; here the populations cycle) and is stable where the n-nullcline is decreasing. This is generally the case for any monotone increasing feeding rate $\alpha(n)n$ under equations (A.14a,b).

cling dynamics) as i slowly changes. We can understand these quasi-asymptotic consumer-producer dynamics as follows.

Assuming constant $i \in (0, 1)$ the dynamics of (A.14a,b) can be understood from the n and p nullclines

$$\frac{1}{n}\frac{dn}{dt} = 0 \quad \Rightarrow \quad p = \frac{r}{\alpha(n)}(1-n) \tag{A.15a}$$

$$\frac{1}{p}\frac{dp}{dt} = 0 \quad \Rightarrow \quad G(i) = \alpha(n)n. \tag{A.15b}$$

where $G(i) = \frac{1+\nu i}{1-gi}$ is the fractional increase in the per-consumer mortality rate divided by the decrease in fecundity. For an example of these nullclines using a type-II functional response, see Figure A.3.

The p-nullcline (A.15b) for fixed i defines a vertical line at the equilibrium

value of $n = n_{eq}$. The coexistence equilibrium occurs where these two nullclines intersect in the positive quadrant of the n-p plane, and is stable when 1) the per-capita feeding rate $\alpha(n)n$ is increasing at n_{eq}, and 2) the n-nullcline (A.15a) is decreasing at n_{eq}. Cycling dynamics occur if the n-nullcline is increasing at n_{eq} (where the coexistence equilibrium is unstable).

As i only affects the p-nullcline, the consequences of reduced fecundity and increased mortality depend entirely on how i affects the equilibrium value of n. Differentiating $\alpha(n)n = G(i)$ with respect to i, it follows that n_* typically *increases* as disease prevalence i increases since

$$\operatorname{sign}\left(\frac{dn_*}{di}\right) = \operatorname{sign}\left(\frac{d}{dn}(A(n_*)n_*)\right)\operatorname{sign}\left(\frac{d}{di}G(i)\right). \tag{A.16}$$

Consequently, a slow increase in disease prevalence among the consumer population should stabilize the system by increasing n_{eq} as shown in Figure A.3.

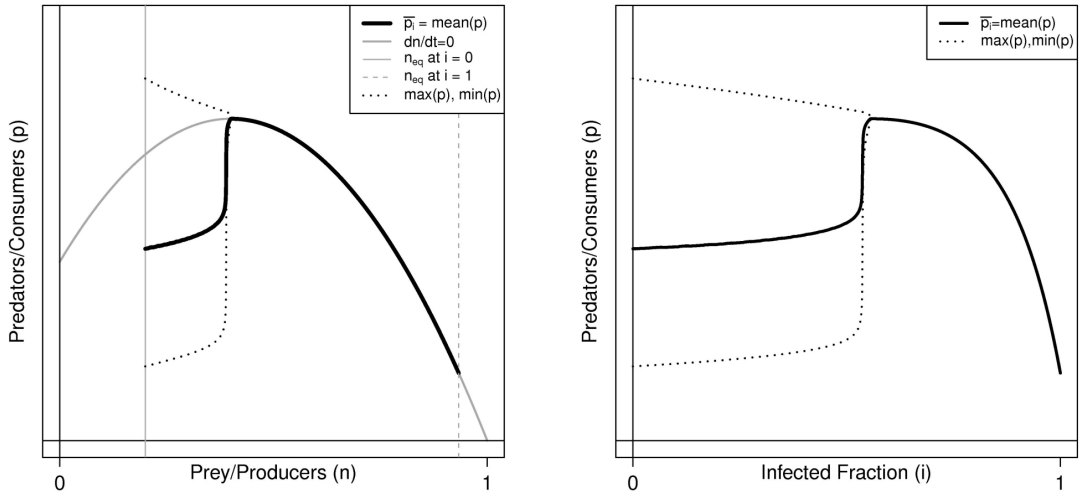

Figure A.4: Nullclines for the Rosenzweig-MacArthur model (type-II $\alpha(n)$) illustrating how the "hydra effect" [Abrams, 2009] in this model allows disease to paradoxically increase the mean producer population size during cycling dynamics. The mean and amplitude of the consumer population is shown as the p-nullcline (vertical line) moves right as the fixed disease fraction (i) is increased from $i = 0$ to $i = 1$. Also shown is the mean $\overline{p_i}$ as a function of i. See Figure A.3 for other details.

A.6.1 Why bistability?

Having described the consumer-producer dynamics under fixed i, we can clarify how density-dependent disease transmission leads to bistability by simplifying the disease equation (A.14c). This can be done (albeit crudely) by considering the criterion for disease to invade the disease-free cycle LC_1 (see Appendix A.6.2)

$$R\overline{p_0} > 1. \tag{A.17}$$

Here $\overline{p_0}$ is the mean consumer density over the disease-free cycle. Note the similarity to the condition $R_{0d} > 1$ necessary for invasion of the disease-free steady state EQ_1.

Based upon this observation we approximate equation (A.14c) by taking the "slow disease" limit of (A.14) which relies on the mean producer density $\overline{p_i}$ over

the attracting cycle or equilibrium point determined by (A.14a,b) with fixed i. Doing so yields the approximation

$$\frac{di}{dt} = i\,(\overline{p_i} \cdot (1 - i) - 1/R)\,R \tag{A.18}$$

Computing $\overline{p_i}$ over a range of (fixed) i values, Figure A.4 shows how a disease-induced mortality and reduced fecundity can each *increase* mean consumer density during cycling regimes, when consumer-producer dynamics are fast relative to changes in i. This "hydra effect" [Abrams, 2009] appears to be what allows for bistability when disease transmission is density dependent. Positive feedback between p and i means that perturbing either a cycling system with little or no disease could sufficiently increase consumer density and push the system above threshold, allowing persistence of disease at steady state.

More precesely, Figure A.5 shows the $\overline{p_i}$ curve shown in Figure A.4 shapes the dynamics of A.18 for differing values of R. Stability is determined by where i is increasing ($\overline{p_i}(1-i) > 1/R$) and decreasing ($\overline{p_i}(1-i) < 1/R$), and the small peak in Figure A.5 is approximately where the Hopf bifurcation occurs in the consumer-resource model (A.14a,b). As in Figure A.4, equilibria to the left of this peak correspond to cycles under model (A.14a,c) and those to the right correspond to the endemic disease steady state EQ_2.

Figure A.5 accounts for four of the five qualitatively different cases described for models (1.1) and (1.6) in the text. Though not shown, if the "Hopf peak" were to surpass the critical value of $\overline{p_0}$ (the triangle in Figure A.5), then any values of $1/R$ between the peak's maximum value and $\overline{p_0}$ would yield bistability between disease-free cycles LC_1 and the endemic disease steady state EQ_2 as in region ④ of Figure 1.3.

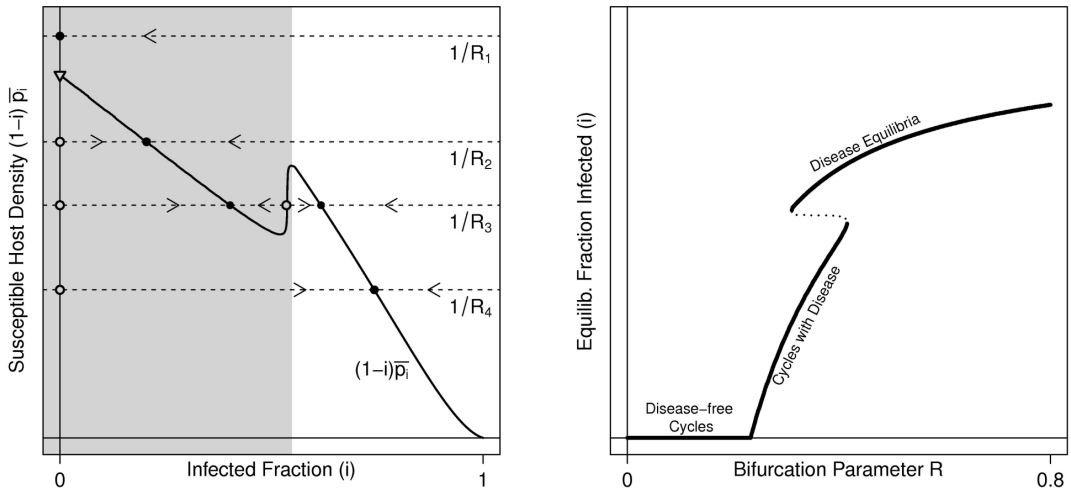

Figure A.5: Example dynamics of equation (A.18) for multiple values of parameter R. Equilibria in the region shaded light gray correspond to cycles under (A.14). Note $i > 0$ requires $R\overline{p_0} < 1$ (triangle at $i = 0$). In terms of the dynamics of models (A.14) and (1.6), these equilibria correspond to dynamic states where only the disease-free cycle LC_1 is stable (R_1), only the disease cycle LC_2 is stable (R_2), both LC_2 and the endemic disease steady state EQ_2 are bistable (R_3), and where only EQ_2 is stable (R_4). These correspond to the dynamics dominating regions ⑤, ②, ③, and ① in Figure 1.3, respectively.

In summary, the non-equilibrium dynamics of models (1.6) and (1.1) are heavily influenced by the fact that disease transmission is density dependent and that disease can increase the mean consumer population size during consumer-resource cycling. Positive feedback between disease prevalence i and the mean producer density $\overline{p}$ during cycling allows for both disease-induced stabilization of consumer-resource cycles and potential bistability between the endemic disease equilibrium and cycling dynamics with or without disease.

A.6.2 Criteria for Invasion of Disease-free Limit Cycles

Equation (A.14c) is equivalent to

$$\frac{d(\ln i)}{dt} = (1 + v)(Rp(1 - i) - 1) - \frac{d(\ln p)}{dt}. \tag{A.19}$$

A criterion for the local stability of the disease-free limit cycle LC_1 (period T) can be obtained by considering the average rate of increase in i over that disease-free limit cycle assuming an arbitrarily small $i(0) > 0$. Define the instantaneous growth rate on LC_1 as

$$\lambda_i(t) \equiv (1+\nu)(Rp(1-i)-1) - \frac{d(\ln p)}{dt}. \tag{A.20}$$

The average growth rate over LC_1 is therefore given by

$$\Lambda_T \equiv \frac{1}{T}\int_0^T \lambda_i(t)dt. \tag{A.21}$$

thus LC_1 is locally stable if $\Lambda_T < 0$ and disease invades if $\Lambda_T > 0$.

Combining the above equations yields

$$\begin{aligned}\Lambda_T =& \frac{1}{T}\int_0^T (1+\nu)(Rp(1-i)dt - \frac{1}{T}\int_0^T \frac{d(\ln p)}{dt}dt \\ =& (R\overline{s}-1)(1+\nu) - \frac{1}{T}(\ln p(T) - \ln p(0))\end{aligned} \tag{A.22}$$

where $\overline{s} \equiv \frac{1}{T}\int_0^T p(t)(1-i(t))dt$. On the limit cycle $p(T) = p(0)$ and $\overline{s} = \overline{s_0}$ where s_0 is the mean susceptible population size over the disease-free cycle. These two facts together with (A.22) yield the LC_1 stability criterion

$$R\overline{s_0} < 1. \tag{A.23}$$

Note that in cases of bistability, sufficiently high initial levels of disease can push the system beyond the basin of attraction for disease-free cycle LC_1 and result in disease invasion despite $R\overline{s_0} < 1$.

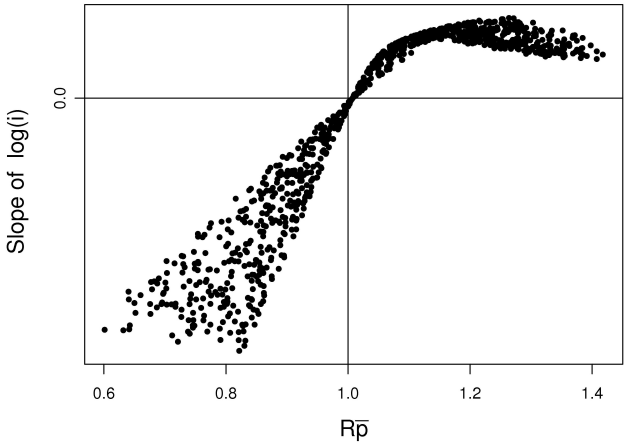

Figure A.6: Simulation showing the performance of the disease invasion criterion for the disease-free cycle LC_1 under constant rates model (1.1) with fast spore dynamics. Parameter values were sampled from uniform distributions with $\beta \in (5, 11)$, $f \in (0, 1)$ and $\nu \in (0, 3)$. Disease invasion shown by the slope of the best fit line to $\log(i(t))$ over 15 time units, with positive slope indicating disease invasion. The quantity $R\overline{p}$ is as described in the text. Parameters used: $r = 40$, $\alpha = 9$, $k = 0.6$, $m = 0$, $\mu = 1900$, $\sigma = 90$.

APPENDIX B

APPENDIX OF CHAPTER 2

B.1 Scaling the model

The unscaled model is based on the non-specific immune response model described in Reynolds et al. [2006], here extended to include the specific immune response. It is given by

$$\frac{dP}{dt} = k_{pg}P\left(1 - \frac{P}{p_\infty}\right) - \frac{k_{pm}s_mP}{\mu_m + k_{mp}P} - \left(k_{pn0} + \frac{(k_{pnmax} - k_{pn0})Y^\theta}{x_{ny}^\theta + Y^\theta}\right)cNP \tag{B.1a}$$

$$\frac{dN}{dt} = \frac{s_{nr}c\left(k_{nn}N + k_{np}P\right)}{\mu_{nr} + c\left(k_{nn}N + k_{np}P\right)} - \mu_nN \tag{B.1b}$$

$$\frac{dY_0}{dt} = \frac{k_{ynp}(cNP)^\alpha}{x_{np}^\alpha + (cNP)^\alpha} - \mu_{y0}Y_0 \tag{B.1c}$$

$$\frac{dY}{dt} = \mu_{y0}Y_0 - \mu_yY \tag{B.1d}$$

Model (2.1) in the text is obtained by making the following transformation: $p = P/p_\infty$, $n = N/s_{nr}$, $y_0 = Y_0/k_{ynp}$, $y = Y/k_{ynp}$, $k_{pg} = k_{pg}$, $k_m = k_{pm}s_m/(k_{mp}p_{inf})$, $\mu_p = \mu_m/(k_{mp}p_{inf})$, $K_{min} = cs_{nr}k_{ny0}$, $K_{max} = cs_{nr}k_{np_{max}}$, $\theta = \theta$, $x = x_{ny}/k_{ynp}$, $x_y = x_{np}/(cs_{nr}p_{inf})$, $k_p = k_{np}p_{inf}/(k_{nn}s_{nr})$, $x_n = \mu_{nr}/(ck_{nn}s_{nr})$, $\mu_n = \mu_n$, $\alpha = \alpha$, $\mu_{y0} = \mu_{y0}$, $\mu_y = \mu_y$ and time $t = t$.

B.1.1 Changes from the Reynolds et al 2006 model

1. The constant k_{pn} is replaced by the function $K_{pn}(Y_a)$. According to Blanchard and Browning [2005, p.490] in some species of mycoplasma anti-

Parameter	Value	Range	Description
k_{pg}	0.10	0.01 – 2.44	Pathogen growth rate (Mycoplasmas relatively slow)
p_{inf}	2x10^7	-	Rescaled pathogen density
k_{pm}	0.6	-	Maximum removal by local innate components
s_m	0.005	-	
k_{mp}	0.01	-	Maximum removal by local innate components
μ_m	0.002	0.0013 – 0.0048	
k_{pn0}	0	$k_{pn0} < k_{pnmax}$	Basline active innate pathogen removal rate
$k_{pn_{max}}$	1.8	0 – 2.5	Maximum removal rate, specific components present
x_{ny}	1	-	Half-saturation constant for activation of specific response
c	0.75	-	Anti-inflammatory mediator effect (held constant)
s_{nr}	0.08	-	
k_{np}	0.1	-	Pathogen activation of the innate response
k_{nn}	0.01	-	Positive feedback in the activation of the innate response
μ_{nr}	0.12	0.069 – 0.12	
μ_n	0.05	$\mu_n < \mu_{nr}$	
k_{ynp}	0.005	-	Rescaled maturing specific immune components
α	6	-	
θ	6	-	
x_{np}	10	-	Specific comp. half-saturation constant for pathogen removal
μ_{y0}	0.0037	-	Activation rate of specific components
μ_y	0.0016	-	Decay rate of specific components
k_{dn}	0.06	-	Maximum rate of damage/inflammation accumulation (sets $D_{max} = 3$)
x_{dn}	0.06	-	Half-saturation constant of innate activity causing damage
μ_D	0.02	-	Rate of healing of damage from damage/inflammation

Table B.1: Parameter values of the unscaled model, as modified from Reynolds et al 2005.

bodies are necessary for phagocytosis by innate immune components (e.g. macrophages) so we assume the efficiency of pathogen removal k_{pn} is instead a function of specific immune activity Y and is relatively low without

assistance from the specific immune system (at low Y).

2. The anti-inflammatory mediators C_A modeled in Reynolds et al. [2006] et al are here assumed to be constant, and have been combined with parameter c_∞ into the single parameter $c = \frac{1}{1+\left(\frac{C_a}{c_\infty}\right)^2}$.

3. To model maturing and active specific immune components (e.g. B- or T-cells, antibodies, etc.) two new state variables were introduced: Y_0 and Y, respectively. Assuming activation and maturation occur in response to antigen presentation by macrophages the activation rate of the maturing components Y_0 is assumed to be an increasing function of both P and N, with the presence of pathogen and an activated specific immune response required for activation.

   Other possibilities for the first term in equation (2.1c) include (1) to assume that antigen presentation is more directly related to N levels and that it saturates at low antigen levels (low P), e.g. $\frac{k_{ynp}P^\alpha}{x_{np}^\alpha+P^\alpha}N$; or (2) to assume that it depends on the amount of antigen processed by N, i.e. that the activation rate is proportional to the net rate of pathogen loss $K(Y)NP$.

4. Setting $k_{nd} = 0$ decouples the feedback of damage D to activate innate components (N) by assuming it is negligible w.r.t. the pathogen and self-activation. This removes D from the system simplifying the model mathematically, and it is biologically reasonable as typically *M. gallisepticum* doesn't seem to lead to self-sustained inflammation.

B.2 Simplifying Model (2.1)

The simplified models in the text were derived based on the existence of multiple timescales in the full model and the role certain terms played in driving the dynamics under specific circumstances as explained in the text. Additional details regarding these simplified models are as follows.

1. We assume the p-n subsystem is fast relative to the y_0-y dynamics, and that the n dynamics are fast relative to the p dynamics. In the limit where n tracks p instantaneously, n will approximately satisfy $\frac{dn}{dt} = 0$. Solving for n as a function of p, $n(p)$ is one of the two non-zero roots of dn/dt,

$$n_{\pm}(p) = \frac{1}{2}\left(\frac{1}{\mu_n} - x_n - k_p p\right) \pm \frac{1}{2}\sqrt{\left(\frac{1}{\mu_n} - x_n - k_p p\right)^2 + 4\frac{1}{\mu_n}k_p p}. \tag{B.2}$$

   Requiring $n(p) > 0$ when $p > 0$ and that $n(0) = 0$ implies that we only need consider the case where $n(p) = n_+(p)$, and define

$$n(p) = \frac{1}{2}\left(\frac{1}{\mu_n} - x_n - k_p p\right) + \frac{1}{2}\sqrt{\left(\frac{1}{\mu_n} - x_n - k_p p\right)^2 + 4\frac{1}{\mu_n}k_p p}. \tag{B.3}$$

2. Further simplifications can be made by assuming more direct activation of the adaptive/specific immune response (in the context of mean-field equations, this essentially assumes an exponentially distributed time to activation instead of a gamma distributed delay). This model has a single adaptive immune response variable y replacing equations (B.1c) and (B.1d) with the single equation

$$\frac{dy}{dt} = \frac{(np)^\alpha}{x_y^\alpha + (np)^\alpha} - \mu_y y.$$

This system has the same equilibrium conditions as (2.1), but may yield different stability conditions.

3. For parameter values near those given in Table B.1, additional simplifications can be made by dropping certain terms from equation (2.1) since the model terms are approximately

$$\frac{dp}{dt} = 0.1p(1-p) - \frac{1.5 \cdot 10^{-8} p}{1 \cdot 10^{-8} + p} - \left(\frac{0.1086 y^6}{200^6 + y^6}\right) np \tag{B.4a}$$

$$\frac{dn}{dt} = \frac{n + 2.5 \cdot 10^9 p}{199 + n + 2.5 \cdot 10^9 p} - 0.05n \tag{B.4b}$$

$$\frac{dy_0}{dt} = \frac{(np)^6}{8.29 \cdot 10^{-36} + (np)^6} - 0.0037 y_0 \tag{B.4c}$$

$$\frac{dy}{dt} = 0.0037 y_0 - 0.0016 y \tag{B.4d}$$

and

$$n(p) = \frac{1}{2}\left(-179 - 2.5 \cdot 10^9 p\right) + \frac{1}{2}\sqrt{(-179 - 2.5 \cdot 10^9 p)^2 + 2 \cdot 10^{11} p}. \tag{B.5}$$

This suggests the following simplifications. The activation of the innate response is primarily driven by pathogen load p, as $k_p \gg 1$. Omitting n from the $\frac{dn}{dt}$ equation leaves

$$\frac{dn}{dt} = \frac{p}{\frac{x_n}{k_p} + p} - \mu_n n \tag{B.6}$$

reducing $n(p)$ to

$$n(p) = \frac{1}{\mu_n} \frac{p}{\frac{x_n}{k_p} + p}. \tag{B.7}$$

Combining the above simplifications yields the simplified p-y model (2.8) which approximates the slow time scale dynamics of model 2.1.

B.3 Fast (*p*-*n* model) dynamics

Because different processes in model (2.1) occur over a broad range of time scales, we can analyze the model dynamics using standard separation of time scales techniques. We first consider the dynamics without an active immune response, then consider the "fast" time scale dynamics given by the *p*-*n* model. Results similar to those in B.3.1 and B.3.2 were previously discussed by Reynolds et al. [2006] for a very similar model.

B.3.1 Pathogen dynamics without an immune response

Holding the specific and non-specific immune response constant ($n = 0$), the pathogen dynamics follow

$$\frac{dp}{dt} = k_{pg} p\,(1-p) - \frac{k_m p}{\mu_p + p} \tag{B.8}$$

where the second term captures the host's baseline immune defenses as detailed in the text.

Equation (B.8) can have one to three equilibria

$$p_o = 0 \tag{B.9a}$$

$$p_{crit} = \frac{1}{2}\left(\left(1-\mu_p\right) - \sqrt{\left(1+\mu_p\right)^2 - \frac{4}{k_{pg}}k_m}\right) \tag{B.9b}$$

$$p_{max} = \frac{1}{2}\left(\left(1-\mu_p\right) + \sqrt{\left(1+\mu_p\right)^2 - \frac{4}{k_{pg}}k_m}\right) \tag{B.9c}$$

corresponding, respectively, to a state of health (stable when $r_0 < 0$; see text), an unstable equilibrium and threshold for the Allee effect (unstable when p_{crit}

positive; same as $r_0 < 0$) and an equilibrium state of pathogen persistence (stable when p_s exists in $(0, 1]$).

B.3.2 Dynamics of the *p*-*n* subsystem

Next we consider the dynamics of the "fast" model (2.4), where the ("slow" time scale) specific immune dynamics are treated as constant. The equilibria for equations (2.4) are

$$(p_o, n_o) = (0, 0) \tag{B.10a}$$

$$(p_n, n_n) = \left(0, \frac{1}{\mu_n} - x_n\right) \tag{B.10b}$$

$$(p_*, n_*), \quad p_*,\ n_* > 0 \tag{B.10c}$$

which correspond to a state of health (B.10a, the origin), a self-sustaining immune response that can persist in the absence of pathogen (B.10b) and one or more equilibria with positive pathogen density (p_*) and immune activity (n_*). Typically there are only one (e.g. $k_m = 0$) or two (see figure 2.4) interior equilibria. In rare cases, there can be three interior equilibria, two of which arise at relatively low pathogen densities via a saddle-node bifurcation, resulting in bistability. Ranking the three equilibria by pathogen density, the middle equilibrium acts like an Allee threshold (an unstable equilibrium) resulting in bistability between the upper steady state and a lower steady state (or limit cycle) instead of bistability with the origin.

Stability criteria for these equilibria are as follows. The healthy state (B.10a) is locally stable when $r_0 < 0$ and when the host immune response is not self-sustaining $n_n < 0$, where r_0 and n_n are given by (2.3) and (B.10b) respectively. The

state of pathogen-free persistent inflammation (B.10b) is caused by the positive feedback in the non-specific immune response (n), and is locally stable whenever $n_n > 0$ and pathogen cannot invade that state $r_0 < K_{ny} n_n$.

Stability criteria for interior equilibria (B.10c) and criteria for an Allee effect are best summarized by considering the nullclines of model (2.4) given by $\frac{dp}{dt} = 0$ and $\frac{dn}{dt} = 0$. The p- and n-nullclines are, respectively

$$n(p) = \frac{\left(k_{pg}(1-p) - \frac{k_m}{\mu_p + p}\right)}{K_{ny}}; \; p = 0 \tag{B.11a}$$

$$p(n) = \frac{n}{k_p}\left(\frac{x_n}{\frac{1}{\mu_n} - n} - 1\right). \tag{B.11b}$$

It clarifies things to think of the p and n nullclines restricted to the positive quadrant of the p-n plane with p on the horizontal axis and n on the vertical axis, as shown in Figure 2.4. We can rewrite the nullclines (B.11) as functions of p when restricted to the positive quadrant.

$$f_p(p) = \frac{\left(k_{pg}(1-p) - \frac{k_m}{\mu_p + p}\right)}{K_{ny}}; \; p = 0 \tag{B.12a}$$

$$f_n(p) = \frac{1}{2}\left(\left(n_n - k_p p\right) + \sqrt{\left(n_n - k_p p\right)^2 + \frac{4k_p}{\mu_n} p}\right) \tag{B.12b}$$

The simpler of the two ($f_n(p)$, the n-nullcline) is described first. This curve is concave down and either increases from the origin or ($p = 0$, $n = n_n$) towards $n \to \mu_n$ with increasing p (see solid curve in figure 2.4).

If $k_m = 0$ the p-nullcline is simply a decreasing line intersecting the axes at ($p = 0$, $n = k_{pg}/K_{ny}$) and ($p = 1$, $n = 0$). If $k_m > 0$, the second term in (B.11a) introduces a vertical asymptote at $p = -\mu_p$. This makes the p-nullcline concave down and it intersects the p-axis twice: it increases through the p-axis somewhere above $p = -\mu_p$ and decreases across the p-axis between $1 - \mu_p$ and 1.

These two roots are given by

$$p_{\pm} = \frac{1}{2}\left(\left(1-\mu_p\right) \pm \sqrt{\left(1+\mu_p\right)^2 - \frac{4}{k_{pg}}k_m}\right) \tag{B.13}$$

The lower root is positive only if $\frac{k_m}{\mu_p} > k_{pg}$ (i.e. when equation (2.2) shows bistability). When (B.11a) is unimodal over the domain $(0,1)$, the peak occurs at $p = \sqrt{\frac{k_m}{k_{pg}}} - \mu_p$.

Having described these two nullclines in detail, we may now consider the stability criteria of interior equilibrium points.

Stability of Interior Equilibria of (2.4)

On the positive quadrant of the *p*-*n* plane under model (2.4), denote the *p*-nullcline by $f_p(p)$ and the *n*-nullcline by $f_n(p)$ according to equations (B.12). Assume these curves intersect to yield an equilibrium point (p_*, n_*). Stability of this equilibrium is determined by the sign of the Jacobian's trace and determinant at this point, where

$$\text{sign}(-Tr) = \text{sign}\left(-pK_{ny}f_p'(p) + \frac{d}{dp}\left[\frac{dn}{dt}\right]\frac{1}{f_n'(p)}\right)_{(p,n)=(p_*,n_*)} \tag{B.14a}$$

$$\text{sign}(Det) = \text{sign}(f_n'(p) - f_p'(p))_{(p,n)=(p_*,n_*)} \tag{B.14b}$$

The stability conditions for (p_*, n_*) can be summarized as

$$f_p'(p) < \min\left(f_n'(p),\ \frac{d}{dp}\left[\frac{dn}{dt}\right]\frac{1}{pK_{ny}f_n'(p)}\right)_{(p,n)=(p_*,n_*)} \tag{B.15}$$

where loss of stability via a Hopf bifurcation results in

$$\frac{\left(\frac{d}{dp}\left[\frac{dn}{dt}\right]\right)_{(p_*,n_*)}}{p_*K_{ny}f_n'(p_*)} < f_p'(p_*) < f_n'(p_*) \tag{B.16}$$

Limited numerical investigation suggests cycling dynamics in the fast p-n subsystem are rare and of small amplitude for biologically relevant parameter values.

These criteria have the following implications.

1. Here, both $f_n'(p) > 0$ and $\frac{d}{dp}\left(\frac{dn}{dt}\right) > 0$ hold. This implies that Hopf bifurcations require both nullclines be increasing functions of p.
2. If the p-nullcline is a strictly decreasing function on all of $p \in (0, 1)$ – e.g. if $k_m \approx 0$ – there can be no stable limit cycle oscillations. Therefore in this case a necessary (but not sufficient) requirement for cycling is that (i.e., $k_m \geq k_{pg}\mu_p^2$).

B.3.3 Simplified p-n model dynamics

In the text we simplify the p-n model (2.4) by omitting positive feedback in the activation rate of n. This yields the new form of dn/dt given by (2.5). Here we detail the dynamics of this simplified p-n model.

First, we rewrite the model equations in terms of their nullclines

$$\frac{dp}{dt} = (f_p(p) - n)K_{ny}p \tag{B.17a}$$

$$\frac{dn}{dt} = (f_n(p) - n)\mu_n \tag{B.17b}$$

where the p-nullcline (for $p > 0$) is $f_p(p)$ (B.12a) and the n-nullcline is $f_n(p) \equiv \mathbf{n}(p)$ (2.6).

The stability of the origin under this model is as stated in the text, with $r_0 > 0$ required for pathogen invasion. Linearizing this system about any equilibrium

with $p_* > 0$, $n_* > 0$ yields a Jacobian matrix with trace and determinant

$$-Tr = -p_* K_{ny} f_p'(p_*) + \mu_n \tag{B.18a}$$

$$Det = \mu_n K_{ny} p_* (f_n'(p_*) - f_p'(p_*)). \tag{B.18b}$$

This equilibrium is stable when these two quantities are positive with loss of stability via a Hopf bifurcation when Tr increases through 0.

B.3.4 Pathogen dynamics with fast n

Assuming a fast non-specific response (n) under the simplified p-n model given by (2.4a) and (2.5), we can approximate that subsystem with the single equation (2.7). Relative to the simplified p-n model, the dynamics of (2.7) can be summarized as follows (see Figure B.1).

The equilibria of the simplified p-n model satisfy $\frac{dp}{dt} = 0$ and $\frac{dn}{dt} = 0$, and therefore those equilibrium pathogen densities are exactly the equilibria of the one dimensional model (2.7). Writing equation (2.7) using the p and n nullclines in the previous section

$$\frac{dp}{dt} = (f_p(p) - f_n(p)) K_{ny} p. \tag{B.19}$$

Linearizing about an equilibrium point $p_* > 0$ gives the stability condition

$$f_n'(p_*) - f_p'(p_*) > 0. \tag{B.20}$$

Recalling stability conditions (B.18), it follows that if $p_*, n_* > 0$ is stable under the simplified p-n model then p_* is necessarily a stable equilibrium of the one dimensional model (2.7). Likewise, unstable equilibria associated with stable limit cycles will be stable under model (2.7) so long as (B.18b) remains positive.

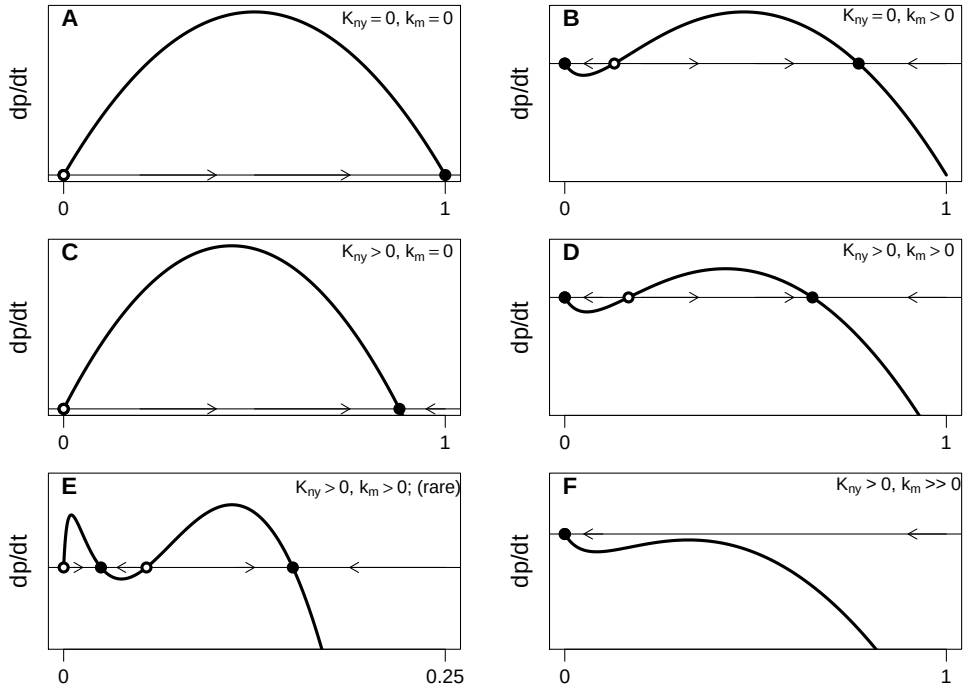

Figure B.1: Dynamics of (2.7) which approximate the simplified *p*-*n* subsystem when *n*-dynamics are fast.

B.4 Slow *p*-*y* model dynamics

We here rewrite the *p*-*y* model equations (2.8) in a more general form

$$\frac{dp}{dt} = \left(k_{pg}(1-p) - \frac{k_m}{\mu_p + p} - K(y)\mathbf{n}(p)\right)p \tag{B.21a}$$

$$\frac{dy}{dt} = G(p) - \mu_y y. \tag{B.21b}$$

where $G(p)$ is the specific immune activation rate, $G(p) = (\mathbf{n}(p)p)^\alpha/((\mathbf{n}(p)p)^\alpha + x_y^\alpha)$. More generally the results below hold for other choices of G where $G(0) = G'(0) = 0$, $G'(p) \geq 0$ and $G(p) \leq G_{max}$.

The equilibria of the *p*-*y* model (2.8) are only the origin (the healthy state) and the intersections of the nullclines (2.10) in the interior of the positive quadrant, since $\mathbf{n}(0) = 0$ (i.e. there is no self-sustaining inflammatory response). Stability

conditions for these equilibria are as follows.

The origin has eigenvalues $\lambda_1 = r_0$ and $\lambda_2 = -\mu_y$, where r_0 is given by (2.3) and hence local stability is determined by whether r_0 is greater or less than 0.

Stability of the interior equilibria can be considered first under the simple case where $k_m = 0$. An interior equilibrium point is stable when the Jacobian's determinant is positive and its trace negative. For model (B.21),

$$-Tr(J) = \mu_y + \left(k_{pg} + K(y)\mathbf{n}'(p)\right)p \tag{B.22a}$$

$$Det(J) = \left(\left(k_{pg} + K(y)\mathbf{n}'(p)\right)\mu_y + K'(y)\mathbf{n}(p)G'(p)\right)p. \tag{B.22b}$$

Recalling that $\mathbf{n}(p)$, $K(y)$ and $G(p)$ are each increasing functions, stability is ensured as both of the quantities above are positive for any equilibrium quantities $p, y > 0$.

More generally, if $k_m > 0$ then

$$-Tr(J) = \mu_y + \left(k_{pg} + K(y)\mathbf{n}'(p) - \frac{k_m}{(\mu_p + p)^2}\right)p \tag{B.23a}$$

$$Det(J) = \left(\left(k_{pg} + K(y)\mathbf{n}'(p) - \frac{k_m}{(\mu_p + p)^2}\right)\mu_y + K'(y)\mathbf{n}(p)G'(p)\right)p \tag{B.23b}$$

Here stability can be lost if either of these two quantities becomes negative. The loss of stability via a Hopf bifurcation occurs when (B.23a) passes through 0. Computational results suggest cycling dynamics only occur rarely and with small amplitudes for parameter values relevant to this particular biological application. They occur during instances of bi- or multi-stability and typically have small basins of attraction. That said, they may have some relevance to the loss of low-level pathogen persistence via stochastic extinction.

B.4.1 Nullclines of the *p*-*y* model

The nullclines of the *p*-*y* model (B.21a,b) for positive values p and y are

$$g_p(p) = K^{-1}\left(\frac{k_{pg}(1-p) - \frac{k_m}{\mu_p + p}}{\mathbf{n}(p)}\right) \tag{B.24a}$$

$$g_y(p) = \frac{G(p)}{\mu_y} \tag{B.24b}$$

For the case of $G(p)$ considered in the text, the y-nullcline (2.10b) is a strictly increasing function of p, increasing from the origin and asymptotically approaching the saturating value $y = \mu_y^{-1}$. The y-nullcline reaches half that maximum value when $p = p_{1/2}$ defined by $\mathbf{n}(p_{1/2})p_{1/2} = x_y$ (see 2.10b) and given explicitly by

$$p_{1/2} = x_y\mu_n\left(\frac{1 + \sqrt{1 + 4\frac{x_n/k_p}{x_y\mu_n}}}{2}\right) \tag{B.25}$$

Recall from the full model (2.1) that the activation rates of the innate (n) and specific (y_0) immune responses (see the first terms in (2.1)b,c) reach half of their maximum value when $p = x_n/k_p$ and $p = x_y$, respectively. If the innate response reaches a maximum activity level at relatively small p (i.e. $k_p/x_n \gg 1$), then $\mathbf{n}(p)$ is approximately its upper limit of $1/\mu_p$ for most $p \in (0, 1)$. If $x_n/k_p \ll x_y\mu_n$, then $p_{1/2} \approx x_y\mu_n$. If $x_n/k_p \gg x_y\mu_n$ then $p_{1/2} \approx \sqrt{x_y\mu_p x_n/k_p}$.

Letting $F(p) = (k_{pg}(1-p) - \frac{k_m}{\mu_p + p})/\mathbf{n}(p)$, the slope of the nullclines (B.24) at an equilibrium point (p_*, y_*) are, respectively

$$g_p'(p_*) = K^{-1\prime}(F(p_*))\,F'(p_*) \tag{B.26a}$$

$$g_y'(p_*) = \frac{G'(p_*)}{\mu_y} \tag{B.26b}$$

where the signs of $K^{-1\prime}(\cdot)$ and $G'(\cdot)$ are positive and the sign of $F'(\cdot)$ may be

positive or negative, since at any positive valued equilibrium point (p,y)

$$F'(p) = -\left(k_{pg} + K(y)\mathbf{n}'(p) - \frac{k_m}{(\mu_p + p)^2}\right)\frac{1}{\mathbf{n}(p)}.$$

To relate the slope of the nullclines to the stability criteria (B.23), a little calculus gives that $K^{-1'}(F(p_*)) = 1/K'(y_*)$ and hence $g'_p(p_*) = F'(p_*)/K'(y_*)$. Together with (B.26) this yields the general ($k_m \geq 0$) stability criteria

$$-Tr(J) = \mu_y - g'_p(p_*)K'(y_*)\mathbf{n}(p_*)p_* \tag{B.27a}$$

$$Det(J) = \left(g'_y(p_*) - g'_p(p_*)\right)K'(y_*)\mathbf{n}(p_*)p_*\mu_y \tag{B.27b}$$

Since the p-nullcline increases and decreases where $F(p)$ increases and decreases, respectively, the Hopf condition (B.27a) shows that the only equilibria that can undergo a Hopf bifurcation are those that occur where the p-nullcline is increasing with a large enough slope s.t. $g'_p(p_*) > \frac{\mu_y}{K'(y_*)\mathbf{n}(p_*)p_*}$.

B.4.2 The transition from persistence to clearance

The bifurcations involved in the transition from low-level pathogen persistence to pathogen clearance indicated with an arrow in Figure 2.5 are illustrated in Figure B.2B where K_{max} is increased through a very narrow region of parameter space. To better illustrate key details, insets are included in Figure B.2 that contain topologically equivalent illustrations of the dynamics. We are particularly interested in initial conditions that correspond to a newly infected naive host, i.e. initial conditions that lie along the p-axis with very low pathogen density.

Preceding the transition (low K_{max}, see Figure B.2A), the basin of attraction for the persistence steady state (shaded gray) is large while the basin of attraction for the healthy state (shaded white) is a very small region near $p \approx 0$. As

show in the inset, there is a saddle equilibrium near the origin whose stable manifold forms the boundary between initial conditions that lead to the origin or to (p_*, n_*). Increasing K_{max} very near the transition zone (see Figure B.2B), it is also possible (though not necessary) for the persistence steady state to undergo a supercritical Hopf bifurcation resulting in pathogen-immune cycles. Next there is an abrupt change in the two basins of attraction that appear to result from a homoclinic bifurcation (Figure B.2C). As K_{max} is increases through this bifurcation, the arm of stable manifold (blue curve) separating the two regions lifts off of the y axis (Figure B.2A to B) and wraps around a neighborhood of the persistence steady state (or cycle) eventually intersecting the p axis. Continuing, this motion, it eventually intersects the unstable manifold of the saddle and forms a homoclinic orbit like the one shown in the Figure B.2C inset. Beyond this point, an unstable limit cycle is born from the homoclinic bifurcation and the stable manifold now spirals backwards onto this cycle leaving the interior of that cycle as the basin of attraction for disease persistence (either cycling or at steady state). Note that now all initial conditions of the form $(p > 0, y = 0)$ yield either no infection $(p \approx 0)$ or an acute infection resolved by the specific immune response. Increasing K_{max} further, the region yielding disease persistence continues to shrink and may disappear via either a saddle-node of limit cycles or a subcritical Hopf bifurcation when the unstable limit cycle collides with the stable limit cycle or stable persistence equilibrium, respectively.

Figure B.2: Details of the transition indicated by the arrow in Figure 2.5B for the *p*-*y* model (2.8) parameterized to exhibit bistability. Topologically equivalent insets are included for clarification and to show the unstable saddle (empty circle in the inset) that is so near the origin that the solid (origin) and empty (saddle) circles overlap. This transition can be understood as the result of a saddle homoclinic bifurcation near a generalized Hopf bifurcation. This figure shows the *p*-*y* dynamics before (Panels **A**, **B**), at (Panel **C**) and after (Panel **D**) the saddle homoclinic. Shading indicates the basin of attraction for disease persistence, non-shaded regions lead to the origin and the boundary between basins of attraction is the stable manifold of a saddle equilibrium (empty circle in the insets). Panel **A**: Starting at low K_{max}, infections lead to a state of pathogen persistence. Panel **B**: Increasing K_{max} through the transition region, the boundary between basins of attraction bends away from the y axis increasing the origin's basin of attraction. For most parameter sets considered, the persistence equilibrium undergoes a Hopf bifurcation resulting in cycling dynamics at low pathogen density, as shown. Panel **C**: At the saddle homoclinic bifurcation, a homoclinic orbit is formed as the stable and unstable manifolds of the saddle connect as shown in the inset. This gives rise to an unstable limit cycle that contains the basin of attraction for pathogen persistence. Panel **D**: Beyond this bifurcation, nearly all biologically meaningful trajectories lead to the origin, most after a brief excursion that corresponds to an acute infection resolved by the host immune response. See text for additional details.

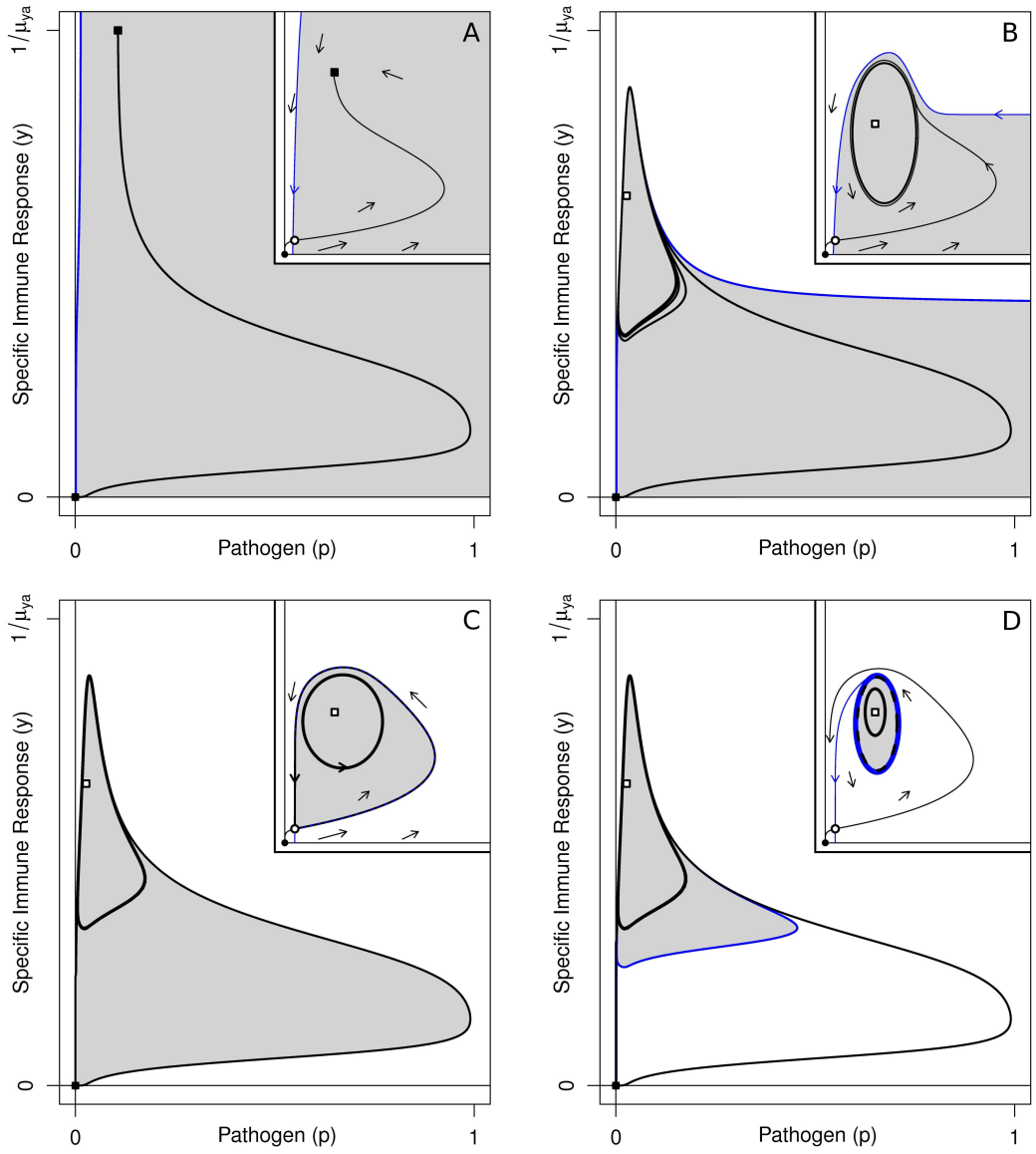
A
B
C
D
Specific Immune Response (y)
1/μya
0
Pathogen (p)
0
1

B.5 Parameter Variation and Sensitivity Analysis

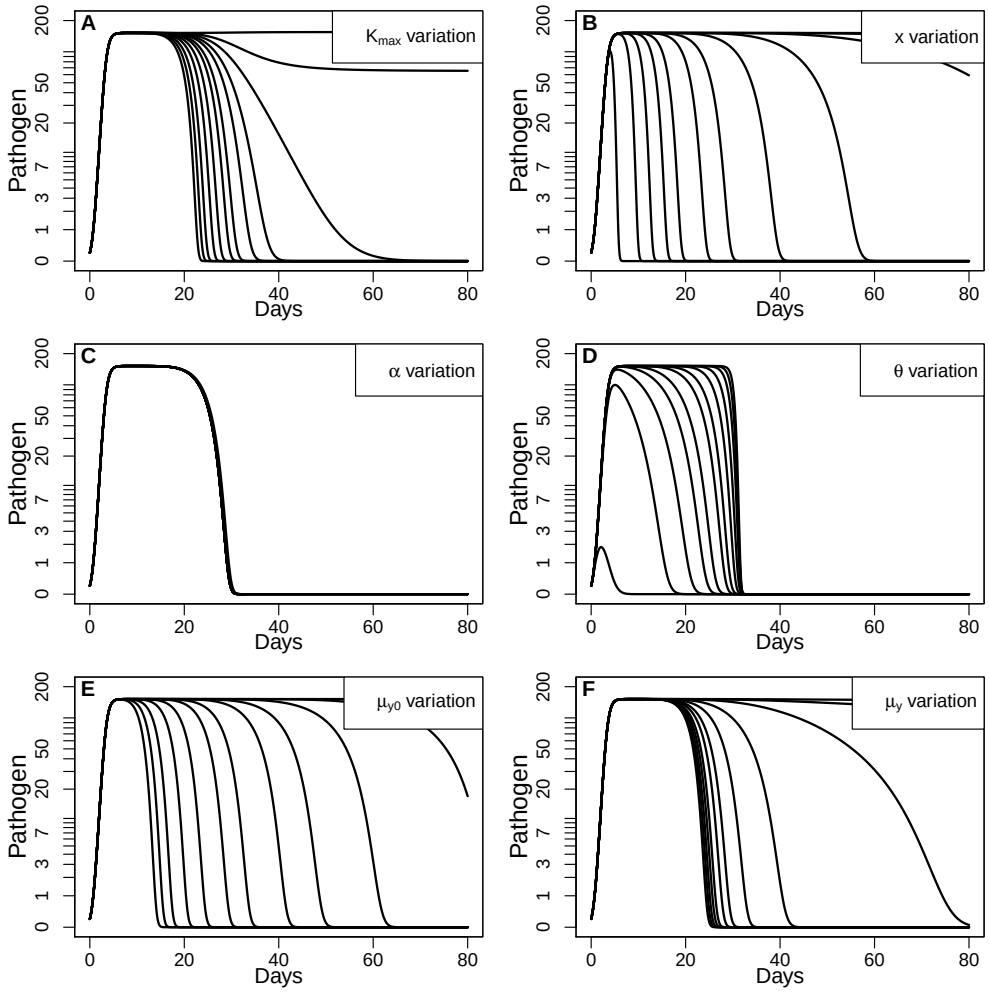

Figure B.3: Pathogen load variation under model (2.1). See Figure 2.11 for details.

BIBLIOGRAPHY

Peter A. Abrams. When does greater mortality increase population size? The long history and diverse mechanisms underlying the hydra effect. *Ecology Letters*, 12(5):462–474, 2009. ISSN 1461-0248. doi: 10.1111/j.1461-0248.2009.01282.x.

John W. Aldrich and John S. Weske. Origin and evolution of the eastern house finch population. *The Auk*, 95(3):528–536, July 1978.

Alain Blanchard and Glenn Browning, editors. *Mycoplasmas: Molecular Biology Pathogenicity and Strategies for Control*. Horizon Bioscience, Wymondham, Norfolk, U.K., April 2005. ISBN 0-8493-9861-4.

Daniel R. Brown, Robert F. Whitcomb, and Janet M. Bradbury. Revised minimal standards for description of new species of the class Mollicutes (division Tenericutes). *Int J Syst Evol Microbiol*, 57(11):2703–2719, 2007. doi: 10.1099/ijs.0.64722-0.

Carla E. Cáceres. Interspecific variation in the abundance , production, and emergence of daphnia diapausing eggs. *Ecology*, 79(5):1699–1710, 1998. doi: 10.1890/0012-9658(1998)079[1699:IVITAP]2.0.CO;2.

Christine Citti, Glenn F. Browning, and Renate Rosengarten. Phenotypic Diversity and Cell Invasion in Host Subversion by Pathogenic Mycoplasmas. In Alain Blanchard and Glenn Browning, editors, *Mycoplasmas: Molecular Biology Pathogenicity and Strategies for Control*, chapter 13, pages 439–483. Horizon Bioscience, Wymondham, Norfolk, U.K., April 2005. ISBN 0-8493-9861-4.

Troy Day. Parasite transmission modes and the evolution of virulence. *Evolution*, 55(12):2389–2400, 2001. doi: 10.1111/j.0014-3820.2001.tb00754.x.

André A. Dhondt, Sonia Altizer, Evan G. Cooch, Andrew K. Davis, Andrew Dobson, Melanie J.L. Driscoll, Barry K. Hartup, Dana M. Hawley, Wesley M. Hochachka, Parviez R. Hosseini, Christopher S. Jennelle, George V. Kollias, David H. Ley, Elliott C.H. Swarthout, and Keila V. Sydenstricker. Dynamics of a Novel Pathogen in an Avian Host: Mycoplasmal Conjunctivitis in House Finches. *Acta Tropica*, 94(1):77 – 93, 2005. ISSN 0001-706X. doi: 10.1016/j.actatropica.2005.01.009.

André A. Dhondt, Keila V. Dhondt, and Brynn V. McCleery. Comparative infectiousness of three passerine bird species after experimental inoculation with *Mycoplasma gallisepticum*. *Avian Pathology*, 37(6):635–640, 2008. ISSN 0307-9457. doi: 10.1080/03079450802499100.

Keila V. Dhondt, André A. Dhondt, and David H. Ley. Effects of route of inoculation on *Mycoplasma gallisepticum* infection in captive house finches. *Avian Pathology*, 36(6):475–479, December 2007. ISSN 0307-9457. doi: 10.1080/03079450701642016.

A. Dhooge, W. Govaerts, and Yu. A. Kuznetsov. matcont: A matlab package for numerical bifurcation analysis of ODEs. *ACM TOMS*, 29:141–164, 2003.

Meghan A. Duffy. Selective predation, parasitism, and trophic cascades in a bluegill-daphnia-parasite system. *Oecologia*, 153(2):453–460, August 2007. ISSN 0029-8549. doi: 10.1007/s00442-007-0742-y.

Meghan A. Duffy, Spencer R. Hall, Alan J. Tessier, and Marianne Huebner. Selective predators and their parasitized prey: Are epidemics in zooplankton under top-down control? *Limnology and Oceanography*, 50(2):412–420, 2005. ISSN 00243590. doi: 10.2307/3597716.

Meghan A. Duffy, Chad E. Brassil, Spencer R. Hall, Alan J. Tessier, Carla E. Caceres, and Jeffrey K. Conner. Parasite-mediated disruptive selection in a natural daphnia population. *BMC Evolutionary Biology*, 8:80+, March 2008. ISSN 1471-2148. doi: 10.1186/1471-2148-8-80.

MeghanA. Duffy and SpencerR. Hall. Selective predation and rapid evolution can jointly dampen effects of virulent parasites on daphnia populations. *The American Naturalist*, 171(4):499–510, 2008. doi: 10.1086/528998. PMID: 18260781.

Dieter Ebert. *Ecology, Epidemiology, and Evolution of Parasitism in Daphnia*. Bethesda (MD): National Library of Medicine (US), National Center for Biotechnology Information. Available from: http://www.ncbi.nlm.nih.gov/entrez/query.fcgi?db=Books, November 2005.

D. G. ff. Edward and E. A. Freundt. Proposal for Mollicutes as name of the class established for the order Mycoplasmatales. *Int J Syst Bacteriol*, 17(3):267–268, 1967. doi: 10.1099/00207713-17-3-267.

D. G. ff. Edward and A. D. Kanarek. Organisms of the pleuropneumonia group of avian origin: their classification into species. *Annals of the New York Academy of Sciences*, 79(10):696–702, Jan 1960. doi: 10.1111/j.1749-6632.1960.tb42744.x.

John J. Elliott and Robert S. Aribib Jr. Origin and Status of the Eastern House Finch in the Eastern United States. *The Auk*, 70(1):31–37, January 1953.

Cristina R. Faustino, Christopher S. Jennelle, Véronique Connolly, Andrew K. Davis, Elliott C. Swarthout, André A. Dhondt, and Evan G. Cooch. *Mycoplasma gallisepticum* infection dynamics in a house finch population: sea-

sonal variation in survival, encounter and transmission rate. *Journal of Animal Ecology*, 73(4):651–669, 2004. doi: 10.1111/j.0021-8790.2004.00840.x.

J. R. Fischer, D. E. Stallknecht, P. Luttrell, A. A. Dhondt, and K. A. Converse. Mycoplasmal conjunctivitis in wild songbirds: the spread of a new contagious disease in a mobile host population. *Emerg Infect Dis*, 3(1):6972, JanMar 1997.

Jessica L. Grodio, Keila V. Dhondt, Priscilla H. O'Connell, and Karel A. Schat. Detection and quantification of *Mycoplasma gallisepticum* genome load in conjunctival samples of experimentally infected house finches (*Carpodacus mexicanus*) using real-time polymerase chain reaction. *Avian Pathology*, 37(4):385–391, August 2008. ISSN 0307-9457. doi: 10.1080/03079450802216629.

Jessica L. Grodio, Dana M. Hawley, Erik E. Osnas, David H. Ley, Keila V. Dhondt, André A. Dhondt, and Karel A. Schat. Pathogenicity and immunogenicity of three *Mycoplasma gallisepticum* isolates in house finches (*Carpodacus mexicanus*). *Veterinary Microbiology*, 2011. ISSN 0378-1135. doi: 10.1016/j.vetmic.2011.08.003.

James P. Grover. *Resource Competition*. Number 19 in Population and Community Biology. Chapman & Hall, 1997.

John Guckenheimer and Mark Myers. Computing hopf bifurcations. ii: Three examples from neurophysiology. *SIAM Journal on Scientific Computing*, 17(6): 1275–1301, 1996. doi: 10.1137/S1064827593253495.

John Guckenheimer, Mark Myers, and Bernd Sturmfels. Computing Hopf Bifurcations I. *SIAM Journal on Numerical Analysis*, 34(1):1–21, 1997. ISSN 00361429. doi: 10.2307/2952033.

S. R. Hall, A. J. Tessier, M. A. Duffy, M. Huebner, and C. E. Cáceres. Warmer does not have to mean sicker: temperature and predators can jointly drive timing of epidemics. *Ecology*, 87(7):1684–1695, July 2006. ISSN 0012-9658. doi: 10.1890/0012-9658(2006)87[1684:WDNHTM]2.0.CO;2.

S. R. Hall, C. R. Becker, J. L. Simonis, M. A. Duffy, A. J. Tessier, and C. E. Cáceres. Friendly competition: evidence for a dilution effect among competitors in a planktonic host-parasite system. *Ecology*, 90(3):791–801, March 2009a. ISSN 0012-9658. doi: 10.1890/08-0838.1.

Spencer Hall, Meghan Duffy, and Carla Cáceres. Selective predation and productivity jointly drive complex behavior in host-parasite systems. *The American Naturalist*, 165(1):70–81, January 2005. doi: 10.1086/426601.

Spencer R. Hall, Lena Sivars-Becker, Claes Becker, Meghan A. Duffy, Alan J. Tessier, and Carla E. Cáceres. Eating yourself sick: transmission of disease as a function of foraging ecology. *Ecology Letters*, 10(3):207–218, March 2007. ISSN 1461-023X. doi: 10.1111/j.1461-0248.2007.01011.x.

Spencer R. Hall, Christine J. Knight, Claes R. Becker, Meghan A. Duffy, Alan J. Tessier, and Carla E. Cáceres. Quality matters: resource quality for hosts and the timing of epidemics. *Ecology Letters*, 12(2):118–128, 2009b. ISSN 1461-0248. doi: 10.1111/j.1461-0248.2008.01264.x.

Hall, Spencer R. and Simonis, JosephL. and Nisbet, RogerM. and Tessier, AlanJ. and Cáceres, CarlaE. Resource ecology of virulence in a planktonic host-parasite system: An explanation using dynamic energy budgets. *The American Naturalist*, 174(2):149–162, 2009. doi: 10.1086/600086. PMID: 19527119.

BK Hartup, AA Dhondt, KV Sydenstricker, WM Hochachka, and GV Kol-

lias. Host range and dynamics of mycoplasmal conjunctivitis among birds in North America. *J Wildl Dis*, 37(1):72–81, 2001.

D. M. Hawley, C. S. Jennelle, K. V. Sydenstricker, and A. A. Dhondt. Pathogen resistance and immunocompetence covary with social status in house finches (*Carpodacus mexicanus*). *Functional Ecology*, 21(3):520–527, June 2007. ISSN 0269-8463. doi: 10.1111/j.1365-2435.2007.01254.x.

D. M. Hawley, K. V. Dhondt, A. P. Dobson, J. L. Grodio, W. M. Hochachka, D. H. Ley, E. E. Osnas, K. A. Schat, and A. A. Dhondt. Common garden experiment reveals pathogen isolate but no host genetic diversity effect on the dynamics of an emerging wildlife disease. *Journal of Evolutionary Biology*, 23:1680–1688, 2010. doi: 10.1111/j.1420-9101.2010.02035.x.

JM Hickman-Davis, SM Michalek, J Gibbs-Erwin, and JR Lindsey. Depletion of alveolar macrophages exacerbates respiratory mycoplasmosis in mycoplasma-resistant C57BL mice but not mycoplasma-susceptible C3H mice. *Infect. Immun.*, 65(6):2278–2282, 1997.

F. M. Hilker and K. Schmitz. Disease-induced stabilization of predator-prey oscillations. *Journal of theoretical biology*, 255(3):299–306, December 2008. ISSN 1095-8541. doi: 10.1016/j.jtbi.2008.08.018.

Wesley M. Hochachka and Andr A. Dhondt. Density-dependent decline of host abundance resulting from a new infectious disease. *Proceedings of the National Academy of Sciences of the United States of America*, 97(10):5303–5306, 2000. doi: 10.1073/pnas.080551197.

George V. Kollias, Keila V. Sydenstricker, Heidi W. Kollias, David H. Ley, Parviez R. Hosseini, Veronique Connolly, and André A. Dhondt. Experimen-

tal Infection of House Finches with *Mycoplasma gallisepticum*. *J Wildl Dis*, 40 (1):79–86, 2004.

Kelly Lee, Lynn Martin, and Martin Wikelski. Responding to inflammatory challenges is less costly for a successful avian invader, the house sparrow (*Passer domesticus*), than its less-invasive congener. *Oecologia*, 145:243–250, 2005. ISSN 0029-8549. doi: 10.1007/s00442-005-0113-5.

Kelly A. Lee. Linking immune defenses and life history at the levels of the individual and the species. *Integrative and Comparative Biology*, 46(6):1000–1015, October 2006. doi: 10.1093/icb/icl049.

Curtis M. Lively. The ecology of virulence. *Ecology Letters*, 9(10):1089–1095, October 2006. ISSN 1461-023X. doi: 10.1111/j.1461-0248.2006.00969.x.

M. P. Luttrell, J. R. Fischer, D. E. Stallknecht, and S. H. Kleven. Field Investigation of *Mycoplasma gallisepticum* Infections in House Finches (*Carpodacus mexicanus*) from Maryland and Georgia. *Avian Diseases*, 40(2):335–341, April-June 1996. ISSN 00052086.

MP Luttrell, DE Stallknecht, JR Fischer, CT Sewell, and SH Kleven. Natural Mycoplasma gallisepticum infection in a captive flock of house finches. *Journal of Wildlife Disease*, 34(2):289–296, 1998.

Lynn B. Martin II, Monica Pless, Julia Svoboda, and Martin Wikelski. Immune Activity in Temperate and Tropical House Sparrows: A Common-Garden Experiment. *Ecology*, 85(8):2323–2331, 2004. doi: 10.1890/03-0365.

Edward McCauley, Roger M. Nisbet, William W. Murdoch, Andre M. de Roos, and William S. C. Gurney. Large-amplitude cycles of daphnia and its algal

prey in enriched environments. *Nature*, 402(6762):653–656, December 1999. ISSN 0028-0836. doi: 10.1038/45223.

I Mikaelian, DH Ley, R Claveau, M Lemieux, and JP Berube. Mycoplasmosis in evening and pine grosbeaks with conjunctivitis in Quebec. *J Wildl Dis*, 37(4): 826–830, 2001.

William W. Murdoch, Cheryl J. Briggs, and Roger M. Nisbet. *Consumer-Resource Dynamics*. Monographs in population biology; 36. Princeton University Press, Princeton, NJ, 2003. ISBN 13: 978-0-691-00657-4.

Erik E. Osnas and Andrew P. Dobson. Evolution of virulence when transmission occurs before disease. *Biology Letters*, 6(4):505–508, 2010. doi: 10.1098/rsbl.2009.1019.

Richard S. Ostfeld, Felicia Keesing, and Valerie T. Eviner, editors. *Infectious disease ecology: effects of ecosystems on disease and of disease on ecosystems*. Princeton University Press, 2008.

Leka Papazisi, Timothy S. Gorton, Gerald Kutish, Philip F. Markham, Glenn F. Browning, Di Kim Nguyen, Steven Swartzell, Anup Madan, Greg Mahairas, and Steven J. Geary. The complete genome sequence of the avian pathogen *Mycoplasma gallisepticum* strain R_{low}. *Microbiology*, 149(9):2307–2316, 2003. doi: 10.1099/mic.0.26427-0.

Karen G. Porter, Jeroen Gerritsen, and Jr. Orcutt, John D. The effect of food concentration on swimming patterns, feeding behavior, ingestion, assimilation, and respiration by daphnia. *Limnology and Oceanography*, 27(5):935–949, 1982. ISSN 00243590.

Angela Reynolds, Jonathan Rubin, Gilles Clermont, Judy Day, Yoram Vodovotz, and G. Bard Ermentrout. A reduced mathematical model of the acute inflammatory response: I. Derivation of model and analysis of anti-inflammation. *Journal of Theoretical Biology*, 242(1):220 – 236, April 2006. ISSN 0022-5193. doi: 10.1016/j.jtbi.2006.02.016.

Michael L. Rosenzweig. Paradox of enrichment: Destabilization of exploitation ecosystems in ecological time. *Science*, 171(3969):385–387, 1971. doi: 10.1126/science.171.3969.385.

M. Roy and R. D. Holt. Effects of predation on host-pathogen dynamics in sir models. *Theoretical population biology*, 73(3):319–331, May 2008. ISSN 1096-0325. doi: 10.1016/j.tpb.2007.12.008.

Marten Scheffer, Sergio Rinaldi, Yuri A. Kuznetsov, and Egbert H. van Nes. Seasonal dynamics of daphnia and algae explained as a periodically forced predator-prey system. *Oikos*, 80(3):519–532, 1997. ISSN 00301299.

Lee A. Segel and Alan S. Perelson. Exploiting the diversity of time scales in the immune system: A B-cell antibody model. *Journal of Statistical Physics*, 63: 1113–1131, 1991. ISSN 0022-4715. doi: 10.1007/BF01030002.

Jerry W. Simecka. Immune Responses Following Mycoplasma Infection. In Alain Blanchard and Glenn Browning, editors, *Mycoplasmas: Molecular Biology Pathogenicity and Strategies for Control*, chapter 14, pages 485–534. Horizon Bioscience, Wymondham, Norfolk, U.K., April 2005. ISBN 0-8493-9861-4.

Constantine Sorokin and Robert W. Krauss. The effects of light intensity on the growth rates of green algae. *Plant Physiol.*, 33(2):109–113, 1958. doi: 10.1104/pp.33.2.109.

Keila V. Sydenstricker, André A. Dhondt, David H. Ley, and George V. Kollias. Re-Exposure of Captive House Finches That Recovered From *Mycoplasma gallisepticum* Infection. *J Wildl Dis*, 41(2):326–333, 2005.

Keila V. Sydenstricker, André A. Dhondt, Dana M. Hawley, Christopher S. Jennelle, Heidi W. Kollias, and George V. Kollias. Characterization of Experimental *Mycoplasma gallisepticum* Infection in Captive House Finch Flocks. *Avian Diseases*, 50(1):39–44, 2006. doi: 10.1637/7403-062805R.1.

Chelsea L. Wood, James E. Byers, Kathryn L. Cottingham, Irit Altman, Megan J. Donahue, and April M. H. Blakeslee. Parasites alter community structure. *Proceedings of the National Academy of Sciences*, 104(22):9335–9339, 2007. doi: 10.1073/pnas.0700062104.